DESIGN AND ANALYSIS OF SCULPTED ROTOR INTERIOR PERMANENT MAGNET MACHINES

By

Steven Lee Hayslett

A DISSERTATION

Submitted to
Michigan State University
in partial fulfillment of the requirements
for the degree of

Mechanical Engineering - Doctor of Philosophy

2022

ABSTRACT

DESIGN AND ANALYSIS OF SCULPTED ROTOR INTERIOR PERMANENT MAGNET MACHINES

By

Steven Lee Hayslett

Design of interior permanent magnet electrical machines is complex. Interior permanent magnet machines offer a good balance of cost, efficiency, and torque/power density. Maximum torque and power production of an interior permanent magnet machine is achieved through balancing design choices related to the permanent magnet and salient features. The embedded magnet within the salient structure of the rotor lamination results in an increase in harmonic content. In addition, interaction of the armature, control angle, and rotor reluctance structure creates additional harmonic content. These harmonics result in increased torque ripple, radial forces, losses, and other unwanted phenomena. Further improvements in torque and power density, and techniques to minimize harmonics, are necessary. Typical interior permanent magnet machine design results at the maximum torque per amp condition are at neither the maximum magnet nor maximum salient torque, but at the best combination of the two. The use of rotor surface features to align the magnet and the reluctance axis allows for improvement of torque and power density. Reduction of flux and torque harmonics is also possible through careful design of rotor sculpt features that are included at or near the surface of the rotor.

Finite element models provide high fidelity and accurate results to machine performance, but do not give insight into the relationship between design parameters and performance. Winding factor models describe the machine with a set of Fourier series equations, providing access to the harmonic information of both parameters and performance. Direct knowledge of

this information provides better insight, clear understanding of interactions, and the ability to develop a more efficient design process. A new analytical winding function model of the single-V IPM machine is introduced, which considers the sculpted rotor and how this model can be used in the design approach of machines.

Rotor feature trends are established and utilized to increase design intuition and reduce dependency upon the lengthy design of experiment optimization processes. The shape and placement of the rotor features, derived from the optimization process, show the improvement in torque average and torque ripple of the IPM machine.

ACKNOWLEDGMENTS

First, I would like to express my deepest thanks to Dr. Elias Strangas for his patience, support, and guidance in enabling me to complete my Ph.D. program. It has been a great experience working with him over the past years. I have learned much and gained perspective from him.

Second, I would like to pay my special regards to the members of the Electric Machines and Power Electronics Research (EMPowER) Laboratory at Michigan State University. Thank you, Dr. Thang Pham, Dr. Anmol Aggarwal, Matt Meier, Tiraruek Ruekamnuaychok, Cristian Lopez Martinez, Dr. Reemon Haddad, Dr. William Jensen, Dr. Abdullah Alfehaid, and Dr. Shanelle Foster.

I would also like to thank my Ph.D. guidance committee members Dr. Andre Benard, Dr. Abraham Engeda, and Dr. George Zhu.

This would have not been possible without the endless support of my wife Ratsada and son Tyler. In addition, I am grateful to my parents Lyle and Marge for encouraging me to pursue a lifetime of learning.

Finally, I would like to pay my special regards to my inspiring colleagues and mentors, Dr. Sinisa Jurkovic, Dr. Khawja Rahman, Dr. Yochan Son, Dr. Tausif Husain, and Peter Savagian.

TABLE OF CONTENTS

LIST OF TABLES . . . . **ix**

LIST OF FIGURES . . . . **x**

KEY TO SYMBOLS AND ABBREVIATIONS . . . . **xv**

Chapter 1 Introduction **1**
- 1.1 Problem Statement 1
- 1.2 Objective and Contributions 3
- 1.3 Background 5
  - 1.3.1 Transportation Sector Trends 5
  - 1.3.2 Interior Permanent Magnet Machines 6
  - 1.3.3 Rotor Modifications 9
  - 1.3.4 Analytical Methods 11
    - 1.3.4.1 Review of Recent Analytical Models 14
- 1.4 Organization of Thesis 16

Chapter 2 Fundamentals: Magnetics **17**
- 2.1 Stator with Sinusoidally Distributed Windings 19
- 2.2 Salient Rotor Geometry Analysis 20
- 2.3 Permanent Magnets 24
  - 2.3.1 Permanent Magnet Properties and Equivalent Current 24
  - 2.3.2 Simplified Permanent Magnet Analysis 30
- 2.4 Magnetic Dipole and Equivalent Magnetic Currents 32
- 2.5 Torque Analysis 35
- 2.6 Flux Linkage and Inductance 37
- 2.7 First Analysis of Machine Design 38
  - 2.7.1 Ideal Case 42
  - 2.7.2 Magnet Geometry Effects 42

Chapter 3 Fundamentals: Implementation and Control **46**
- 3.1 Voltage Equations 46
  - 3.1.1 Voltage Equations in ABC 48
  - 3.1.2 The Clarke Transformation: Voltage Equations in $\alpha\beta$ 50
  - 3.1.3 The Park Transformation: Voltage Equations in DQ Coordinates . . 51
- 3.2 Torque Equation 52
- 3.3 First Analysis of Machine Performance and Control 56
  - 3.3.1 Example Machine 58
- 3.4 Relationship to Design 63

Chapter 4 MMF Permeance Theory **64**

4.1 Air Gap Permeance 64
4.2 Rotor Reluctance Path 65
4.3 Stator Slots by Permeance Function 68
4.4 Windings, MMF, Linear Current Density 70
4.4.1 Stator MMF Modifications for the Second Reluctance Path 71
4.5 Sculpted and Slotted Features by MMF Function 73
4.5.1 Application of Superposition for Slotted Features 74
4.5.2 Magnet MMF and Sculpted Rotor 76
4.5.3 MMF of the Second Reluctance Path due to Rotor Sculpting 79
4.6 Flux Linkage and Inductance 80
4.7 Example Machine 81

Chapter 5 Space and Time Harmonics of Fields, Permeance, and Torque 91
5.1 Fourier Series Description 91
5.1.1 Current 91
5.1.2 Permeance 92
5.1.3 Winding and Turns Functions 93
5.1.4 MMF and Linear Current Density 94
5.2 Rotating Harmonics 96
5.2.1 Armature MMF 96
5.2.2 Primary Reluctance Path Flux Density Harmonics 96
5.2.3 Linear Current Density Harmonics 97
5.2.4 Torque Harmonic Orders from Air Gap Flux Density and Linear Current Density 99
5.2.5 Magnet Flux Density and Torque Harmonics 100
5.2.6 Field and Torque Harmonics Relationship to Control Angle 101
5.3 Example Machine Mechanical Harmonics 103

Chapter 6 Design for Minimal Torque Ripple 106
6.1 Review of Design Methods and Features 106
6.2 Application of Analytical Model to Example Machine 107
6.2.1 Sculpting Geometry 108
6.3 Model Validation: Radial Flux Density 109
6.4 Model Validation: Torque Ripple 111
6.5 Torque Ripple Components 112
6.6 Investigation of Design Features 114
6.6.1 Magnet Pole Arc 114
6.6.2 Single Pair Symmetrical Rotor Sculpt Feature 115
6.6.3 Single Asymmetrical Rotor Sculpt Feature 117
6.6.4 Two Symmetrical Rotor Sculpt Features 117
6.7 Conclusions 120

Chapter 7 Optimal Design for Minimal Torque Ripple 122
7.1 Methods 122
7.2 Electric Machine Parameters 122

7.3 Minimization of Torque Harmonics . . . 123
7.3.1 Optimization Methodology . . . 124
7.4 Optimal Designs . . . 127
7.5 Finite Element Detailed Search of Design Space . . . 129
7.6 Exhaustive Search . . . 130
7.7 Conclusion . . . 133

Chapter 8 Conclusion . . . 135
8.1 Closing . . . 135
8.2 Future Work . . . 135

BIBLIOGRAPHY . . . 137

LIST OF TABLES

Table 3.1: Example Machine 58

Table 4.1: Example Motor Parameters 82

Table 5.1: Armature MMF Harmonic Sequencing Summary, negative sequence (+), positive sequence (-), not applicable (n/a). Not applicable is due to cancellation of triplen harmonics of the 3 phases or even MMF components are not possible due to convolution. 97

Table 5.2: Linear Current Density Electrical Harmonic Sequence Value 98

Table 5.3: Air Gap Field Spatial Electrical Harmonic Convolution, Horizontal - Flux Density Harmonics, Vertical - Linear Current Density Harmonics 99

Table 5.4: Air Gap Field Spatial Electrical Harmonic Convolution and Electrical Torque Harmonic, Horizontal - Flux Density Harmonics, Vertical - Linear Current Density Harmonics 100

Table 5.5: Airgap flux density Fourier coefficients dependency on reference frame currents. 102

Table 5.6: Mechanical Harmonics of Example Machine 105

Table 6.1: Example motor parameters. 107

Table 6.2: Two sculpt feature parameters. 118

Table 7.1: Motor Parameters 123

Table 7.2: Analytical Model Sculpt Feature Designs 127

LIST OF FIGURES

Figure 1.1: Interior Permanent Magnet Machine 7

Figure 1.2: A Single Pole of an Interior Permanent Magnet Machine: a) slot, b) tooth, c) stator yoke, d) winding/conductor, e) rib (secondary reluctance path), f) bridge, g) stator OD, h) stator ID, i) rotor OD, j) barrier, k) rib (primary reluctance path), l) magnet, n) airgap 8

Figure 1.3: IPM rotor types: single V (**left**), delta (**center**), double V (**right**). . . . 10

Figure 1.4: Example Interior Permanent Magnet Machine with Rotor Sculpt Features 11

Figure 2.1: Radial and Tangential Flux Density in Air Gap 18

Figure 2.2: Sinudsoidally Distributed Three Phase Windings 20

Figure 2.3: Doubly Sinusoidal Air Gap: The salient rotor is shown in blue and the stator in yellow. 21

Figure 2.4: Integration Path for Ampere's Law, Current Sheet (red) 23

Figure 2.5: Magnetization Curve [1] 25

Figure 2.6: Demagnetization Curve [1] 26

Figure 2.7: Permanent Magnet Model: A_m area of magnet, A_g area of gap, B_m magnet flux density, H_m magnet field strength, B_g airgap flux density, H_g air gap field strength, l_m length of magnet, g length of airgap, $N_1 I_1$ amp turns 27

Figure 2.8: Equivalent Current Permanent Magnet Model: A_m area of magnet, A_g area of gap, B_m magnet flux density, H'_m magnet field strength, B_g airgap flux density, H_g air gap field strength, l_m length of magnet, g length of airgap, $N_1 I_1$ amp turns 28

Figure 2.9: Magnet Properties 30

Figure 2.10: Flux Paths: Crossing the Air Gap (red) , Leakage (blue) 31

Figure 2.11: Magnetic Dipole From Current Loop [2] 34

Figure 2.12: Inegration Path for Flux and Flux Linkage 38

Figure 2.13: Basic Geometry, $\delta = 45°$: toroidal core (yellow), rotor (orange), north magnets(red), south magnet(blue) 39

Figure 2.14: Theoretical Torque Versus Current Angle IPM Machine , $\delta = 0°$: Reluctance Torque (blue), Magnet Torque (red), Total (black dashed) 40

Figure 2.15: Theoretical Torque Versus Current Angle IPM Machine , $\delta = 45°$: Reluctance Torque (blue), Magnet Torque (red), Total (black dashed) . . . 41

Figure 2.16: Torque Benefit of Ideal Aligned Axis Design as Compared to Traditional Alignment (% increase) 43

Figure 2.17: Torque Benefit as Function of Alignment Angle and Magnet Width as Percentage of Pole Span: ideal case torque (black dashed), 100% magnet span torque (red), 66% magnet span torque (green), 50% magnet span torque (blue) , 50% magnet span torque (blue), magnet physical vs actual shift angle (blue dashed) , magnet physical vs actual shift angle (blue dashed dotted) 45

Figure 3.1: Motor Structure with Voltage Eq 47

Figure 3.2: Single Coil Reluctance System 53

Figure 3.3: Example Machine Current Plane $\delta = 0°$, current limit (blue circle), voltage limit (green ellipse), maximum torque per ampere (MTPA) trajectory (orange curve), maximum speed of MTPA (orange *), maximum speed at full current (purple x), short circuit current (purple circle). 59

Figure 3.4: Example Machine Current Plane $\delta = 45°$,current limit (blue circle), voltage limit (green ellipse), maximum torque per ampere (MTPA) trajectory (orange curve), maximum speed of MTPA (orange *), maximum speed at full current (purple x), short circuit current (purple circle). 60

Figure 3.5: Example Machine Torque and Power Speed Curves $\delta = 0°$ 61

Figure 3.6: Example Machine Torque and Power Speed Curves $\delta = 45°$ 62

Figure 4.1: Permeability of IPM Rotor 67

Figure 4.2: Stator slots physical and air gap model: tooth width w_{th}, slot width w_s, slot height h_s, air gap g, slot pitch τ_s, tooth percenatage of slot width γ, effective slot height h_{s1}, stator coordinate α, effective stator air gap g_s . 69

Figure 4.3: Constant air gap machine [3] 71

Figure 4.4: MMF modifications for secondary reluctance paths: MMF of the armature(blue), average MMF across the 2nd reluctance path (green), modified second reluctance path MMF (modified second reluctance path MMF = MMF of the armature - average MMF across the 2nd reluctance path). . 72

Figure 4.5: Useage of Superposition and Equivalent Magnetization Currents (a) slotted stator (b) toroidal stator (c) stator with EMC (d - e) modified EMC [4] 75

Figure 4.6: Magnet Pole Equivalent Winding Factor 77

Figure 4.7: Scupted Rotor Superposition (a) sculpted rotor (b) unsculpted rotor (c) sculpted rotor equivalent magnetic currents 77

Figure 4.8: Sculpted Rotor Winding Function 78

Figure 4.9: Sculpted Rotor Magnet Pole Flux Density 78

Figure 4.10: Sculpted Rotor Reluctance Counter Dipole Current 79

Figure 4.11: Example Motor 82

Figure 4.12: Example Motor Air Gap Permeance Functions Versus Stator Coordinate 84

Figure 4.13: Example Motor Stator Winding Functions Versus Stator Coordinate . . 85

Figure 4.14: Example Rotor Equivalent Magnet Winding Functions Versus Stator Coordinate 85

Figure 4.15: Example Stator Conductor Width Function Versus Stator Coordinate . 86

Figure 4.16: Analytically Calculated Stator MMF for Primary and Secondary Reluctance Paths Versus Stator Coordinate 87

Figure 4.17: Analytically Calculated Motor Radial Flux Density Versus Stator Coordinate 87

Figure 4.18: Example Motor Magnet Sculpt Feature Winding Function Versus Stator Coordinate 88

Figure 4.19: Example Motor Reluctance Sculpt Feature MMF Versus Stator Coordinate, MMF due to sculpt feature based on primary reluctance path (blue), MMF due to sculpt feature based on secondary reluctance path (red) . . 89

Figure 4.20: Example Motor Flux Density Sculpted vs Smooth Versus Stator Coordinate 89

Figure 4.21: Example Motor Torque Ripple Versus Rotor Position Using MMF Permeance Model and Maxwell Stress Tensor 90

Figure 5.1: Permeance and Winding Functions 93

Figure 6.1: Rotor sculpt features. 110

Figure 6.2: Radial flux densities with sinusoidally distributed windings ($N = 200$) at various currents and control angles. 110

Figure 6.3: Radial flux densities with distributed windings (2 SPP) at various currents and control angles. 110

Figure 6.4: Radial flux densities with single symmetrical sculpt feature located at $\tau_1 = 50\%$, $W_1 = 10\%$, and $D_1 = 1.2$ mm. 111

Figure 6.5: Radial flux densities (reluctance only) with single asymmetrical sculpt feature located at $\tau = 50\%$, $W = 20\%$, and $D = 1.2$ mm. 111

Figure 6.6: Smooth rotor IPM torque ripple. 112

Figure 6.7: Sculpt feature torque ripple. 112

Figure 6.8: Analytical model torque ripple components at various control angles. . . . 113

Figure 6.9: Effects of magnet pole arc τ_p loaded at $I_{ss} = 200$ and $\beta = 135°$. 115

Figure 6.10: Symmetrical sculpt feature effects compared to finite elements: $D_1 = 1.2$ mm, $W_1 = 5\%$. 116

Figure 6.11: Symmetrical sculpt feature effects with phasor diagram: $D_1 = 1.2$ mm, $W_1 = 9\%$. 116

Figure 6.12: Sculpt feature effects $N = 1$. 118

Figure 6.13: Single asymmetrical sculpt feature effects with phasor diagram: $D_1 = 1.2$ mm, $W_1 = 5\%$. 119

Figure 6.14: Two sculpt features of 12th order electrical torque phasor plot. 120

Figure 7.1: Two pole equivalent Scrupted Rotor IPM model 123

Figure 7.2: Rotor Sculpt Feature, bridge stress (red arrow), sculpt stress (green arrow) 125

Figure 7.3: Rotor Stresses, 5000 rpm, D1=2mm, Z1=0.1 126

Figure 7.4: Comparison of Sculpt Feature Effects to Average Torque (FE and Model), $I_{ss} = 200A, \beta = 112°$ . . . 128

Figure 7.5: Comparison of Sculpt Feature Design Effects to Torque Ripple (FE and Model), $I_{ss} = 200A, \beta = 112°$ . . . 128

Figure 7.6: FE Torque Comparison of Analytical Model Optimized Sculpt Features, $I_{ss} = 200A, \beta = 180°$ . . . 129

Figure 7.7: Finite Element Extended Search of Design 2, $I_{ss} = 200A, \beta = 112°$, Constraint: Dashed Red Line, Analytical Design: Red * . . . 130

Figure 7.8: Finite Element Extended Search of Design 3, $I_{ss} = 200A, \beta = 112°$, Analytical Design: Red * . . . 131

Figure 7.9: Finite Element Extended Search of Design 4, $I_{ss} = 200A, \beta = 112°$, Constraint: Dashed Red Line, Analytical Design: Red * . . . 131

Figure 7.10: Finite Element Exhaustive Search, Order = 6, $I_{ss} = 200A, \beta = 112°$, Design 2 (red), Design 3 (green), Design 4 (yellow) . . . 132

Figure 7.11: Finite Element Exhaustive Search, Order = 12, $I_{ss} = 200A, \beta = 112°$, Design 2 (red), Design 3 (green), Design 4 (yellow) . . . 132

Figure 7.12: Finite Element Exhaustive Search, Order = 0, $I_{ss} = 200A, \beta = 112°$, Design 2 (red), Design 3 (green), Design 4 (yellow) . . . 133

KEY TO SYMBOLS AND ABBREVIATIONS

I_{ss} phase current (peak)

β control angle

p pole pairs

i_d d-axis current

i_q q-axis current

I_a phase a current

I_b phase b current

I_c phase c current

I_f magnet equivalent field current

θ stator or rotor azimuthal coordinate

ϕ rotor position

δ magnet offset

l stack length

g air gap dimension

Λ_{r1} primary reluctance path permeance

Λ_{r2} secondary reluctance path permeance

Λ_m magnet path permeance

N_a phase a winding factor

N_b phase b winding factor

N_c phase c winding factor

N_r equivalent magnet winding factor

n_a phase a turns function

n_b phase b turns function

n_c phase c turns function

C_a phase a conductor density function

C_b phase b conductor density function

C_c phase c conductor density function

F_a phase A MMF

F_b phase B MMF

F_c phase C MMF

F_{PM} rotor magnet MMF

F_{abc} 3 phase MMF

F_{r2} modified F_{abc} for 2nd reluctance path

J volume current density

K linear current density

K_{abc} linear current density of 3 phase windings

$B_{r1}(\theta, \phi)$ primary reluctance path radial flux density

$B_{r2}(\theta, \phi)$ secondary reluctance path radial flux density

$B_m(\theta, \phi)$ magnet path radial flux density

T_{r1} primary reluctance torque

T_{r2} secondary reluctance torque

T_m magnet torque

l_d d- axis inductance

l_q q- axis inductance

λ_d d- axis flux linkage

λ_q q- axis flux linkage

λ_m d- axis flux linkage of magnet

R_x radius

H_x magnetic field intensity

$\mu_\circ$ permeability of free space

A area

MMF magnetomotive force

EMF electromotive force

PM permanent magnet machine

PMAC permanent magnet alternating current machine

IPM interior permanent magnet machine

IM induction machine

EMC equivalent magnetization current

MEC magnetic equivalent circuit

FE finite element

Chapter 1

Introduction

1.1 Problem Statement

The IPM machine is increasingly being utilized throughout the transportation industry as a primary source of propulsion due to its good efficiency, torque, and power density. IPM machines bury the magnet within the rotor to achieve a balance of cost, performance, capability, efficiency, and power and torque density. Ideally, only a constant torque is produced from a sinusoidal distribution of airgap flux densities. The embedding of the magnet within the salient structure of the rotor lamination, coupled with distributing the winding in discrete locations results in airgap flux density harmonics. These harmonics result in torque pulsations, radial force harmonics, losses, and other unwanted phenomena. Torque ripple is important to minimize as it is one of the main causes of vibration, premature failure, driveline oscillations, and acoustic noise. The goal of this work is to minimize torque harmonics of IPM machines.

Electric machine design choices to minimize torque ripple are often at odds with increasing torque density or decreasing manufacturing cost. Discrete choices within the armature and rotor must be made to improve torque ripple trade off. Basic design features are shown in fig. 1.2. The armature choices include both number of slots and how the winding is placed within those slots. The rotor choice is limited to the number of barriers and the strength of the magnet. Interactions of the rotor and stator discrete choices are important and have been well researched. The discrete choices in the machine alone are not enough to address the minimization of torque pulsations, and further work is needed. The focus of this work will be on the design of features at the surface of the rotor, sculpting features, to minimize torque pulsations while preserving average torque.

Finite element analysis has been the tool of choice for the design of IPM machines. This is because finite element analysis accurately predicts experimental results across a broad range of machines and has been utilized to evaluate and compare machine types and validate analytical solutions. Often, finite elements have been coupled with optimization methods, requiring large sets of design of experiments. The amount of computational resources is significant. This research seeks to develop computationally efficient methods which reduce computational effort and yield an accurate solution.

Strategic use of symmetrical rotor sculpt features provides an additional degree of freedom in design to improve torque ripple in IPM machines at a cost of torque average. Enhancements in rotor sculpt features has the potential to preserve the cost of torque average. Analytical solutions can be applied for analysis with a reduced computational effort. However, extension to design optimization is often overlooked as analytical methods may not capture all physical effects, such as fringing or saturation. To date, no analytical methods have addressed the minimization of torque ripple by the design of rotor sculpt features. The development of an accurate and low cost model for rotor sculpt features is needed to reduce reliance on computationally expensive heuristic finite element methods.

1.2 Objective and Contributions

An analytical approach to minimize IPM machine torque ripple through the optimal design of asymmetrical sculpt features is presented in this thesis. Rotor sculpting is shown to affect both average torque and torque pulsations. Torque pulsations from a smooth IPM's rotor are minimized utilizing this new analytical model to design sculpt features. The model adequately predicts performance. It not only minimizes specific harmonics of torque but also finds the optimal shape of the sculpt feature taking advantage of the computational efficiency of analytical models. An example IPM machine is modeled with this framework's permeance functions, winding functions, current sources. A novel winding function framework is presented based upon the IPM machine's flux sources: the first reluctance path, the second reluctance path, and the magnet path as shown in fig. 1.1. New to this framework are the necessary modifications to armature Magneto Motive Force (MMF) to calculate the effects of the equipotential nature of the rotor's salient features. The winding function method is extended to account for rotor surface modifications utilizing an additional MMF term. The optimization problem is defined with the objective to minimize specific orders of torque ripple. The analytical model along with optimization is used to make a smooth rotor machine better with the design of sculpting features. Starting from the FE results of the smooth rotor, the torque harmonics are determined and used to set a target for the analytical method to cancel. The analytical method is used to determine the required sculpt geometry in order to cancel the targeted torque harmonic. The analytical model is validated through FE. This is because it has been well established finite elements accurately predicts experimental results across a broad range of machines [5–8] and have been utilized to evaluate and compare machine types [8–11] and validate analytical solutions [12–22]. Both smooth and sculpted rotor airgap flux densities and torque are presented and compared. Three sculpted rotor designs were developed with the analytical model. Analytical design accuracy is validated first by comparing analytical performance to finite elements. Secondly, the geometries of the analytical optimum are compared to the FE optimum. Significant computational savings are demonstrated using the analytical model to minimize torque harmonics.

To achieve the above-stated objective, the contributions of this work are:

- Voltage and Torque equations considering the impacts of asymmetrical features to the IPM machine.
- An analytical winding factor model for the IPM machine accounting for the first reluctance path, second reluctance path, and magnet path.
- An analytical winding factor method allowing for the accurate modeling of rotor sculpt features.
- Demonstration of the analytical methods accuracy and computational efficiency benchmarked with finite elements.
- A design technique to design sculpt features through vector summation to achieve desired counter-torque amplitude and phase.
- An analytical method to minimize torque harmonics using asymmetrical rotor features demonstrated to achieve computational efficiency better than and accuracy similar to finite elements.

1.3 Background

1.3.1 Transportation Sector Trends

Recent emphasis on the impacts of the transportation industry has generated interest in technologies that reduce energy consumption. As a result, the industry is rapidly evolving around the electrification of the propulsion system, in particular automobiles and aeroplanes. The automotive industry has focused on development of battery electric vehicles [23, 24], plugin hybrid electric vehicles [25], and hybrid electric vehicles [26,27]. Similarly, aircraft are being converted to replace propulsion and any number of types of onboard energy systems, including hydraulic, mechanical, and pneumatic [28].

The electrified propulsion system consists of a battery pack, inverter, and electrical machine. The battery pack stores and converts energy electrochemically through direct current. The inverter converts electrical direct current/voltage from the battery pack to an alternating current/voltage to the terminals of the electrical machine. The electrical machine, or motor, performs electromechanical energy conversion. As it is still early in the technology life cycle of electric cars and planes, many improvements must be made to gain wide acceptance. Performance and financial hurdles remain for the entire system.

The choice in machine type is important with common choices being: permanent magnet machines (PM), interior permanent magnet machines (IPM), and induction machines (IM) each having a known possibility. Surface mount permanent magnet machines achieve high torque density but have speed limits due to magnet retention, magnet losses, and a high magnet cost [29, 30]. Induction machines save on material cost, with no need for rare earth materials, but have lower torque density, lower efficiency, and require special measures for the increased loss in the rotor. Interior permanent machine machines, bury the magnet interior to the machine and achieve a balance of cost, efficiency, torque/power density [31]. The interior permanent magnet machine has been at the center of attention for the development of these future systems [23–26].

Highly efficient, torque and power-dense electric machines are needed for these future applications [32] as this drives cost savings for both the system and the machine. Electrical machine cost is fundamentally dependent upon the machine's volume, materials, and manufacturing process. Diameter and length selections may be made with $T \propto D^2 L$, where T is torque, D is diameter, and L is length, based on prior designs while considering the need for improved torque and power density [33]. Decreasing the volume of the electrical machine requires shifting the power of the machine to higher speeds, reducing the torque of the machine.

1.3.2 Interior Permanent Magnet Machines

A two dimensional illustration of a four-pole IPM machine is contained in fig. 1.1. The IPM is fundamentally constructed of two components a stator and a rotor. The stator, often referred to as the armature, is the mechanically grounded part of the machine. It is constructed of slots, teeth, a yoke, and three phase windings. The armature teeth and yoke are constructed of a magnetically permeable iron alloy. The teeth and yoke allow for easy flow of magnetic flux to and from the air gap of the machine. The slots allow space for the copper windings. The windings are distributed within the slots and produce a Magneto Motive Force (MMF) which in turn creates the distribution of current dependant radial magnetic flux density. The placement of the windings also creates a linear current density along the bore of the stator, creating a tangential component of flux density. When arranged and controlled properly the windings produce a rotating set of fields to produce torque.

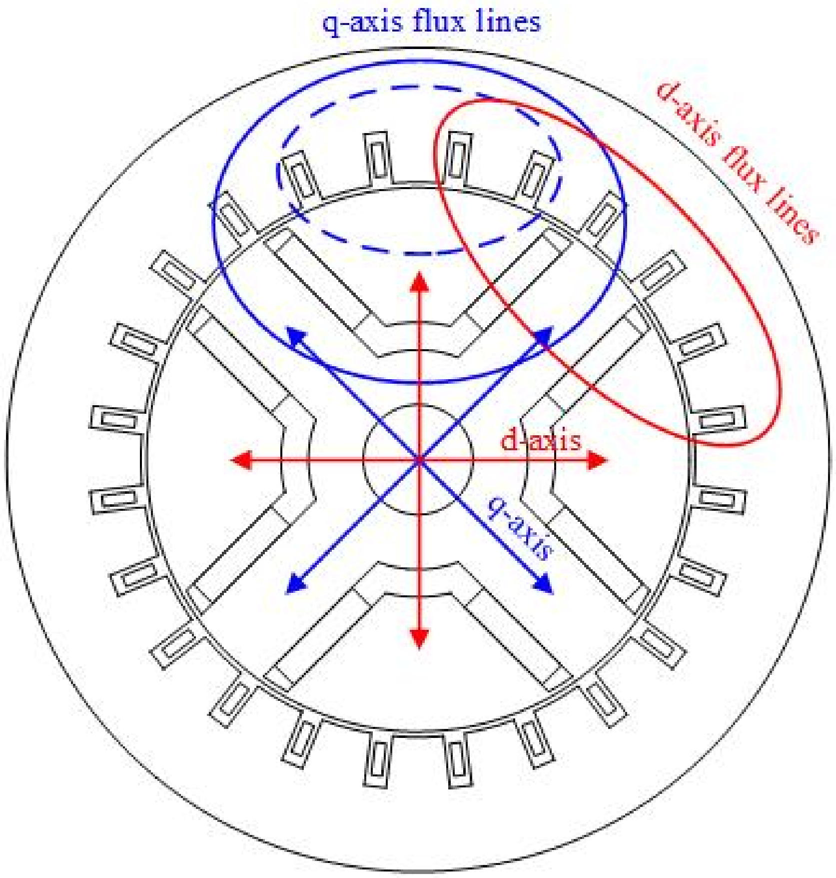

Figure 1.1: Interior Permanent Magnet Machine

As shown in fig. 1.2 the rotor, the mechanically rotating part is constructed of an iron core, barriers, and permanent magnets. The iron core is constructed of ribs and bridges. The ribs control the distribution of flux density while the bridges mechanically couple all parts together. Barriers provide air pockets, which assist the ribs in directing flux, and contain embedded magnets. The permanent magnets are embedded within the rotor and produce an MMF which is independent of the current.

From the perspective of the rotor, a direct axis (d-) and a quadrature axis (q-) of the machine are electromagnetically defined. The d- axis is the primary axis of which the permanent magnet flux density flows. The magnet flux density flows through the magnet into the central rib of the magnet pole, into the airgap, through the stator teeth and yoke, and

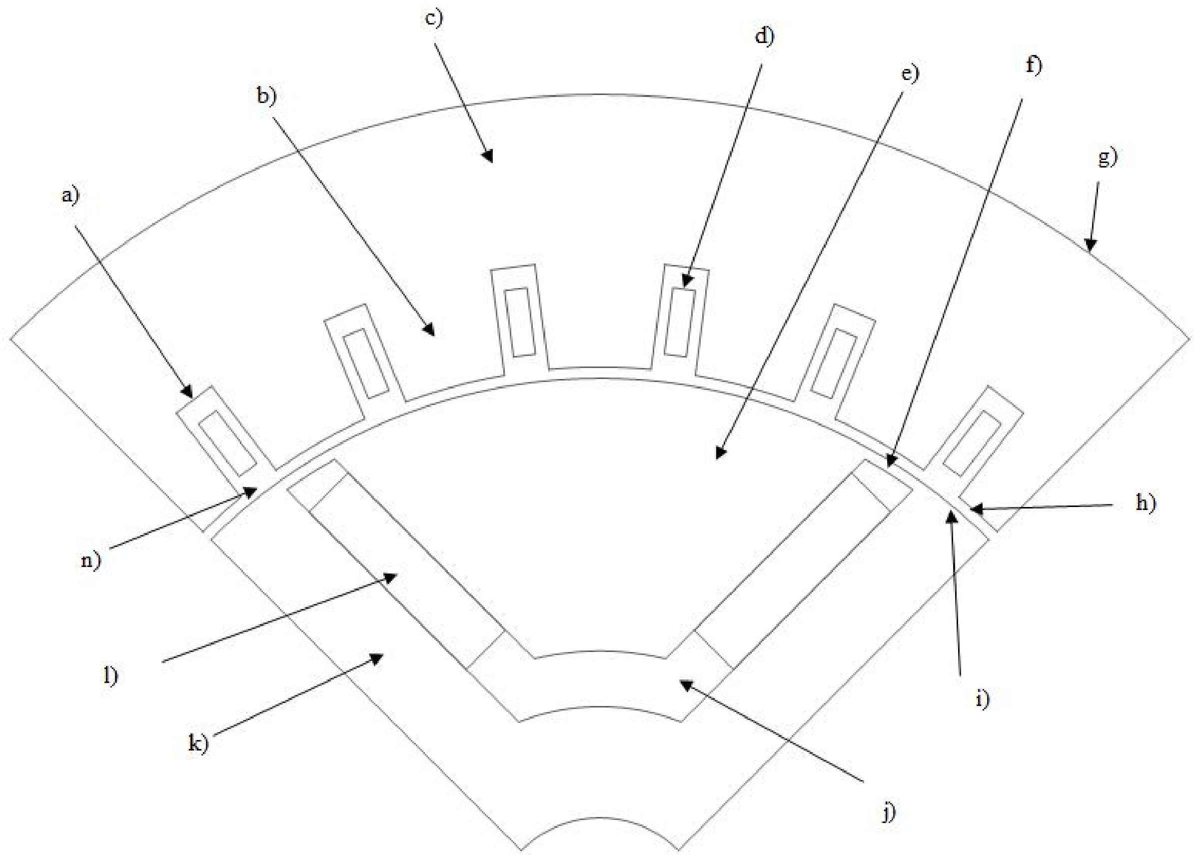

Figure 1.2: A Single Pole of an Interior Permanent Magnet Machine: a) slot, b) tooth, c) stator yoke, d) winding/conductor, e) rib (secondary reluctance path), f) bridge, g) stator OD, h) stator ID, i) rotor OD, j) barrier, k) rib (primary reluctance path), l) magnet, n) airgap

returns into the adjacent opposite magnet pole. This permanent magnet flux density path is shown in 1.1 as a red ellipse. The q- axis is the axis in which the armature-induced flux flows. This flux is produced from the armature MMF. Two paths result in armature induced, one through the primary reluctance path, and a second through the secondary reluctance path. The primary reluctance path flux is shown as the solid blue ellipse and the second reluctance path flux is shown as the dashed blue ellipse.

1.3.3 Rotor Modifications

Rotor sculpting among other design features is usually left to trial and error techniques rather than analytical methods which could provide more insight. Researchers have investigated rotor modifications to alter the airgap, modify airgap flux, and improve torque harmonics. The first feature type is pole shaping, which creates a small airgap near the d-axis and an increased airgap in the region of the q-axis. The torque ripple was reduced for the single magnet flat magnet IPM and optimized with a differential evolution algorithm and finite elements [34]. A surface-mount PM pole-shaped machine was studied with an analytical solution to the field in [35]. The 2D solution was confirmed both by finite element and testing. The pole-shaped single flat magnet IPM was optimized with a response surface method within FE [36]. This included the use of rotor core modifications as well; both FE and experimental results were presented. The flat magnet IPM pole shape was optimized, along with the creation of design rules for the ratio of q-axis and d-axis airgap length in [37]. The single V magnet-shape IPM was improved with pole shaping using finite elements in [38]. Cogging torque and back emf were measured. A third harmonic was added to the pole shape in [39], which studied the machine in finite elements. A second feature type is in the rotor core, which creates a small hole in the rotor core near the airgap to redirect flux. Holes in the rotor core's second reluctance path of the single magnet IPM were shown to decrease torque ripple using finite elements in [40]. The double V magnet IPM machine with improved torque ripple, due to holes in rotor iron core and rotor surface sculpt features, was shown to improve torque ripple but lower average torque in [41]. The delta magnet IPM shape included modified internal rotor features to improve for average torque and decrease iron loss in [42].

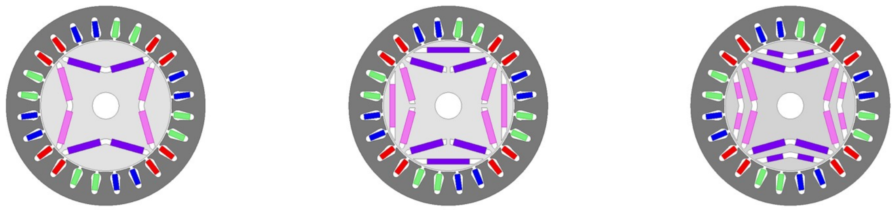

Figure 1.3: IPM rotor types: single V (**left**), delta (**center**), double V (**right**).

The third and final feature type is sculpting the rotor surface at the airgap to redirect flux. The single flat magnet IPM machine cogging torque was reduced in [43] and experimentally verified. Figure 1.4 shows a rotor pole with sculpted features. A grid on/off optimization of the rotor surface was conducted on the single flat magnet IPM using finite elements in [44,45], resulting in an asymmetric rotor surface with a reduction in torque ripple and maintaining average torque. The double V-magnet IPM torque ripple was minimized with both rotor core and surface sculpted features in [41]. The delta-magnet IPM machine torque ripple was minimized with rotor surface sculpt features in [46]. Then, a general analytical expression for torque harmonics was developed and utilized to optimize the solution with finite elements.

Flux density from the magnet is independent from the armature current, and the flux density from the reluctance path is dependent upon the armature. Torque from the magnet is proportional to the armature current while the reluctance torque is proportional to the square of the armature current. For any given operating point there is minimum current needed at the optimum control angle. Traditionally, the IPM machine design results in this Maximum Torque per Amp (MTPA) at neither the magnet nor salient maximum torque, but at the best combination of the two. Recently researchers have looked into aligning the magnet and the reluctance axis to improve torque and power density of the machine [47–49]. This does not come without compromise as features to shift the magnet flux introduces additional harmonics to the air gap. Alignment through the use of surface features has been

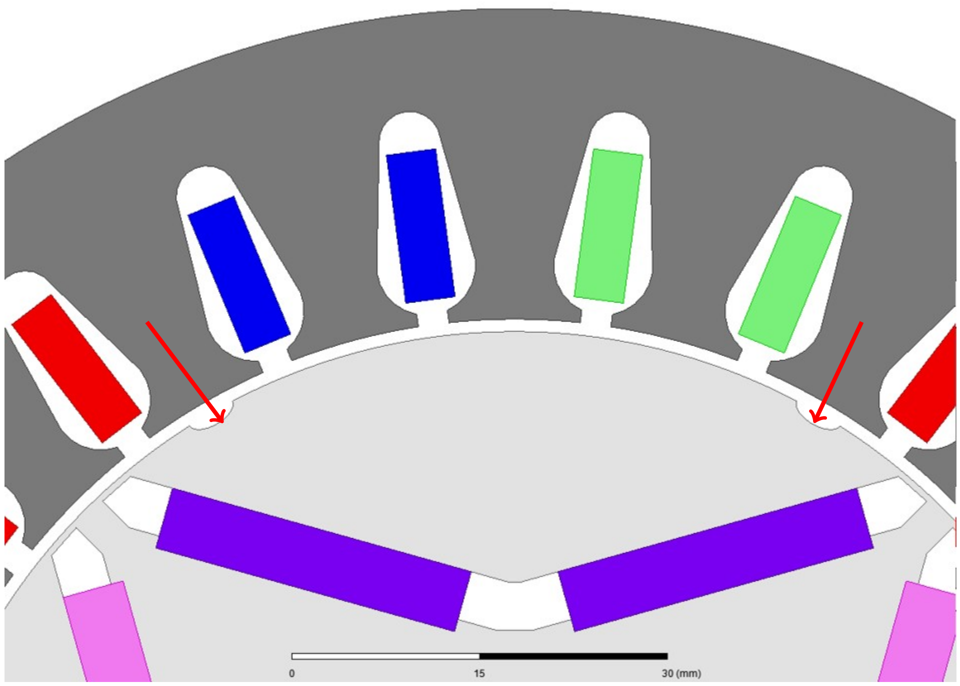

Figure 1.4: Example Interior Permanent Magnet Machine with Rotor Sculpt Features

shown to provide harmonic amplification of the permanent magnet flux density and overall torque production [50].

1.3.4 Analytical Methods

Analytical expressions for the airgap and torque harmonics are developed for the IPM in [51, 52]. The synchronous reluctance of torque harmonics presented in [53] is extended to the IPM machine in [52]. The expressions are useful in setting the stator slot and rotor barrier counts but do not model the machine.

Analytical models build intuitive relationships between the physical geometry of the machine to its airgap and flux density harmonics. Directly solving the Laplacian–Poisson is difficult [54, 55]. Subdomain models break the model into pieces in which the Laplacian–Poisson can be more readily solved [56, 57]. Magnetically Equivalent Circuits (MEC) divide the geometry into smaller manageable pieces [58]. Methods depending on winding functions allow for the geometry and harmonics to be described, but the second reluctance path can be difficult to model. The airgap harmonics of the salient pole permanent magnet synchronous machine are presented in [59] but does not address torque ripple or the secondary reluctance path of the IPM machine. The rotor permeance path is approximated in [60] to determine the torque ripple of the machine under study but does not fully describe an IPM machine. The double V shaped IPM is presented in [61], in which flux densities are calculated through a MEC model and described with a Fourier series. The single V IPM presented in [62] considers the pole cap effect but does not consider torque ripple harmonics. The single V, delta and double V IPM rotor configurations are shown in Figure 1.3. Moreover, the airgap harmonics in permanent magnet synchronous machines were calculated in [63, 64], but the effect of the second reluctance path on the airgap harmonics was not included in the calculations.

The flux density in the air gap is used to compute the main proprieties of an electric machine, such as flux linkage, back-EMF, inductance, forces, and torque. Analytical, magnetic equivalent circuit (MEC), and finite element methods can all be used to calculate the air gap fields for both permanent magnet and armature excitations. Analytical methods [65] are primarily based upon direct solutions of Maxwell's Equations. Often idealization of the geometry and material properties is utilized, leading to inaccurate results. As geometries and material properties become more complex analytical methods become prohibitively difficult. The magnetic equivalent circuit method subdivides the magnetic and electric fields into circuits of permeances and MMFs [66]. Carefully placed permeance or reluctance elements allow flux to flow in predetermined directions. Geometry, time harmonics, and saturation are then calculated at a reduced fidelity with reasonable speed. The finite element method solves the partial differential equations by subdividing the complex geometry into many elements [67]. The full detail of geometry, windings, and material nonlinearity can be considered. The finer the mesh and time step, the more accurate results can be obtained. Increased accuracy comes at the expense of time and cost.

Recent research has been conducted in the application of MMF permeance theory to various machines, including switched reluctance, doubly salient synchronous reluctance, surface mount permanent magnet, synchronous reluctance, and the interior permanent magnet machine. Cogging torque and acoustic noise were studied and minimized for the surface permanent magnet machine in [68]. A modulator function was utilized in conjunction with MMF-Permeance theory was used to develop a general formulation spanning multiple machines [69]. Air gap flux density was computed for the embedded surface mount machine in [59]. A mixture of analytical and finite element techniques was used to compute complex permeances and air gap pressure models to conduct a detailed NVH study [70]. Synchronous reluctance rotors with a primary salient feature were presented in [71] and [72]. No load operation of the flux switching machine was investigated in [73] utilizing MMF permeance theory. Torque production of the doubly salient synchronous reluctance machine was studied in [74]. Han, Jahns, and Soong studied the interior permanent magnet machine, using a simplified model MMF permanence model, to relate the torque ripple of the armature MMF and magnet MMF interaction [51]. Dutta, Rahman, and Chong studied the inductance properties of the interior magnet machine, focusing on the primary reluctance path [75]. The importance of considering the equal potential pole cap effect of the second reluctance path was presented in [62], while focusing on the calculation of the inductance. Later the same authors followed up extending the method to the calculation of magnet eddy current losses [76]. Inductance properties of interior permanent magnet machines are studied in [77].

The reluctance portion of the IPM machine is studied by partitioning the design into d- and q- axis components in [78]. Torque calculation of a five phase IPM machine is performed in [79] using a new Lorentz force method, utilizing a combined magnetic equivalent circuit and permeance model. A novel rotor design is presented and the open circuit back emf properties are investigated in [15].

1.3.4.1 Review of Recent Analytical Models

The analytical MEC model is used to design a reduced magnet cost single V consequent pole (CP) machine with the same average torque as single V IPM in [17]. The models are developed based on zones and regions, allowing for an assumption of the open circuit flux density distribution. Two flux sources (magnets) and six reluctance network paths are used to create the open circuit single V IPM model. Open circuit flux density is assumed to take a trapezoidal waveform where the flux density is determined spatially from the fluxes in the MEC reluctance network. Similarly, the single V CP IPM network consists of one magnet flux source and five reluctance paths. In both cases, the rotors reluctance path reaction to the armature loading is not computed. The open circuit flux densities are used to quickly determine an equivalent single V CP IPM fundamental to that of the single V IPM fundamental. To guide design, the method is used to find an equivalent consequent pole open circuit flux density fundamental to the traditional IPM flux density. Finite elements are relied on to complete the study of the torque performance.

Multi-barrier synchronous reluctance and Permanent Magnet Assisted Synchronous Reluctance Machines (PMSynRM) are modeled using conformal mapping and magnetic equivalent circuits in [22]. Hyperbolic shaped flux barriers are assumed. Conformal transformations are employed to the rotors flux barrier geometry to compute the magnetic reluctance. The reluctance values calculated from conformal mapping are subsequently used in the reluctance network values of the MEC model. The MEC model considers MMF sources of both the armature and magnet. Loaded and open circuit flux densities, average torque, and torque ripple are compared to finite elements with reasonable accuracy.

The slotless U-type IPM machine open circuit flux density is analytically modeled with a subdomain method solving Laplace's and Poisson's equations in [21]. Analytical equations are derived and presented for each subdomain. Results are validated against finite elements. The model is divided into four regions, which consist of the airgap and magnets. The governing system of partial differential equations is developed, along with simplifications, interface, and boundary conditions. Separation of variables is used to develop the general solutions of the PDEs, and they are written as a Fourier series. The system of equations is solved and compared to FE. Strong agreement of the radial and tangential flux density is shown between the FE and the subdomain methods.

The analytical models discussed were developed for multiple purposes. The MEC method is used in [17] to quickly estimate the open circuit flux density fundamental of the single-V IPM and single-V CP IPM machines. The armature reaction of the reluctance features is not considered by the model, and finite elements are used to finish the designs. Conformal mapping is used in [22] to determine the reluctance of a multi-barrier PMSynRM and further evaluated using a MEC network. Both open circuit and loaded conditions are evaluated for airgap flux densities and torque performance and compared to finite elements. The analysis is not extended to the design. The subdomain methodology is employed in [21] for the analysis of the U-shape IPM machine open circuit conditions. Both tangential and radial flux densities are shown to match finite element results. The model requires further extension to consider the torque performance due to a loaded armature.

1.4 Organization of Thesis

Development of the fundamental magnetic model of IPM machine is presented in Chapter 2. This fundamental model is made up of sinusoidally distributed wingdings, a doubly sinusoidal salient rotor, and permanent magnets. Analysis resulting from the geometry, including torque, flux linkage, and inductance is developed. The governing differential equations of voltage and output equation of torque are developed for the case of the traditional alignment of magnets and for the case where the magnet axis is better aligned to produce torque coincident with the reluctance path in chapter 3. MMF permeance theory is presented in chapter 4 developing the necessary theory for IPM machines and sculpted rotor features. An example machine is presented along with components of torque contributed from the primary reluctance path, secondary reluctance path, and magnet path. Chapter 5 develops the analysis of torque harmonics and the contributions of the various components. Chapter 6 presents features enabling mitigation of torque ripple. Chapter 7 develops a design methodology based on MMF-Permeance theory to improve intuition and reduce design iterations. A design of a machine is presented with a comparison of MMF-Permeance to linear finite element theory results.

Chapter 2

Fundamentals: Magnetics

Rotating electric machines are built from two primary parts: a stator and a rotor. The stator is the stationary part, containing a multi-phase winding or armature, and a magnetically permeable iron core. The rotor is the rotating component, containing permeable iron salient features and a permanent magnet. The cylindrical rotor is surrounded by a cylindrical air gap and further contained within the cylindrical stator.

The stator, fed by winding alternating current, produces a rotating magneto-motive force (MMF) at its bore. The MMF interacting with the stator's permeable iron core, the rotor's permeable iron salient features, and the air gap, produces, a radial air gap flux density. In addition, the permanent magnets of the rotor interact with the same structure adding radial air gap flux density. The stator three phase winding, located close to the inner bore of the stator, also produces a tangential magnetic field, related to the linear current density of the winding. The tangential magnetic field interacts with the radial flux density, as shown in figure 2.1, to produce torque. The portion of this torque due to the air gap radial flux density of the magnet is referred to as 'magnet torque'. The air gap radial flux density associated with the salient portions of the rotor produce 'reluctance torque'. These torque components, composed of the product of current, i_d and i_q, and flux terms, can be observed within the

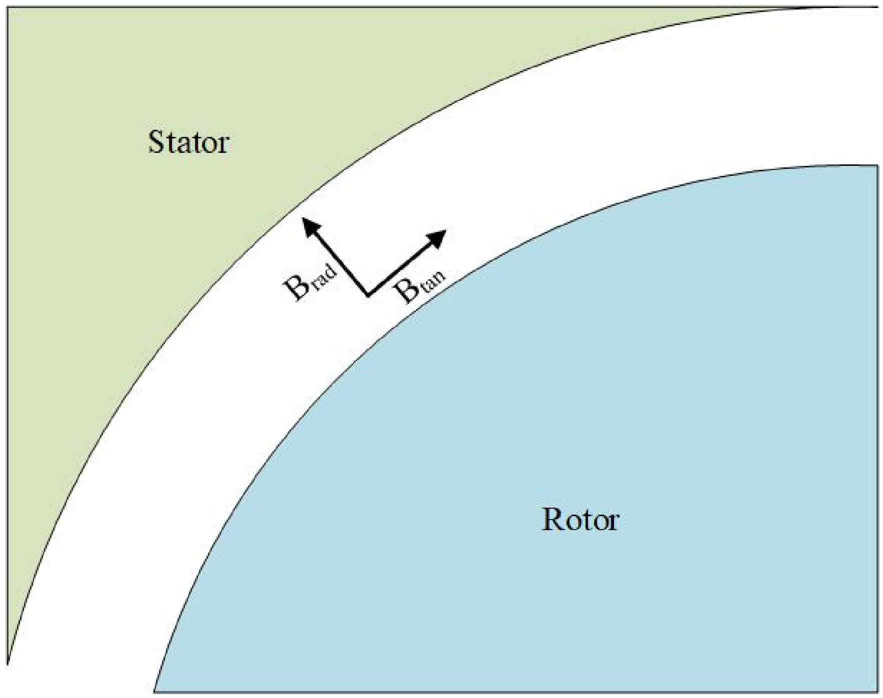

Figure 2.1: Radial and Tangential Flux Density in Air Gap

torque equation of the interior permanent magnet machine eq. (2.1).

$$T = \frac{1}{2}\frac{3}{2}\Big((l_d - l_q)i_d i_q + \lambda_m i_q\Big) \tag{2.1}$$

The radial flux densities of the air gap pass through the three phase windings of the stator. Each phase of the winding links the radial flux density, resulting in a magnet flux linkage and a reluctance flux linkage (or inductance term) for each phase. The individual phase inductance and magnet flux linkage will be dependent on the rotor's angular location within the stator. As the rotor spins with an angular velocity, the changing flux linkages of the windings produce an electromotive force (EMF). The permanent magnet term of voltage is only dependent on rotational speed. The inductive term is dependent upon both rotational speed and the current through the winding.

These processes are fundamentals of electromechanical energy conversion for rotating electric machines. In the remainder of this section, these ideas will be expanded with models based on first principles and their results.

2.1 Stator with Sinusoidally Distributed Windings

Sinusoidally distributed windings are an ideal distribution of windings, physically not possible to achieve, but the concept allows for the first analysis of the machine. The sinusoidal distribution neglects the harmonic content of distributed windings and focuses the analysis on the fundamental components. Each phase of the machine can be described starting with a conductor density function $n(\theta)$ with $\hat{n_x}$ defining the peak density of the winding over the stator bore and p the number of pole pairs of the electric machine, as shown in equation 2.2. For this section, we will assume the machine has $p = 1$ pole pairs. This equation is directly applicable to Phase A. Phase B and Phase C will be offset by 120° and 240° respectively. The linear current density is a product of current (I_a, I_b, and I_c) , total number of turns ($\hat{n}_a$, $\hat{n}_b$, and $\hat{n}_c$), and angular location θ. Since the conductor density has a sinusoidal form, the linear current density will be similar, with the linear current density K_x, shown in eqs. (2.3) to (2.5). A 2-pole stator constructed with sinusoidally distributed current sheets is shown in Figure 2.2 where each sinusoidal current sheet distributes the current over the inner surfaces of the annulus.

$$n_x(\theta) = \hat{n}_x sin(p\theta) \tag{2.2}$$

$$K_a = i_a(\frac{\hat{n}_a}{2})sin(\theta) \tag{2.3}$$

$$K_b = i_b(\frac{\hat{n}_b}{2})sin(\theta - \frac{2\pi}{3}) \tag{2.4}$$

$$K_c = i_c(\frac{\hat{n}_c}{2})sin(\theta + \frac{2\pi}{3}) \tag{2.5}$$

Each phase has it's own set of current sheets. Phase A is a current sheet with the maximum current going into the page at 270° and the same maximum current coming out of the page at 90°. Likewise, phase B and C current sheets are sinusoidally distributed but aligned 120° apart from phase A.

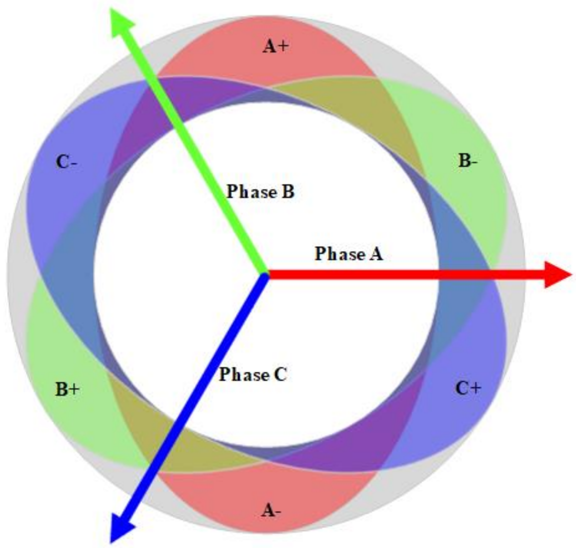

Figure 2.2: Sinudsoidally Distributed Three Phase Windings

2.2 Salient Rotor Geometry Analysis

A doubly sinusoidal airgap is used to model the salient reluctance path. This creates a rotor shape that has opposite ends close to the stator in one dimension, and far away from the stator in the other dimension. This shape provides a salient feature the stator's magnetic field can pull on.

To define a doubly sinusoidal air gap, the rotor shape has to be modeled. The variable θ is the angular coordinate along the stator bore, and ϕ is the position of the rotor. The rotor is defined by these variables in eq. (2.6), where R_{rot} is the rotor radius, R_{sta} is the stator radius, and g_{nom} is the nominal air gap.

$$R_{rot} = (R_{sta} - g_{nom} - A) + A\cos(2\theta - 2\phi) \tag{2.6}$$

The air gap due to the salient rotor geometry is the difference between the inner radius of the stator and the radius of the salient rotor.

$$g = R_{sta} - R_{rot} \tag{2.7}$$

The rotor geometry is shown in fig. 2.3.

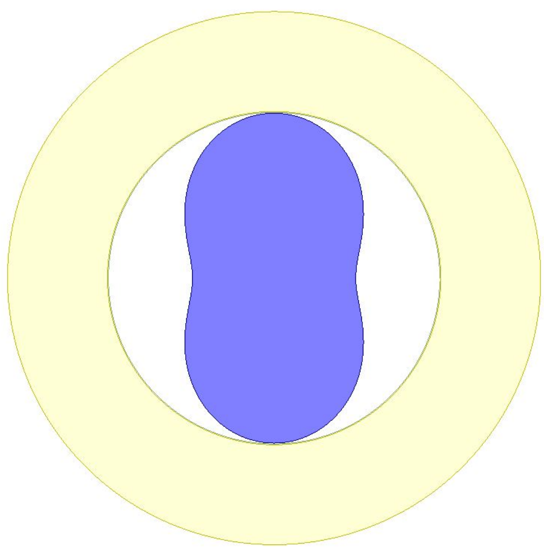

Figure 2.3: Doubly Sinusoidal Air Gap: The salient rotor is shown in blue and the stator in yellow.

The air gap function g defines the salient rotor within the armature. Ampere's Law, eq. (2.8), is used to calculate air gap flux. It states that for any closed loop the sum of the magnetic field in the direction of the length elements is equal to the electric current enclosed in the loop. In basic terms, the magnetic field in space around an electric current is proportional to the electric current which serves as its source. The reluctance portion of the air gap flux is calculated from the rotor shape using Ampere's Law. To simplify the calculation a few assumptions are made:

- air gap flux only flows radially
- the stator and rotor iron have infinite permeability
- the air gap has the permeability of free space
- all materials are homogeneous and linear (no saturation)
- as a result, the magnetic field in the stator and rotor is negligible.

$$\oint_l H dl = \int_S J dS = \sum I \tag{2.8}$$

A suitable integration path must be chosen. The integration path is chosen such that it encloses currents and cuts through the air gap. The portions of the integration path that extend through the air gap are radially oriented. Radial orientation in the air gap follows the flux path which will result in direct calculation of this quantity. To consider the driving currents to form a closed loop the integration path must cross the air gap in two places. If the air gap is different lengths or the materials enclosed are not homogeneous calculation of the air gap flux is complicated. In this case, we will further simplify by choosing a path that maintains equal air gap length on both sections crossing the air gap. To meet all these requirements the path shown in figure 2.12 is chosen. Since the stator is made of material with infinite permeability, $H_{iron} = 0$, Ampere's law for a phase becomes eq. (2.11). The magnetic field for any angular position can be determined and the radial flux density can be computed using the constitutive equation eq. (2.12).

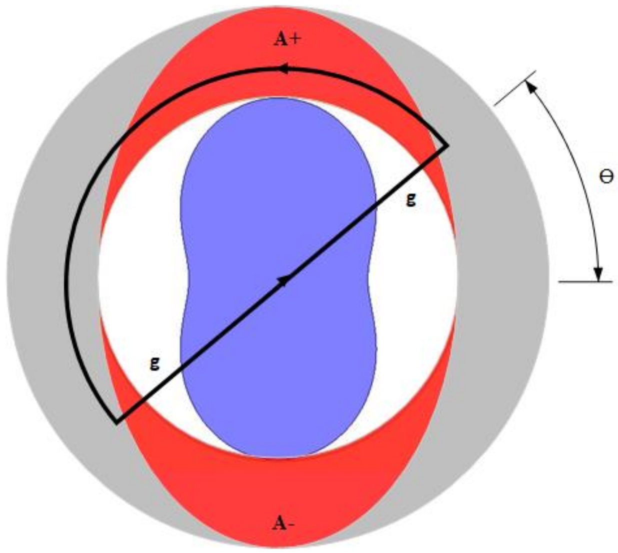

Figure 2.4: Integration Path for Ampere's Law, Current Sheet (red)

$$\int_S JdS = \int_{\theta_1}^{\theta_2} i_1 \frac{\hat{n}_{s1}}{2} sin(\theta) r d\theta \tag{2.9}$$

$$H_{g1}(\theta) \cdot 2g_{air}(\theta) = -i_1 r \frac{\hat{n}_{s1}}{2} cos(\theta)\Big|_{\theta_1}^{\theta_2} \tag{2.10}$$

$$H_{g1}(\theta) = \frac{-i_1 r \frac{\hat{n}_{s1}}{2} cos(\theta)\Big|_{\theta}^{\theta+\pi}}{2g_{air}(\theta)} \tag{2.11}$$

$$B = \mu_o H \tag{2.12}$$

2.3 Permanent Magnets

2.3.1 Permanent Magnet Properties and Equivalent Current

Permanent magnet materials can be described in terms of three vector quantities [80]. The flux density, **B**, (or magnetic induction) describes the concentration and direction of magnetic flux at a point in space. The magnetic field vector, **H**, describes the field in space created by a current through a wire. The magnetization vector, **M**, describes the internal state of the magnet. The units for each property are listed below.

- B is flux density units T
- H is magnetic field $\frac{A}{m}$
- M is magnetization $\frac{A}{m}$

These three vectors are related through their constitutive relationship, which can also be re-written in terms of the polarization vector **J** with units of T.

$$\vec{B} = \mu_0 \vec{H} + \mu_0 \vec{M} = \mu_0 \vec{H} + \vec{J} \tag{2.13}$$

Alone, this constitutive equation is not enough to describe the behavior of a permanent magnet; the non-linear properties including hysteresis must be considered. Figure 2.5 shows a typical magnetization curve for a permanent magnet, where the horizontal axis is the magnetic field and the vertical axis is the magnetization. Starting at no magnetization and no field, the origin of the graph, the magnetic field is increased and the magnetization increases. As the field is increased further, the magnetization begins to saturate. This point, H_s, is called the magnetic field saturation point. Continuing to increase the magnetic field, the magnetization fully saturates at the point M_s. Once the magnetization is fully saturated, the magnetic field is reduced to constant. The magnetization does not follow the original trajectory but settles at the point B_r. This point is called the residual flux density. The residual flux density is also the point where the magnetization equals the flux density. The process described is completely within the first quadrant and is the process used to magnetize a permanent magnet. The second quadrant is where the magnet operates in an electric machine. The residual flux B_r and the intrinsic coercivity H_{ci} are the key points that define the operation of the magnet within the second quadrant.

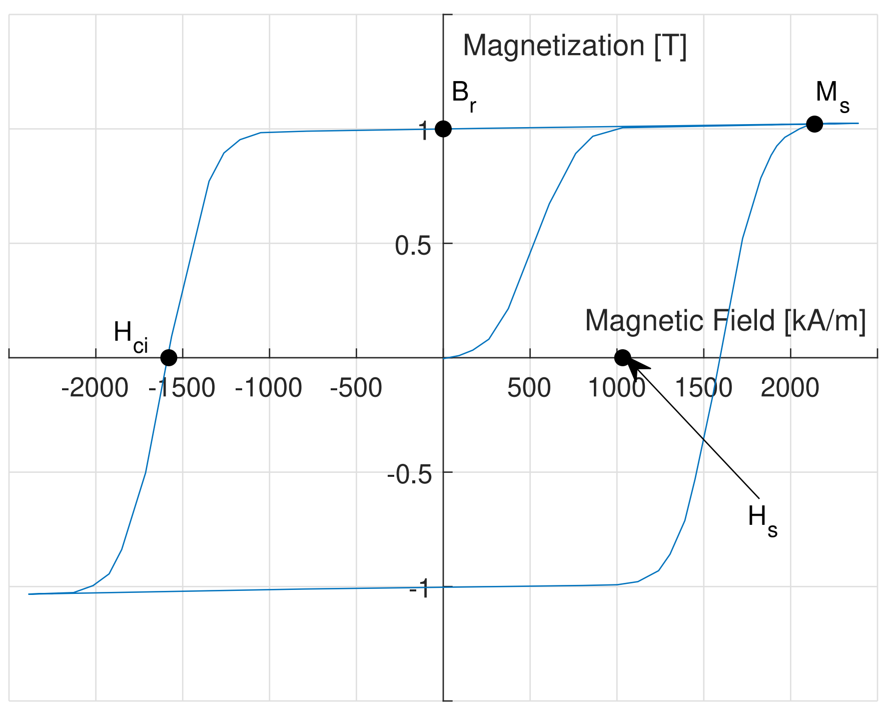

Figure 2.5: Magnetization Curve [1]

Magnet operation within the second quadrant is shown in figure 2.6, it shows the flux density and magnetization of the magnet eventually reduce to zero as the field becomes increasingly negative. The second quadrant is where the magnet operates within an interior permanent magnet machine, this is due to both the machines air gap and the loading from the armature. A simple circuit consisting of coils, a magnet, infinitely permeable steel, and

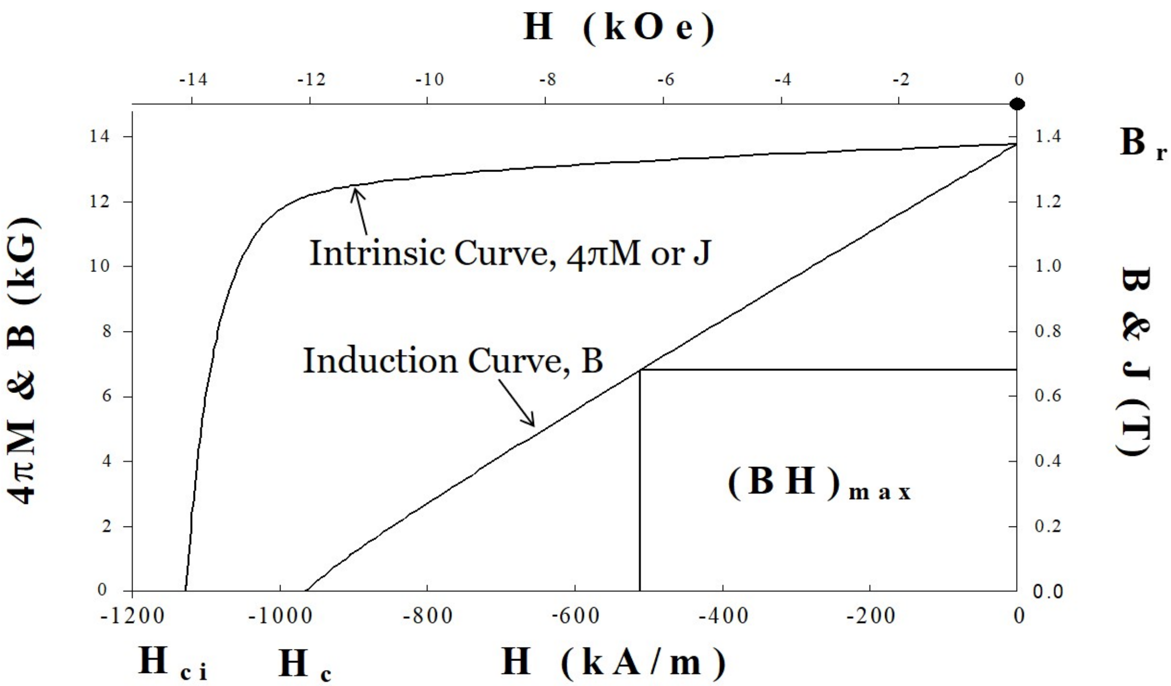

Figure 2.6: Demagnetization Curve [1]

an airgap is effective in describing the operation of the magnet within an interior permanent magnet machine [80]. This circuit is shown in figure 2.7 and is further idealized in equation set 2.14.

$$\begin{aligned} \mu_0 M_s = J_s \geq & \quad B_r \\ B_r \geq & \quad \mu_0 H_c \\ H_{ci} \geq & \quad H_c \\ (B_r/2)^2 \geq & \quad \mu_0 (BH)_{max} \end{aligned} \tag{2.14}$$

Assuming no flux leakage in the magnet reluctance circuit, it can be described with equation set 2.15. First among these equations are the magnet voltage drops of the magnet and the air gap. Next continuity of total flux across both magnet and airgap must be maintained.

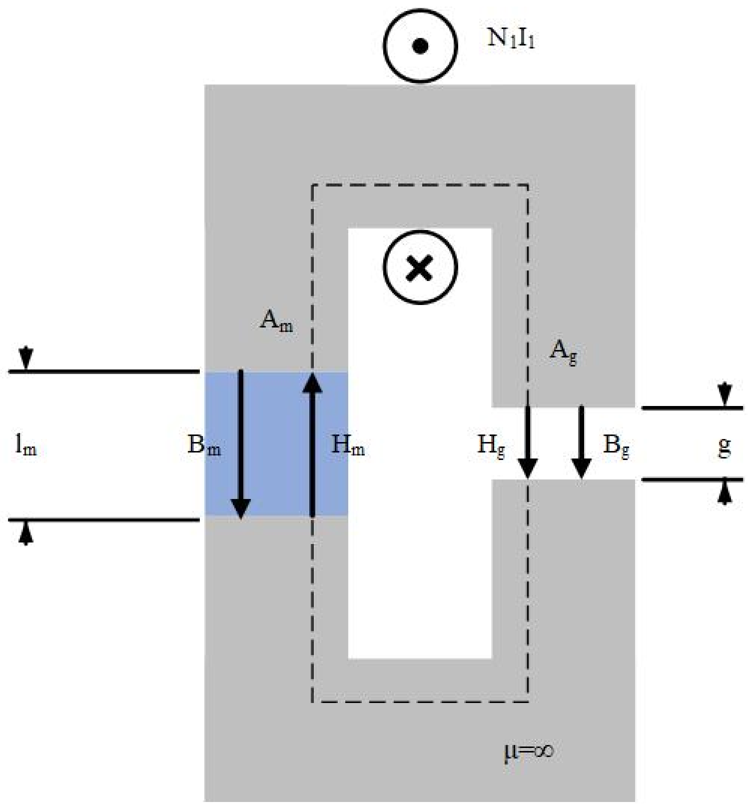

Figure 2.7: Permanent Magnet Model: A_m area of magnet, A_g area of gap, B_m magnet flux density, H_m magnet field strength, B_g airgap flux density, H_g air gap field strength, l_m length of magnet, g length of airgap, N_1I_1 amp turns

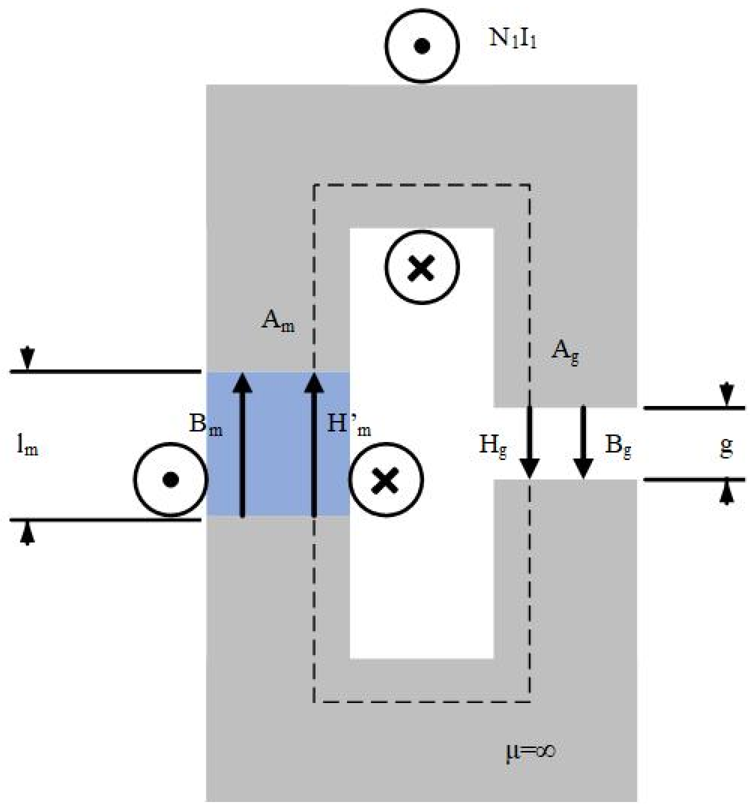

Figure 2.8: Equivalent Current Permanent Magnet Model: A_m area of magnet, A_g area of gap, B_m magnet flux density, H'_m magnet field strength, B_g airgap flux density, H_g air gap field strength, l_m length of magnet, g length of airgap, N_1I_1 amp turns

Finally the constitutive equations for the magnet and the the airgap.

$$\begin{aligned} H_m l_m + H_g g &= N_1 I_1 \\ B_m A_m &= B_g A_g \\ B_g &= \mu_0 H_g \\ B_m &= B_r + \mu_0 \mu_r H_m \end{aligned} \tag{2.15}$$

The load line equation, eq. (2.16), is obtained by solving the first of set eq. (2.15). The load line is used to solve for the magnet flux density as a function of magnetic field for each current.

$$B_m = u_0 \frac{A_g}{g A_m}(-H_m l_m + N_1 I_1) \tag{2.16}$$

The magnet constitutive equation can be further simplified by rewriting in terms of $H_m^{'}$.

$$B_m = \mu_0 \mu_r (\frac{B_r}{\mu_0 \mu_r} + H_m) = \mu_0 \mu_r (H_m^{'}) \tag{2.17}$$

$$\begin{aligned} H_m^{'} l_m + H_g g &= N_1 I_1 + \frac{B_r}{\mu_0 \mu_r} l_m \\ B_m A_m &= B_g A_g \\ B_g &= \mu_0 H_g \\ B_m &= \mu_0 \mu_r H_m^{'} \end{aligned} \tag{2.18}$$

$$N_f I_f = \frac{B_r}{\mu_0 \mu_r} l_m \tag{2.19}$$

The system of equations are now re-written and solved to find the equivalent coil current, equation 2.19, and the four unknowns $H_m^{'}$, H_g, B_m, and B_g. This equivalent coil current gives way to represent a system of magnets as a single phase coil wound around a material with the same permeability as the magnet.

2.3.2 Simplified Permanent Magnet Analysis

The permanent magnet's ability to hold flux density is due to its large hysteresis properties. A demagnetized magnet will begin with properties at the origin of a magnetization curve with no flux density and no field strength. To magnetize a magnet a large positive magnetic field H will need to be applied and as a result, the flux density will increase. Upon relaxation of the magnetic field $H = 0$ the magnetized magnet flux density will settle at its remnant value B_r. To bring the magnet back to zero flux density will require a negative magnetic field applied equal to the magnet's coercivity level H_c. Figure 2.9 shows the operating portion of a B-H curve for a magnetized magnet. In most cases the second quadrant is where the

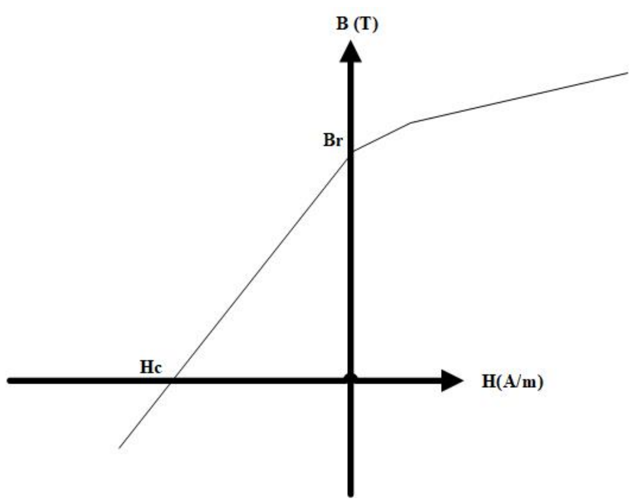

Figure 2.9: Magnet Properties

magnet will operate.

A simple framework is described first beginning with conservation of the magnet flux, Φ and MMF F. Equation 2.20 considers the remnant flux Φ_r, the flux which does not cross the airgap (leakage) Φ_σ, and the flux entering the magnetic circuit air gap Φ_g. Equation

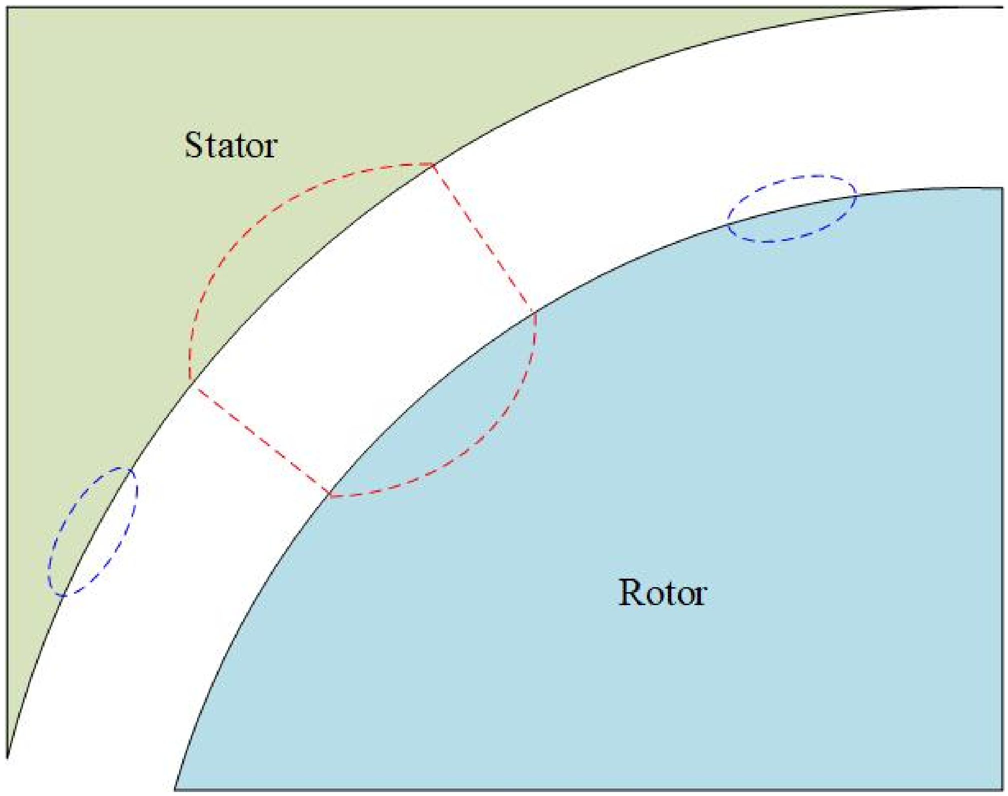

Figure 2.10: Flux Paths: Crossing the Air Gap (red) , Leakage (blue)

2.21 sums the MMFs of the leakage and air gap terms, where R_g is the reluctance to cross the airgap, and R_σ is the leakage reluctance.

$$\sum \Phi = 0 : \Phi_r - \Phi_\sigma - \Phi_g = 0 \tag{2.20}$$

$$\sum F = 0 : \Phi_g R_g - \Phi_\sigma R_\sigma = 0 \tag{2.21}$$

The resulting MMFs can be expressed in terms of each other and fed back into the conservation of flux.

$$\Phi_g = \frac{\Phi_\sigma R_\sigma}{R_g} \tag{2.22}$$

$$\Phi_\sigma = \frac{\Phi_r}{1 + \frac{R_\sigma}{R_g}} \Phi_r \tag{2.23}$$

The remnant flux, Φ_r, is related to the remnant flux density , B_r, multiplied by its area.

$$\Phi_r = B_r A = B_r L(\Delta\theta)r \tag{2.24}$$

The reluctance of the leakage term, R_σ is related to the magnet thickness l, coercivity of the magnet H_c, and remnant flux. The air gap reluctance is tied to the airgap of the machine, g, permeability of free space, $\mu_\circ$, and area A.

$$R_\sigma = \frac{H_c l}{B_r A} = \frac{H_c l}{B_r L(\Delta\theta)r} \tag{2.25}$$

$$R_g = \frac{1}{\mu_\circ}\frac{g}{A} = \frac{1}{\mu_\circ}\frac{g}{L(\Delta\theta)r} \tag{2.26}$$

With these few assumptions, the magnet leakage and the air gap flux density can be computed as:

$$B_\sigma = \frac{B_r}{1 + \mu_0 \frac{H_c l}{B_r g}} \tag{2.27}$$

$$B_g = B_r - B_\sigma \tag{2.28}$$

This models the magnet flux to be dependent on air gap, magnet thickness, coercivity, and remnant flux.

2.4 Magnetic Dipole and Equivalent Magnetic Currents

The study of magnetic fields in free space begins with a subset of Maxwell's equations consisting of Gauss's law 2.29 of magnetism and Ampere's law 2.30. Both can be rewritten in their respective integral form 2.31 and 2.32 made possible through the divergence theorem.

$$\nabla \cdot \boldsymbol{B} = 0 \tag{2.29}$$

$$\nabla \times \boldsymbol{B} = \mu_0 \boldsymbol{J} \tag{2.30}$$

$$\oint_S \boldsymbol{B} \cdot d\boldsymbol{s} = 0 \tag{2.31}$$

$$\oint_C \boldsymbol{B} \cdot d\boldsymbol{l} = \mu_0 I \tag{2.32}$$

Gauss's law states the total flux through a closed surface must be zero, therefore; a magnetic monopole does not exist and magnetic flux is conserved. Ampere's law states that the magnetic field along a closed path is proportional to the current in which it encloses. Vector calculus provides that in the case of the divergence of a vector field $\boldsymbol{V}$ is zero, a vector field $\boldsymbol{W}$ exist such that $\nabla \times \boldsymbol{W} = V$. This allows for the magnetic field density $\boldsymbol{B}$ to be written in terms of it's vector magnetic potential $\boldsymbol{A}$ as shown in equation 2.33.

$$\boldsymbol{B} = \nabla \times \boldsymbol{A} \tag{2.33}$$

Using 2.30 along with 2.33 and assuming $\nabla \cdot \boldsymbol{A} = 0$ Poisson's equation is formed.

$$\nabla^2 \boldsymbol{A} = -\mu_0 \boldsymbol{J} \tag{2.34}$$

Depending upon the complexity of the problem, a combination of these formulations is used for the solution of the magnetic field. Solutions can be found with Poisson's equation, sub-domain analytical solutions [81], and finite element solutions [82].

The magnetic dipole in free space is needed to develop the idea of equivalent current densities in place of magnetization states. Figure 2.11 shows a magnetic dipole in free space formed by a loop of radius b and current of I. The solution at far fields, when $R >> b$, and solved in spherical coordinates, in terms of magnetic vector potential is shown in 2.35 [4]. Where the magnetic dipole moment $\boldsymbol{m}$ is written as $\boldsymbol{m} = \boldsymbol{a_z} I \pi b^2$.

$$\boldsymbol{A} = \frac{\mu_0 \boldsymbol{m} \times \boldsymbol{a_R}}{4\pi R^2} \tag{2.35}$$

This dipole in free space can be used to explain magnetism at the atomistic level, where

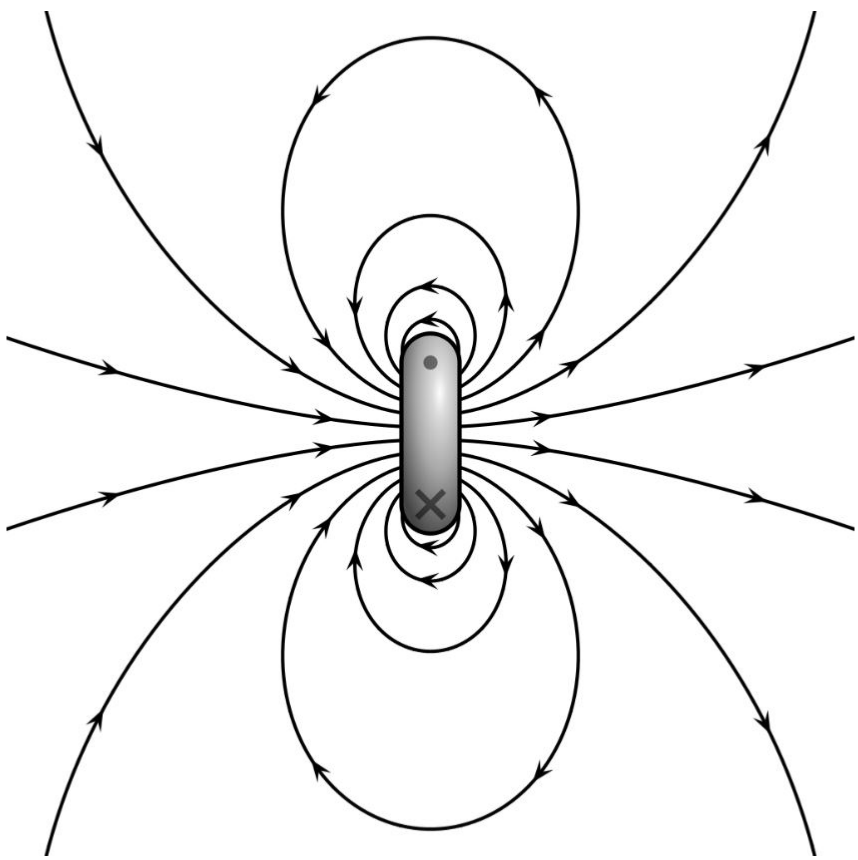

Figure 2.11: Magnetic Dipole From Current Loop [2]

small circulating currents are formed by the process of magnetization. This magnetization aligns the individual dipoles atoms and modifies the orbital spin of the electrons for each atom. The macroscopic volume density of magnetization ,M, with units of A/m, is computed through a sum of the individual microscopic dipoles.

$$\boldsymbol{M} = \lim_{\Delta v \to 0} \frac{\sum\limits_{k=1}^{n} \boldsymbol{m_k}}{\Delta v} \tag{2.36}$$

Shown in [4], the magnetization vector M is equivalent to both a volume current density, $\boldsymbol{J_m}$ with units of $\frac{A}{m^2}$, and a surface current density $\boldsymbol{J_{ms}}$ with units of $\frac{A}{m}$.

$$\boldsymbol{J_m} = \nabla \times \boldsymbol{M} \tag{2.37}$$

$$\boldsymbol{J_{ms}} = \boldsymbol{M} \times \boldsymbol{a_n} \tag{2.38}$$

Given $\boldsymbol{M}$, the flux density B can be found first by computing both $\boldsymbol{J_m}$ and $\boldsymbol{J_{ms}}$ then to determine the magnetic vector potential $\boldsymbol{A}$. Uniform $\boldsymbol{M}$ within a magnetic material will result in no volume current density and only a surface current density J_m on its borders. If space variations of $\boldsymbol{M}$ exist within a material a net volume current density will exist.

In summary, a magnetic dipole can be represented as the sum of equivalent volume and surface current density (Jm and Jms), and utilized as an equivalent magnetization current(EMC). A magnetic dipole inside a material with constant magnetization M can be represented by a current loop formed at the exterior boundary of the dipole.

2.5 Torque Analysis

Torque can be calculated with the Maxwell stress tensor and knowledge of the magnetic fields. It connects the electromagnetic fields and the mechanical forces they produce. It is a tool to compute the air gap torque of an electric machine. Equation 2.39 shows the form of the stress tensor applied to the computation of electric machine torque, where r is the air gap radius, l is the length of the air gap, B_n is the radial air gap flux density, and A is the linear current density of the armature.

$$T = \int_{\theta=0}^{2\pi} r^2 l \cdot B_n(\theta) K(\theta) d\theta \tag{2.39}$$

This equation shows that the torque generated is a product of linear current density and flux density. This equation is used to compute the torque from all sources of flux density, including permanent magnets and the armature. To maximize the permanent magnet contribution to torque the linear current density needs to be simply aligned to the permanent magnet radial flux density. The reluctance flux density will produce maximum torque when the linear current density and the radial flux density are balanced. It can be seen that the net sum of the product B_n and A from equation 2.39 have to be balanced and same signed to produce maximum positive torque. This occurs when the current vector is 45° away from the minimum air gap. This produces the maximum torque by creating the maximum product of linear current density and flux density.

The air gap flux density for the reluctance path can be superimposed for all three phases.

$$B_{rel}(\theta) = B_{g1}(\theta) + B_{g2}(\theta) + B_{g3}(\theta) \tag{2.40}$$

The magnet flux density is superimposed with the reluctance air gap flux densities. For this analysis, the flux density due to the magnet is kept separate to allow for the magnet and reluctance torque to be computed separately. In discrete form, torque equations for reluctance and magnet become eq. (2.41) and eq. (2.42). The reluctance torque and magnet torque can now be added.

$$T_{rel} = r^2 l \sum_0^n B_{rel}(\theta) K(\theta) \Delta\theta \tag{2.41}$$

$$T_{mag} = r^2 l \sum_0^n B_{mag}(\theta) K(\theta) \Delta\theta \tag{2.42}$$

$$T = T_{rel} + T_{mag} \tag{2.43}$$

2.6 Flux Linkage and Inductance

Determination of flux linkage, λ, and inductance L, are required for further analysis and the control of the machine. They are needed for the development of voltage and torque equations. Assuming a previously determined air gap flux density $B(\theta)$, fig. 2.12 illustrates the necessary parameters and variables of geometry to calculate the flux linkage and inductance. The phase windings are constructed with a sinusoidally distributed turns density $n(\theta)$ with a phase vector quantity pointing to the right. The air gap is defined by a rotor of radius r and the gap g. The magnetic flux over a pole, $\Phi(\theta)$, requires integrating the radial flux density over the span [83].

$$\Phi_a(\theta) = \int_{\theta - \frac{\pi}{p}}^{\theta} \mu_0 H_r(\theta) l r d\theta \tag{2.44}$$

The magnetic flux over the pole span in conjunction with turns density $n(\theta)$ allows for the calculation of flux linkage.

$$\lambda_a = \int_{\frac{-\pi}{2p}}^{\frac{\pi}{2p}} \Phi_a(\theta) n_a(\theta) r d\theta \tag{2.45}$$

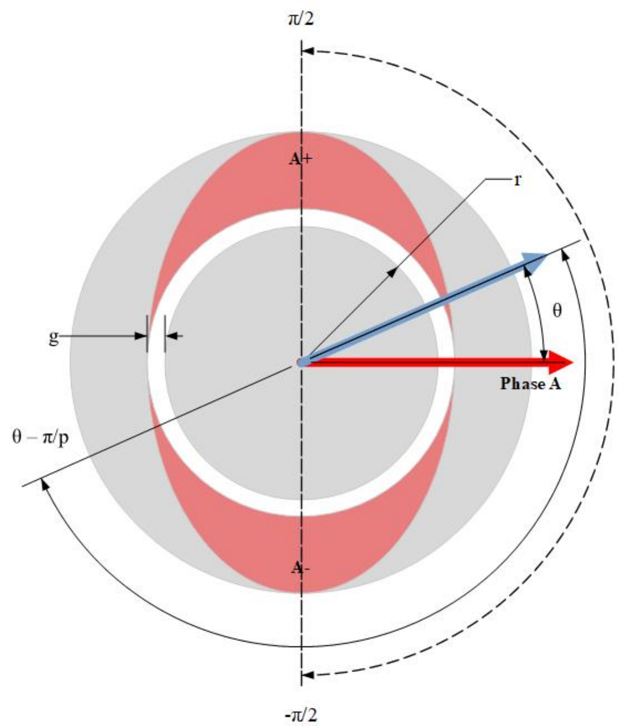

Figure 2.12: Inegration Path for Flux and Flux Linkage

Finally the inductance of the phase is determined by the ratio of flux linkage and current.

$$L_a = \frac{\lambda_a}{i_a} \tag{2.46}$$

2.7 First Analysis of Machine Design

Basic components, shown in figure 2.13, include a permeable toroid, a three phase winding, a permeable salient rotor structure, and a magnet pair. Sinusoidally distributed windings along the inner radius of the toroidal core form the armature. Rotor saliency is achieved through a doubly sinusoidal air gap, equation 2.47, where g_m is the minimum air gap, A_1 is the amplitude of the air gap variance, ϕ is the rotor mechanical position initial offset. Half sinusoidal magnets, defined by equation 2.48, are embedded into the rotor surface where R_m

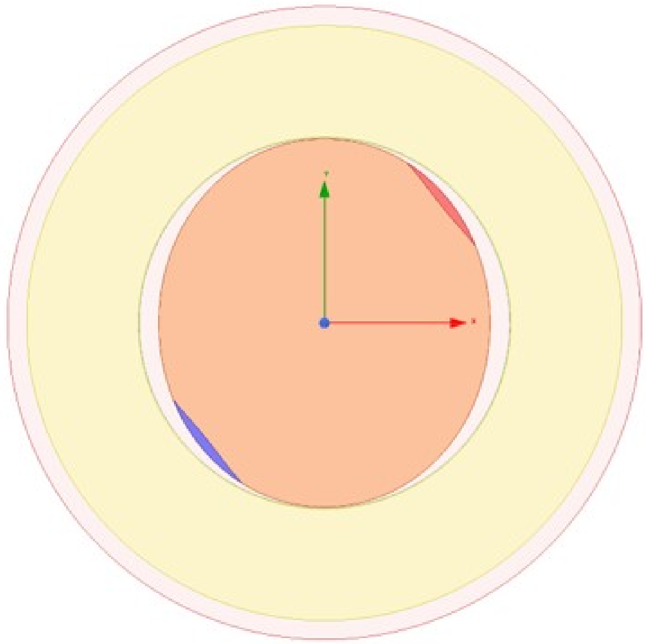

Figure 2.13: Basic Geometry, $\delta = 45^\circ$: toroidal core (yellow), rotor (orange), north magnets(red), south magnet(blue)

is the inner radius of the magnet, A_m is the amplitude of the magnet cutout, and m defines the magnet span. Saliency is designed through the amplitude of the doubly sinusoidal air gap and can be further enhanced through the amplitude of the magnet cutout, the magnet span, and the magnet offset angle. Alignment of the magnet and reluctance torque is achieved through the magnet offset angle δ.

$$R_r = (R_s - g_m - A_1) + A_1 \cos(2\theta - 2\phi) \tag{2.47}$$

$$R_m = R_r - A_m \cos\left[m(\theta - \phi - \delta)\right] \tag{2.48}$$

Resulting torques with traditional alignment, $\delta = 0^\circ$, and non traditional alignment, $\delta = 45^\circ$, are shown in figures 2.14 and 2.15. Magnet and reluctance properties of both cases are the same. For the traditional IPM magnet alignment $\delta = 0^\circ$ it can be seen that the reluctance and magnet torque does not occur at the same current angle. When IPM magnet is aligned at $\delta = 45°$ it can be seen that the reluctance and magnet torque occur at the same current angle and maximize torque production.

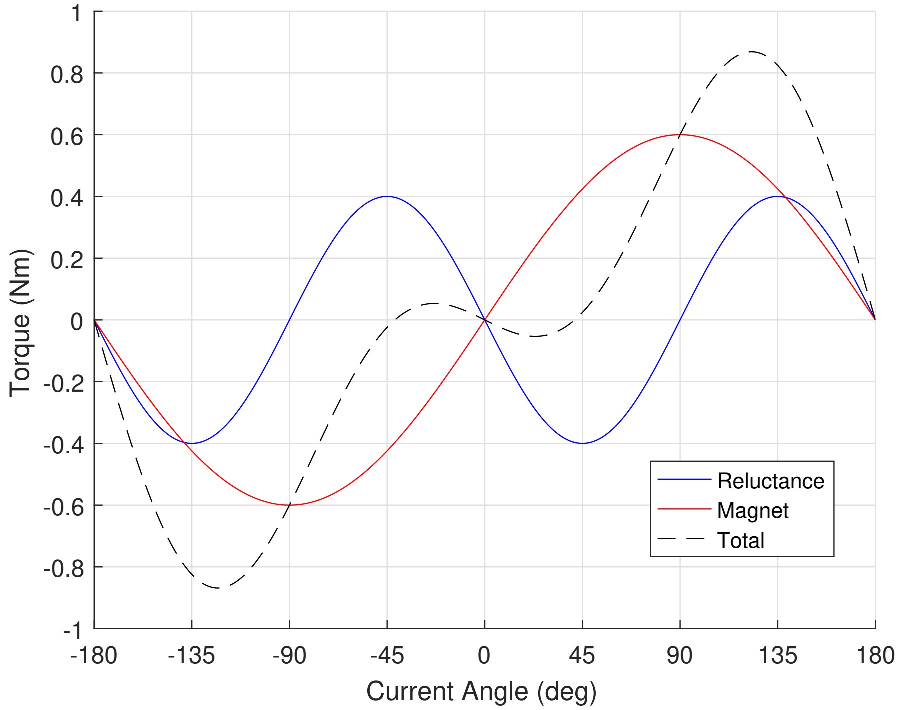

Figure 2.14: Theoretical Torque Versus Current Angle IPM Machine , $\delta = 0°$: Reluctance Torque (blue), Magnet Torque (red), Total (black dashed)

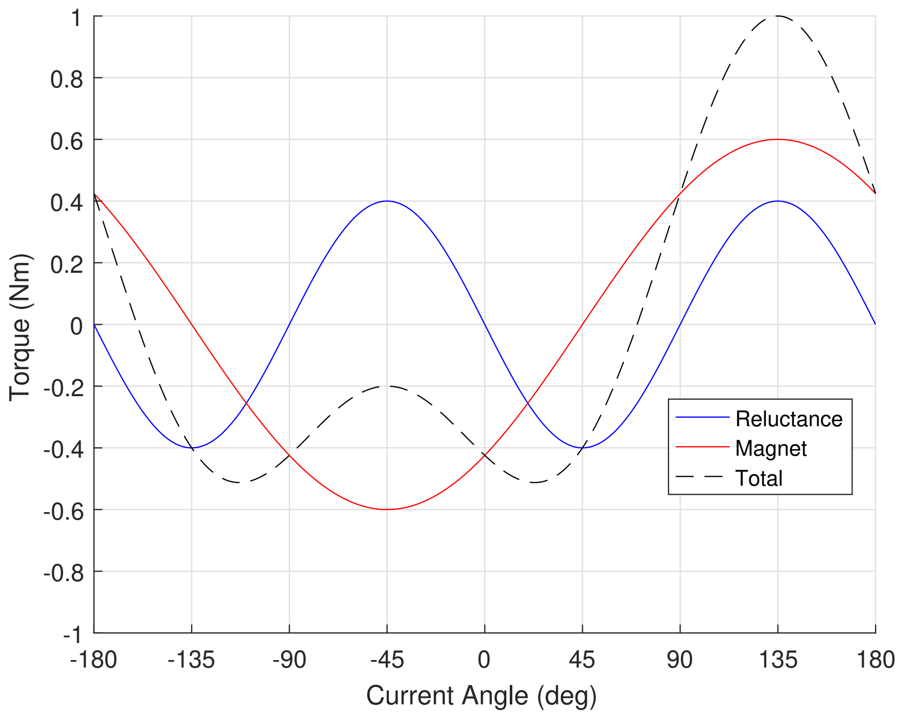

Figure 2.15: Theoretical Torque Versus Current Angle IPM Machine , $\delta = 45°$: Reluctance Torque (blue), Magnet Torque (red), Total (black dashed)

2.7.1 Ideal Case

In this section, the interaction of the salient and magnet features is not considered. This assumption is utilized to determine the maximum theoretical benefit of the aligned axis structure and requires ignoring the effects of magnet geometry upon the geometry of the salient rotor. Included in the ideal case, the magnet material proprieties are altered to maintain a constant magnet torque independent of magnet alignment or air gap. This second assumption allows for the ratio of magnet torque to reluctance torque to be fixed as the magnet axis alignment is varied. Under these ideal conditions, it is confirmed fig. 2.16, the optimum magnet alignment occurs at 45°. A design that is overly reluctant or dominated by the magnet yields little benefit from adjustment of the magnet alignment angle. During design, this magnet to inductance ratio must be considered. The torque benefit of magnet alignment, as compared to the traditional IPM magnet alignment, is computed as a percentage and presented in figure 2.16. The maximum torque benefit of 16% occurs when the magnet torque is 2.5 times the reluctance torque. The most benefit can be achieved when the magnet torque to reluctance torque ratio is between 1 and 5, centered around a magnet alignment angle of 45°.

2.7.2 Magnet Geometry Effects

The embedded magnet has two effects: a primary one to provide flux that creates torque and a secondary one, that alters the reluctance path. When the embedded magnet direction coincides with the axis of maximum reluctance, the saliency ratio is enhanced and more torque is realizable. As the magnet is aligned between the minimum and maximum reluctance, the span of the magnet alters the reluctance path; so much so, that the current angle

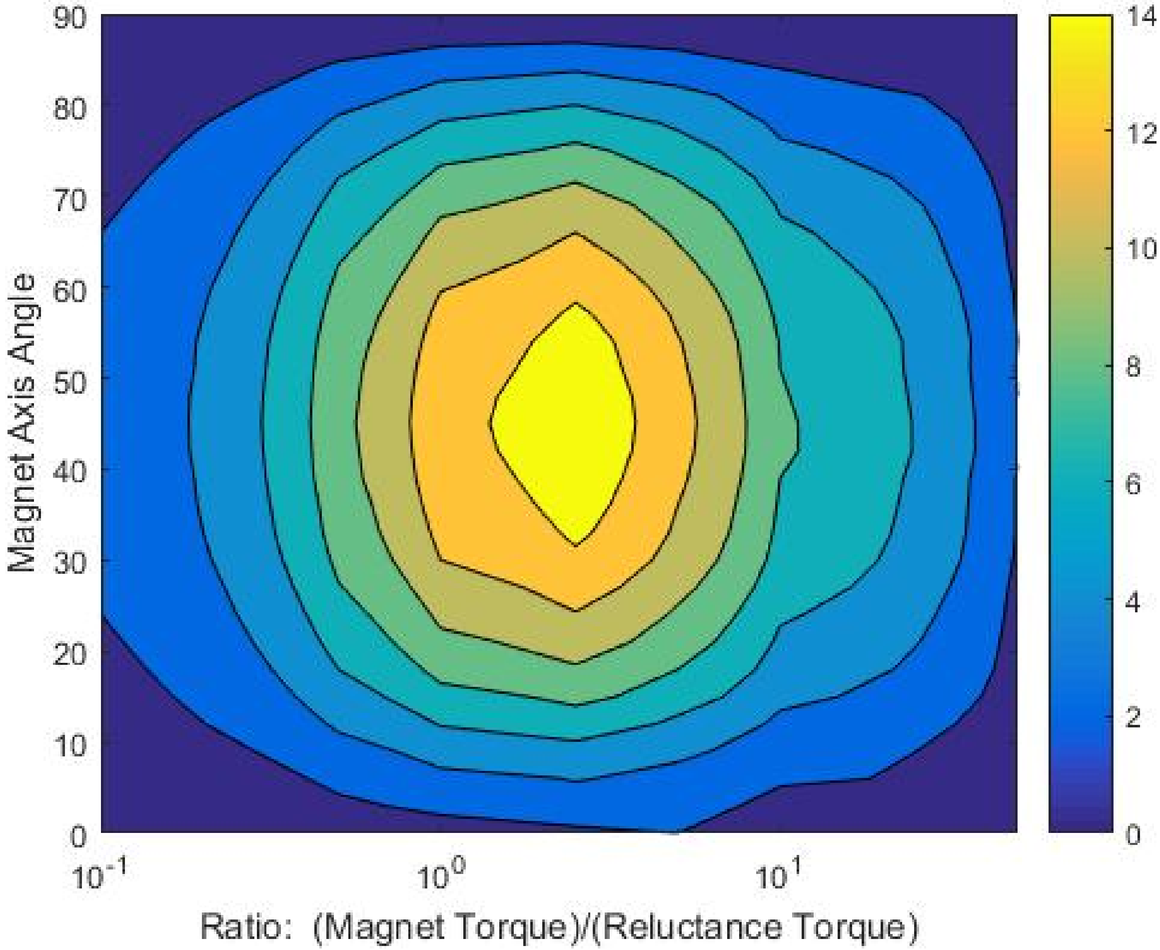

Figure 2.16: Torque Benefit of Ideal Aligned Axis Design as Compared to Traditional Alignment (% increase)

at the torque zero crossing no longer coincides with the geometrical angle of the minimum and maximum air gaps. The analytical magnet model and the modified air gap are both considered during the calculation of the magnet and reluctance air gap flux densities. The magnet span as a percentage of pole pitch is varied along with the magnet axis current angle. A constant armature current was imposed. Figure 2.17 shows that when the geometry of the embedded magnet is included in the reluctance torque computation, optimum results do not occur if the span is too wide. The ideal case torque is presented alongside the torque with different magnet spans. When the magnet spans the full pole pitch the maximum torque is not realizable; as the magnet span shrinks, the ideal location is approached. As the magnet alignment angle is varied, the geometrical and physical axes, of the magnet and reluctance are no longer coincident. The shift, or difference between geometrical and physical axes, is also presented in figure 2.17 by comparing the magnet torque and reluctance torque zero crossing shifts. The impact of this is minimal using practical alignment angles between $0°$ and $45°$. Clearly, magnet geometry must be considered when designing the adjustment features for the location of the magnet flux.

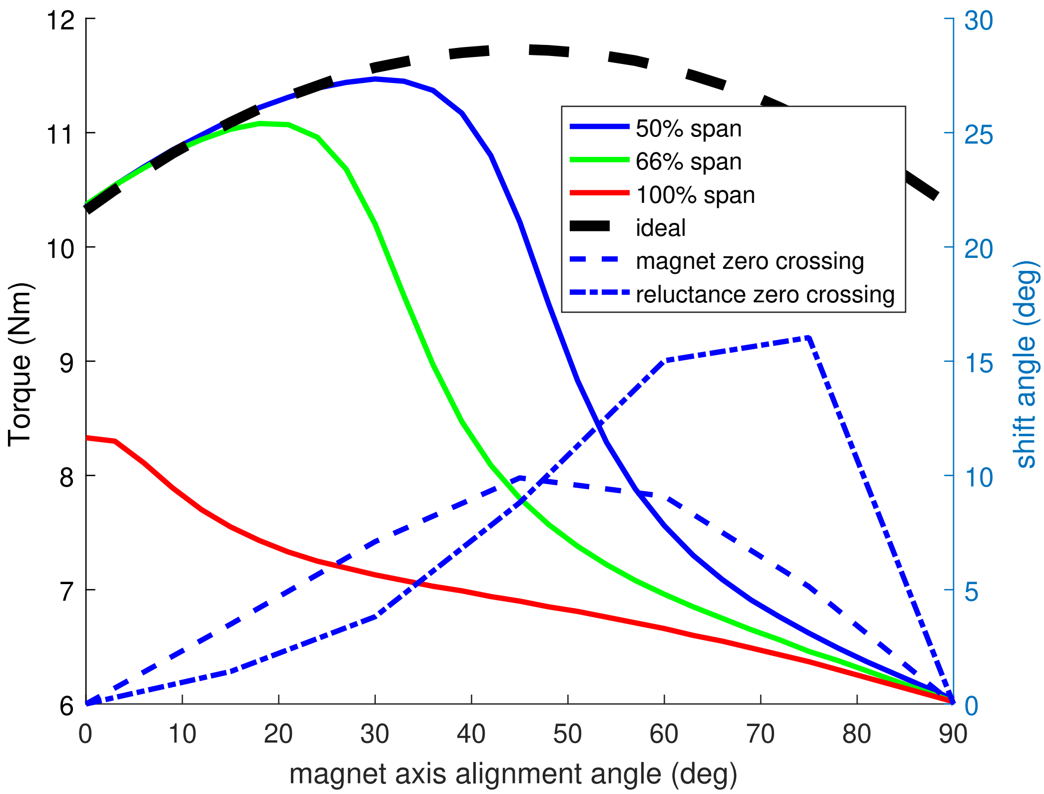

Figure 2.17: Torque Benefit as Function of Alignment Angle and Magnet Width as Percentage of Pole Span: ideal case torque (black dashed), 100% magnet span torque (red), 66% magnet span torque (green), 50% magnet span torque (blue) , 50% magnet span torque (blue), magnet physical vs actual shift angle (blue dashed) , magnet physical vs actual shift angle (blue dashed dotted)

Chapter 3

Fundamentals: Implementation and Control

3.1 Voltage Equations

The synchronous PMAC machine is comprised of a permeable stator, a 3 phase winding within the stator, and a permeable rotor with both salient and magnet features. Figure 3.1 is a simple model useful in the development of the governing voltage and torque equations. The 3 phase windings can each be represented within the stationary frame as separate vectors A, B, and C. The three phase vectors, fixed in direction, but not in amplitude can be vector summed and represented in $-\alpha\beta$ coordinates. The α coordinate is aligned with the phase A vector and points to the right. The β coordinate is orthogonal to the α and pointed upward.

$$[T_s] = \frac{2}{3}\begin{bmatrix} 1 & -\frac{1}{2} & -\frac{1}{2} \\ 0 & \frac{\sqrt{3}}{2} & -\frac{\sqrt{3}}{2} \end{bmatrix} \tag{3.1}$$

$$[T_s]_{inv} = \begin{bmatrix} 1 & 0 \\ -\frac{1}{2} & \frac{\sqrt{3}}{2} \\ -\frac{1}{2} & -\frac{\sqrt{3}}{2} \end{bmatrix} \tag{3.2}$$

Transformation of ABC quantities to the $\alpha\beta$ coordinate system can be done through the coordinate transformation $[T_s]$. $[T_s]$ and $[T_s]_{inv}$ transform the coordinates from the 3 phase vectors to a stationary reference frame $\alpha\beta$ and back again. These are presented as amplitude invariant transformations. This transformation is often referred to as the 3 to 2 transformation and in its generic form shown below.

$$\begin{bmatrix} x_\alpha \\ x_\beta \end{bmatrix} = \frac{2}{3} \begin{bmatrix} 1 & -\frac{1}{2} & -\frac{1}{2} \\ 0 & \frac{\sqrt{3}}{2} & -\frac{\sqrt{3}}{2} \end{bmatrix} \begin{bmatrix} x_a \\ x_b \\ x_c \end{bmatrix} \tag{3.3}$$

$$\begin{bmatrix} x_a \\ x_b \\ x_c \end{bmatrix} = \begin{bmatrix} 1 & 0 \\ -\frac{1}{2} & \frac{\sqrt{3}}{2} \\ -\frac{1}{2} & -\frac{\sqrt{3}}{2} \end{bmatrix} \begin{bmatrix} x_\alpha \\ x_\beta \end{bmatrix} \tag{3.4}$$

Another useful variable transformation is to look at the variables as seen by the rotating

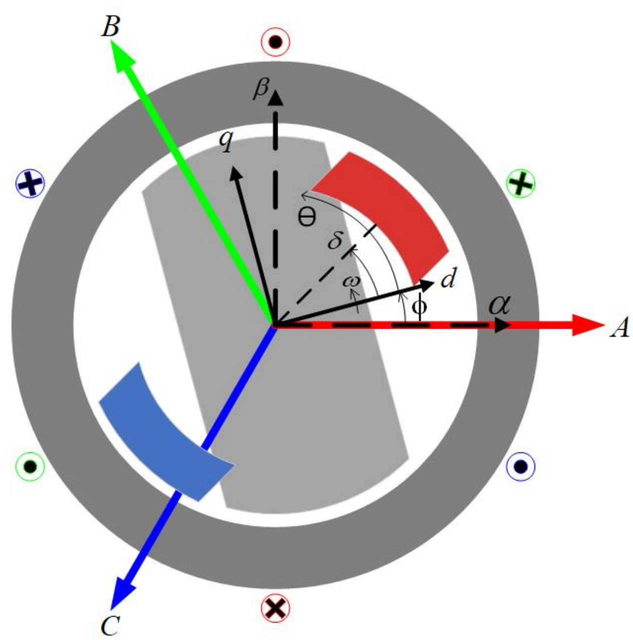

Figure 3.1: Motor Structure with Voltage Eq

from $-dq$. The matrix $T_r(\phi)$ and $T_r(\phi)^{-1}$ transform the stationary frame values to the rotating frame of reference as it rotates at angular velocity ω.

$$[T_r(\phi)] = \begin{bmatrix} \cos\phi & \sin\phi \\ -\sin\phi & \cos\phi \end{bmatrix} \tag{3.5}$$

$$[T_r(\phi)]^{-1} = \begin{bmatrix} \cos\phi & -\sin\phi \\ \sin\phi & \cos\phi \end{bmatrix} \tag{3.6}$$

These allow the $\alpha\beta$ vector to be written as dq coordinates.

$$\begin{bmatrix} x_d \\ x_q \end{bmatrix} = \begin{bmatrix} \cos\phi & \sin\phi \\ -\sin\phi & \cos\phi \end{bmatrix} \begin{bmatrix} x_\alpha \\ x_\beta \end{bmatrix} \tag{3.7}$$

$$\begin{bmatrix} x_\alpha \\ x_\beta \end{bmatrix} = \begin{bmatrix} \cos\phi & -\sin\phi \\ \sin\phi & \cos\phi \end{bmatrix} \begin{bmatrix} x_d \\ x_q \end{bmatrix} \tag{3.8}$$

The traditional rotor frame of reference $-dq$ has the $-d$ axis aligned with maximum reluctance and the $-q$ axis is aligned with the minimum reluctance. Traditional placement of the d axis would also align with the magnet. In this case, the magnet is aligned off of the -d axis by angle δ. The rotor rotates at speed ω and a rotor position of ϕ.

3.1.1 Voltage Equations in ABC

The voltage equations consist of a voltage drop due to the resistive elements and the time rate of change of the flux linkages. Where the voltage for each phase is written as v_x, the current is i_x, flux linkage λ_x, and phase resistance R_s.

$$\begin{bmatrix} v_a \\ v_b \\ v_c \end{bmatrix} = R_s \begin{bmatrix} i_a \\ i_b \\ i_c \end{bmatrix} + \frac{d}{dt} \begin{bmatrix} \lambda_a \\ \lambda_b \\ \lambda_c \end{bmatrix} \tag{3.9}$$

Flux linkage of each phase is made up of the flux densities from both permanent magnet and the inductive sources. Self inductance is written as L_{xx} and mutual inductance is written as M_{xy}. Where as the permanent magnet flux linkage due to the magnet for each phase is λ_{mx}

$$\begin{bmatrix} \lambda_a \\ \lambda_b \\ \lambda_c \end{bmatrix} = L_{ls} \begin{bmatrix} i_a \\ i_b \\ i_c \end{bmatrix} + \begin{bmatrix} L_{aa} & M_{ab} & M_{ac} \\ M_{ba} & L_{bb} & M_{bc} \\ M_{ca} & M_{cb} & L_{cc} \end{bmatrix} \begin{bmatrix} i_a \\ i_b \\ i_c \end{bmatrix} + \begin{bmatrix} \lambda_{ma} \\ \lambda_{mb} \\ \lambda_{mc} \end{bmatrix} \tag{3.10}$$

Angular position of rotor ϕ is . As the rotor changes angular position, ϕ ,the inductance of the phases change with 2ϕ and the flux linkage of the magnets change with ϕ.

$$\begin{bmatrix} \lambda_{ma} \\ \lambda_{mb} \\ \lambda_{mc} \end{bmatrix} = \begin{bmatrix} \lambda_m \cos(\phi - \delta) \\ \lambda_m \cos(\phi - \frac{2\pi}{3} - \delta) \\ \lambda_m \cos(\phi + \frac{2\pi}{3} - \delta) \end{bmatrix} \tag{3.11}$$

The self and mutual inductance contain a leakage term L_{ls}, the average terms L_A, and the position dependant term L_B.

$$
\begin{aligned}
L_{aa} &= L_{ls} + L_A - L_B \cos[2(\phi)] \\
L_{bb} &= L_{ls} + L_A - L_B \cos[2(\phi - \frac{2\pi}{3})] \\
L_{cc} &= L_{ls} + L_A - L_B \cos[2(\phi + \frac{2\pi}{3})]
\end{aligned}
\tag{3.12}
$$

$$
\begin{aligned}
M_{ab} = M_{ba} &= -\frac{1}{2}L_A - L_B \cos[2(\phi - \frac{\pi}{3})] \\
M_{ac} = M_{ca} &= -\frac{1}{2}L_A - L_B \cos[2(\phi + \frac{\pi}{3})] \\
M_{bc} = M_{cb} &= -\frac{1}{2}L_A - L_B \cos[2(\phi + \pi)]
\end{aligned}
\tag{3.13}
$$

$$L_A = \frac{L_d + L_q}{2} \tag{3.14}$$

$$L_B = \frac{L_q - L_d}{2} \tag{3.15}$$

3.1.2 The Clarke Transformation: Voltage Equations in $\alpha\beta$

The voltage equations expressed in three phase quantities can are written in eq. (3.9). In vector form these equations are written in eq. (3.16).

$$\vec{v}_{abc} = R_s \vec{i}_{abc} + \frac{d}{dt}\vec{\lambda}_{abc} \tag{3.16}$$

Applying $[T_a]$ to the phase voltage equations, $\vec{v}_{abc}$, transforms the voltage equations to $\alpha\beta$ coordinates.

$$\vec{v}_{\alpha\beta} = R_s \vec{i}_{\alpha\beta} + \frac{d}{dt}[T_a][L_{sabc}][T_a^{-1}]\vec{i}_{\alpha\beta} + \frac{d}{dt}\vec{\lambda}_{m\alpha\beta} \tag{3.17}$$

With some work, the stationary frame flux linkages are simplified to contain doubly sinusoidal and cosinusoial terns in Eq. 3.18.

$$\begin{bmatrix} \lambda_\alpha \\ \lambda_\beta \end{bmatrix} = \begin{bmatrix} L_{ls} + \frac{3}{2}L_A - \frac{3}{2}L_B\cos(2\phi) & -\frac{3}{2}L_B\sin(2\phi) \\ -\frac{3}{2}L_B\sin(2\phi) & L_{ls} + \frac{3}{2}L_A + \frac{3}{2}L_B\cos(2\phi) \end{bmatrix} \begin{bmatrix} i_\alpha \\ i_\beta \end{bmatrix} + \lambda_m \begin{bmatrix} \cos(\phi - \delta) \\ \sin(\phi - \delta) \end{bmatrix} \tag{3.18}$$

The stationary frame voltage equation is simplified to the form shown in Eq. 3.19.

$$\vec{v}_{\alpha\beta} = R_s\vec{i}_{\alpha\beta} + \frac{d}{dt}\vec{\lambda}_{\alpha\beta} \tag{3.19}$$

3.1.3 The Park Transformation: Voltage Equations in DQ Coordinates

Transformation of variables from the stationary frame to the rotating is shown complex vector form with eq. (3.20). Likewise, the Clarke transformation complex vector form is shown in eq. (3.21). The complex rotation and its conjugate are shown in eq. (3.22) and eq. (3.23).

$$\vec{x}_{\alpha\beta} = \vec{x}_{dq}e^{j\phi} \tag{3.20}$$

$$\vec{x}_{dq} = \vec{x}_{\alpha\beta}e^{-j\phi} \tag{3.21}$$

$$e^{-j\phi} = \cos(\phi) - j\sin(\phi) \tag{3.22}$$

$$e^{j\phi} = \cos(\phi) + j\sin(\phi) \tag{3.23}$$

First the Park transformation is applied to Eq. 3.19.

$$\vec{v}_{dq}e^{j\phi} = R_s\vec{i}_{dq}e^{j\phi} + \frac{d}{dt}\left(\vec{\lambda}_{dq}e^{j\phi}\right) \tag{3.24}$$

The derivative term is expanded in Eq. 3.25.

$$\frac{d}{dt}\left(\vec{\lambda}_{dq}e^{j\phi}\right) = \frac{d}{dt}\left(\vec{\lambda}_{dq}\right)e^{j\phi} + j\frac{d\phi}{dt}\vec{\lambda}_{dq}e^{j\phi} \tag{3.25}$$

Finally the dq voltage equations are expressed as the following.

$$v_d = R_s i_d + l_d\frac{d}{dt}i_d - \omega l_q i_q - \omega\lambda_m \sin(\delta) \tag{3.26}$$

$$v_q = R_s i_q + l_q\frac{d}{dt}i_q + \omega l_d i_d + \omega\lambda_m \cos(\delta) \tag{3.27}$$

3.2 Torque Equation

In this section, the torque equation is developed for the IPM machine. An energy balance of the electro mechanical system is utilized to develop the equation. Using the single coil armature salient rotor shown in fig. 3.2 as the starting point.

$$v = Ri + \frac{d\lambda}{dt} \tag{3.28}$$

Multiplying the single coil voltage equation by idt results in an expression for incremental work, where the incremental joule losses are Ri^2dt, the infinitesimal electrical work is $vidt$,

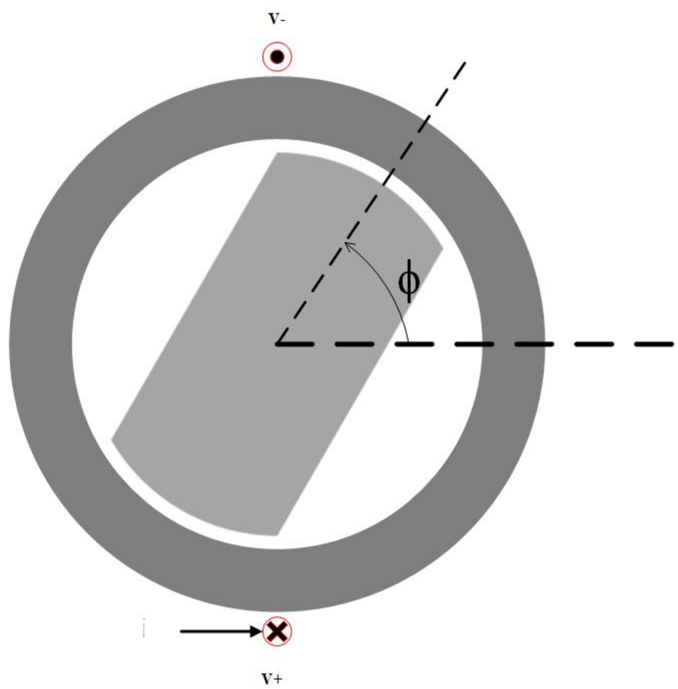

Figure 3.2: Single Coil Reluctance System

and $id\lambda$ is sum of incremental energy stored combined with increment work from torque.

$$vidt = Ri^2 dt + id\lambda \tag{3.29}$$

This assumption is valid when other losses, such as magnetic hysteresis, are not considered. Considering eq. (3.29) the incremental work of the electro-mechanical system contains the electrical energy supplied, $vidt$, the lost joule energy, Ri^2dt, and the magnetic energy, $id\lambda$. The differential magnetic energy , $id\lambda$, of the system contains the balance of stored magnetic energy and the mechanical output of the system.

$$id\lambda = dw_m + \tau d\phi \tag{3.30}$$

The full differential form of stored energy dw_m is shown in eq. (3.31).

$$dw_m = \frac{\partial w_m(\lambda, \phi)}{\partial \lambda} d\lambda + \frac{\partial w_m(\lambda, \phi)}{\partial \phi} d\phi \tag{3.31}$$

Combining eq. (3.30) and eq. (3.31) the energy balance becomes eq. (3.32).

$$id\lambda - \tau d\phi = \frac{\partial w_m(\lambda, \phi)}{\partial \lambda} d\lambda + \frac{\partial w_m(\lambda, \phi)}{\partial \phi} d\phi \tag{3.32}$$

Upon careful inspection of eq. (3.32) the torque can be expressed in terms of stored magnetic energy.

$$id\lambda = \frac{\partial w_m(\lambda, \phi)}{\partial \lambda} d\lambda \tag{3.33}$$

$$-\tau d\phi = \frac{\partial w_m(\lambda, \phi)}{\partial \phi} d\phi \tag{3.34}$$

$$\tau(\lambda, \phi) = -\frac{\partial w_m(\lambda, \phi)}{\partial \phi} \tag{3.35}$$

Due to saturation, it is useful to consider the co-energy w_m' of the system. Co-energy is remaining balance from the product of current and flux linkage and the stored magnetic energy.

$$w_m'(i, \phi) = i\lambda - w_m(\lambda, \phi) \tag{3.36}$$

Through similar analyis the torque can be expressed in terms of co-energy.

$$dw_m'(i, \phi) = \lambda di + \tau d\phi \tag{3.37}$$

Extending the concepts of stored magnetic energy, the torque equations for the machine shown in fig. 3.1 is developed. Flux linkage and its energy are expressed in terms of both inductive and permanent magnet sources.

$$dw'_m(i,\phi) = di\lambda + id\lambda - dw_m(\lambda,\phi) \tag{3.38}$$

$$dw'_m(i,\phi) = \lambda di + \tau d\phi \tag{3.39}$$

$$\lambda di + \tau d\phi = \frac{\partial w'_m(i,\phi)}{\partial i} di + \frac{\partial w'_m(i,\phi)}{\partial \phi} d\phi \tag{3.40}$$

$$\tau = \frac{\partial w'_m(i,\phi)}{\partial \phi} \tag{3.41}$$

$$\vec{\lambda} = [L]\vec{i} + \vec{\lambda_m} \tag{3.42}$$

$$w_m(i_a, i_b, i_c, \lambda_m, \phi) = \frac{1}{2}\Big[\lambda_a i_a + \lambda_b i_b + \lambda_c i_c\Big] = \frac{1}{2}\vec{\lambda}^T\vec{i} \tag{3.43}$$

$$w_m = \frac{1}{2}\Big[\vec{i}^t[L]\vec{i} + \vec{\lambda_m}^t\vec{i}\Big] \tag{3.44}$$

Separating the inductive and permanent magnet terms the IPM torque equation can now be expressed as eq. (3.45).

$$\tau = \frac{\partial(\frac{1}{2}\vec{\lambda}^T\vec{i})}{\partial \phi} = \frac{1}{2}\frac{\partial(\vec{i}^t[L]\vec{i})}{\partial \phi} + \frac{1}{2}\frac{\partial(\vec{\lambda_m}^t\vec{i})}{\partial \phi} \tag{3.45}$$

With much work, the torque equation for the interior permanent magnet machine considering a magnet to reluctance angle of δ is shown in eq. (3.46).

$$\tau = \frac{1}{2}\frac{3}{2}\Bigg((l_d - l_q)i_d i_q + \lambda_m\Big(\cos(\delta)i_q - \sin(\delta)i_d\Big)\Bigg) \tag{3.46}$$

3.3 First Analysis of Machine Performance and Control

The steady state torque, voltage, and power equations are shown in eq. (3.47), eq. (3.48), eq. (3.49), and eq. (3.50). These are the fundamental equations to analyze and control of electric machines. Resistance and loss terms do not have an effect on the torque and only affect the voltage and electrical power. In some analysis it may be useful to assume the phase resistance is negligible.

$$\tau = \frac{1}{2}\frac{3}{2}\Bigg((l_d - l_q)i_d i_q + \lambda_m\Big(\cos(\delta)i_q - \sin(\delta)i_d\Big)\Bigg) \tag{3.47}$$

$$v_d = R_s i_d + -\omega l_q i_q - \omega\lambda_m \sin(\delta) \tag{3.48}$$

$$v_q = R_s i_q + \omega l_d i_d + \omega\lambda_m \cos(\delta) \tag{3.49}$$

$$P = \tau\omega = \frac{3}{2}\frac{1}{2}\Big(v_d i_d + v_q i_q\Big) \tag{3.50}$$

To determine the performance of the electric machine both the current limit, I_{max}, and the voltage limits V_{max} must be considered. The current limit is limited by the power devices of the inverter or the electric machine's thermal capability and is represented by the equation eq. (3.51). The voltage limit is the maximum phase voltage that the inverter can apply, limited by the specific pulse width modulation technique used.

$$I_{max} \leq i_d^2 + i_q^2 \tag{3.51}$$

$$V_{max} \leq v_d^2 + v_q^2 \tag{3.52}$$

Viewed on the current plane, where i_d is the horizontal and i_q is the vertical axis, the current limit equation is a circle of radius I_{max} with its center at the orgin. Plotting voltage limit on the same current plane requires further analysis through the combination of the lossless steady state voltage equations and the voltage constraint into eq. (3.53). In this form the voltage equation becomes an ellipse on the current plane where I_{fq} and I_{fd} locate the center of the voltage ellipse and the denominators define the minor and major axis dimensions.

$$\frac{i_q + I_{fq}}{\frac{V_{max}^2}{(-\omega l_q)^2}} + \frac{i_d + I_{fd}}{\frac{V_{max}^2}{(-\omega l_d)^2}} \leq 1 \tag{3.53}$$

$$\lambda_m \cos(\delta) = l_q I_{fq} \tag{3.54}$$

$$\lambda_m \sin(\delta) = l_d I_{fd} \tag{3.55}$$

The maximum operable speed at specific current levels can be determined by eq. (3.56).

$$\omega = \sqrt{\frac{V_{max}^2}{(l_q i_q + \lambda_m \sin(\delta))^2 + (l_d i_d \lambda_m \cos(\delta))^2}} \tag{3.56}$$

The operation of the electric machine is bounded by the current circle and the voltage ellipse but not fully defined by both. At startup the machine runs inside of the current circle and voltage ellipse. The current to operate within these bounds is described as maximum torque per amp (MTPA). To realize the MTPA trajectory, an optimization problem is needed, as shown in eq. (3.57).

$$\begin{aligned} \min_{-\tau} \quad & \tau = \frac{1}{2}\frac{3}{2}\left((l_d - l_q) i_d i_q + \lambda_m \Big(\cos(\delta) i_q - \sin(\delta) i_d\Big)\right) \\ \text{s.t.} \quad & I_{ss} = i_d^2 + i_q^2 \end{aligned} \tag{3.57}$$

The machine operates on this trajectory until the critical speed or base speed of the machine is reached. The machine begins to field weaken while operating at I_{max}. As the machine speed increases, a second critical speed is reached where the machine is both operating at I_{max} and V_{max}. Beyond this second critical speed the machine begins to operate along the maximum torque per volt (MTPV) trajectory. To realize the MTPV trajectory, an additional optimization problem is used in eq. (3.58).

$$\begin{aligned} \min_{-\tau} \quad & \tau = \frac{1}{2}\frac{3}{2}\Bigg((l_d - l_q) i_d i_q + \lambda_m \Big(\cos(\delta) i_q - \sin(\delta) i_d \Big) \Bigg) \\ \text{s.t.} \quad & V_{max} = v_d^2 + v_q^2 \end{aligned} \tag{3.58}$$

3.3.1 Example Machine

An example machine is explored to illustrate the principles of control and the effects of the magnet displacement angle δ. Parameters of the machine studied are listed in table 3.1. Analysis of two variants of the machine at $\delta = 0°$ and $\delta = 45°$ is shown in fig. 3.3 and fig. 3.4.

Machine Parameters	**Value**
d-axis inductance l_d	9 mH
q-axis inductance l_q	22.5 mH
magnet flux linkage λ_m	0.3 Vs
maximum phase voltage V_{max}	100 V
maximum phase current I_{max}	100 A

Table 3.1: Example Machine

Both figures illustrate the current circle, the voltage ellipse, the MTPA trajectory, critical speed for MTPA, the critical speed for MTPV, and the MTPV trajectory. The current trajectory of the MTPA is notably different. When the magnet angle $\delta = 0°$ the current angle of the trajectory is not constant and varies with current magnitude. When the magnet angle $\delta = 45°$ the current angle of the trajectory is constant. Additionally the center of the voltage ellipse is different for both cases. The traditional magnet angle of $\delta = 0°$ is located on the d-axis current and the $\delta = 45°$ alignment has shifted the center of the voltage ellipse into the third quadrant. The torque and power curves for the two machines are shown in fig. 3.5 and fig. 3.6. By shifting the magnet to $\delta = 45°$ both the torque and the peak power are improved.

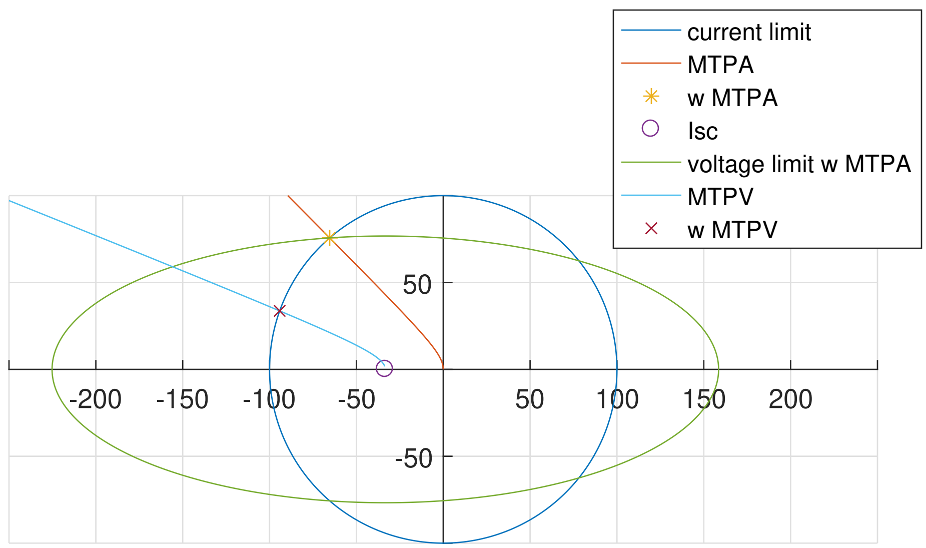

Figure 3.3: Example Machine Current Plane $\delta = 0°$, current limit (blue circle), voltage limit (green ellipse), maximum torque per ampere (MTPA) trajectory (orange curve), maximum speed of MTPA (orange *), maximum speed at full current (purple x), short circuit current (purple circle).

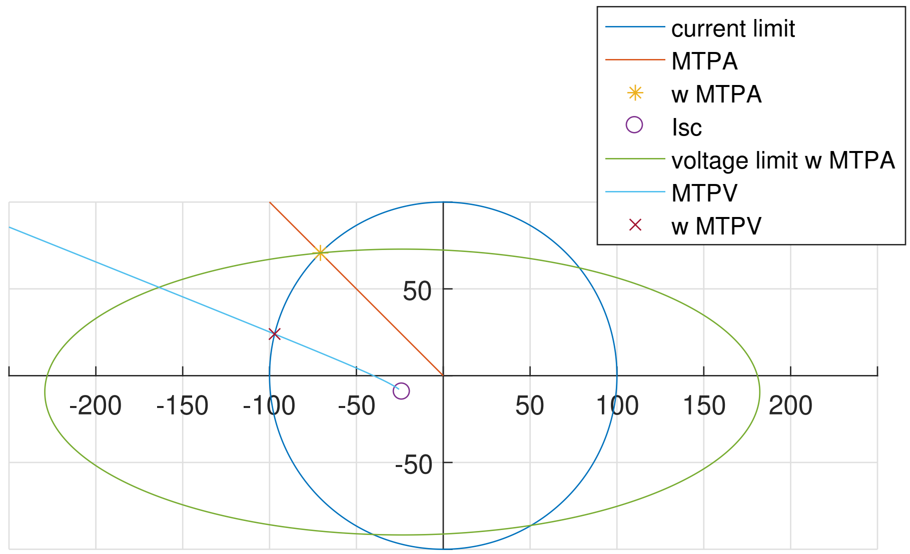

Figure 3.4: Example Machine Current Plane $\delta = 45°$,current limit (blue circle), voltage limit (green ellipse), maximum torque per ampere (MTPA) trajectory (orange curve), maximum speed of MTPA (orange *), maximum speed at full current (purple x), short circuit current (purple circle).

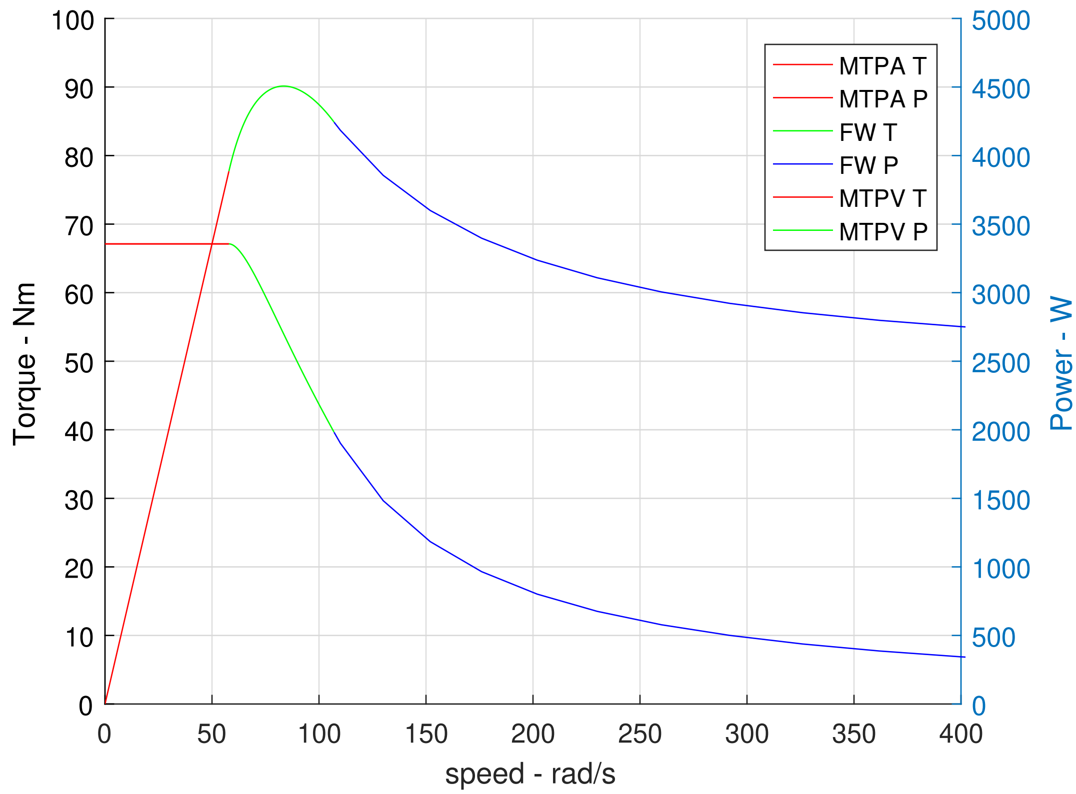

Figure 3.5: Example Machine Torque and Power Speed Curves $\delta = 0^{\circ}$

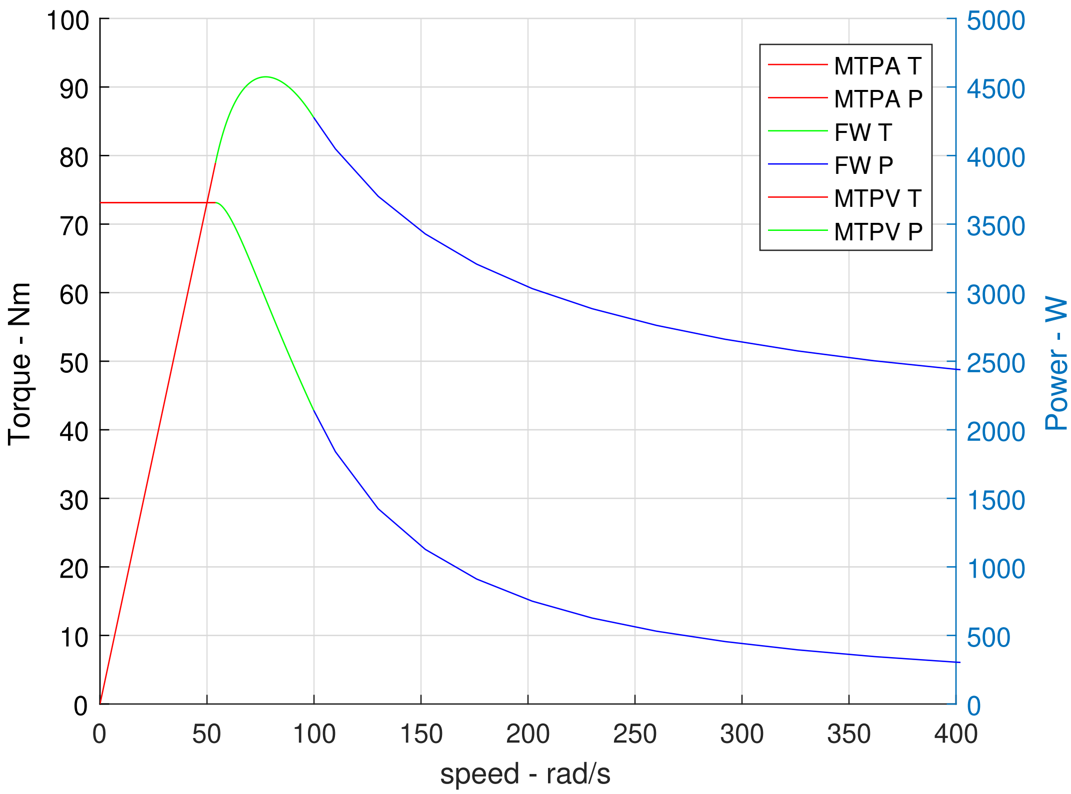

Figure 3.6: Example Machine Torque and Power Speed Curves $\delta = 45°$

3.4 Relationship to Design

The computation of torque is not enough for machine design. It is necessary to stay within the constraints of current and voltage. As the design evolves, these properties must be considered to meet torque, power, efficiency, torque ripple, and other requirements. To achieve these needs flux linkage and inductive properties of the electrical machine must be determined and related to performance and control. Asymmetrical rotor sculpt features require consideration of non-conventional alignment of the magnet to the reluctance, $\delta \neq 0$, new voltage and torque equations are needed. As a result new methods for control of torque as needed for the magnet alignment of $\delta \neq 0$.

Chapter 4

MMF Permeance Theory

Modeling air gap permeability and its reaction MMF provides an analytical model that can be solved quickly and provides insight into the design which is discussed in [59, 60, 84–86]. This method is used to compute the radial flux density of the machine B_r through modeling the airgap permeance, Λ_r, and the MMF, F_r, and a constant reflecting the pole to pole symmetry in eq. (4.1).

$$B_r(\theta, \phi) = 2\Lambda_r(\theta, \phi)F_r(\theta, \phi) \tag{4.1}$$

Accurate descriptions of stator and rotor permeance are required, along with the MMF of the stator windings and the rotor magnets. These models have been traditionally applied to embedded surface mount permanent magnet machines approximating the behavior of the interior permanent magnet machine. This chapter will establish the necessary MMF permeance framework to model IPM machines with rotor sculpt features.

4.1 Air Gap Permeance

Magnetic circuits are analogous to electrical circuits; they replace voltage with MMF and resistance with reluctance. Permeance, $\mathcal{P}$ is a property of allowing the passage of magnetic flux and is the inverse of reluctance, $\mathcal{R}$. Both are related to the permeability μ, cross sectional area A and the length of the air gap, g. The MMF, F, is defined by the stator current and winding arrangement.

$$\mathcal{P} = \frac{1}{\mathcal{R}} = \frac{\mu A}{g} \tag{4.2}$$

$$F = \Phi \mathcal{R} \tag{4.3}$$

Hence the magnetic flux, Φ,is the product of MMF and permeance.

$$\Phi = \mathcal{P} F = \frac{1}{\mathcal{R}} F \tag{4.4}$$

Considering that total magnetic flux density, $\Phi = BA$, is the product of the flux density and area, these concepts can be applied locally using eq. (4.1).

Stator and rotor geometry, individually and together, require the air gap permeability function Λ_r to be described as functions of the angular position with respect to the stationary frame, α, and the angular position of the rotor, ϕ. The air gap permeance function in its simplest form is the ratio of permeability of free space and the air gap thickness. Accommodating both stator and rotor the air gap function is described as combination of the rotor, g_{rt}, and stator, g_{so}, air gaps [60].

$$\Lambda_{tot}(\phi, \theta) = \frac{\mu_0}{g_{rt}(\phi, \theta_{rt}) + g_{so}(\phi, \theta_{so})} \tag{4.5}$$

4.2 Rotor Reluctance Path

Interior permanent magnet machines feature a rotor with embedded magnets serving to create both a magnet driven MMF and a salient structure. A single barrier IPM rotor structure, as shown in figures 1.2, 4.1, and 4.4, shows the common features, including embedded magnets, high reluctance barriers which the magnets fit within, a rib structure under the magnet, a rib structure above the magnet, and bridges to hold the two ribs together. Highly permeable steel rib structures along with the high reluctance of air barriers form the basis of the salient structure. The rib behind the magnet is aligned with the q- axis at the air gap providing two functions. Firstly it allows flux to flow in the q-axis, also referred to as the primary reluctance path. Secondly, it provides a permeable path for the backside of the permanent magnet. The rib above the magnet, provides a secondary reluctance path, allowing q axis flux to loop through and allowing the magnet flux to easily flow into the air gap of the machine.

Modeling the reluctance structure of interior permanent magnet machines has primarily been done by assuming an inset surface mount structure [59, 60, 84–86]. Dajuku and Gerling considered the primary reluctance path by calculating the two permeances, Λ_{p1} and Λ_{p2} [84, 85]. Koo and Nam considered a similar structure applying a Taylor series expansion for the reluctance path [60]. Each of these describes the primary reluctance path as it allows the magnetic flux to flow between two adjacent q-axis. Figure 4.1 shows the graphic description (green) of the permeabilities of the primary path. At the location of the q axis the permeance, Λ_{p1}, is a function related to the air gap of the electric machine.

$$\Lambda_{p1} = \frac{\mu_0}{g} \tag{4.6}$$

The permeance, Λ_{p2}, is related to the flux that flows through the -d axis to yoke of the rotor. This flow-through flux passes through both the air gap, g, and the magnet barrier, h_m.

$$\Lambda_{p2} \approx \frac{\mu_0}{g + h_m} \tag{4.7}$$

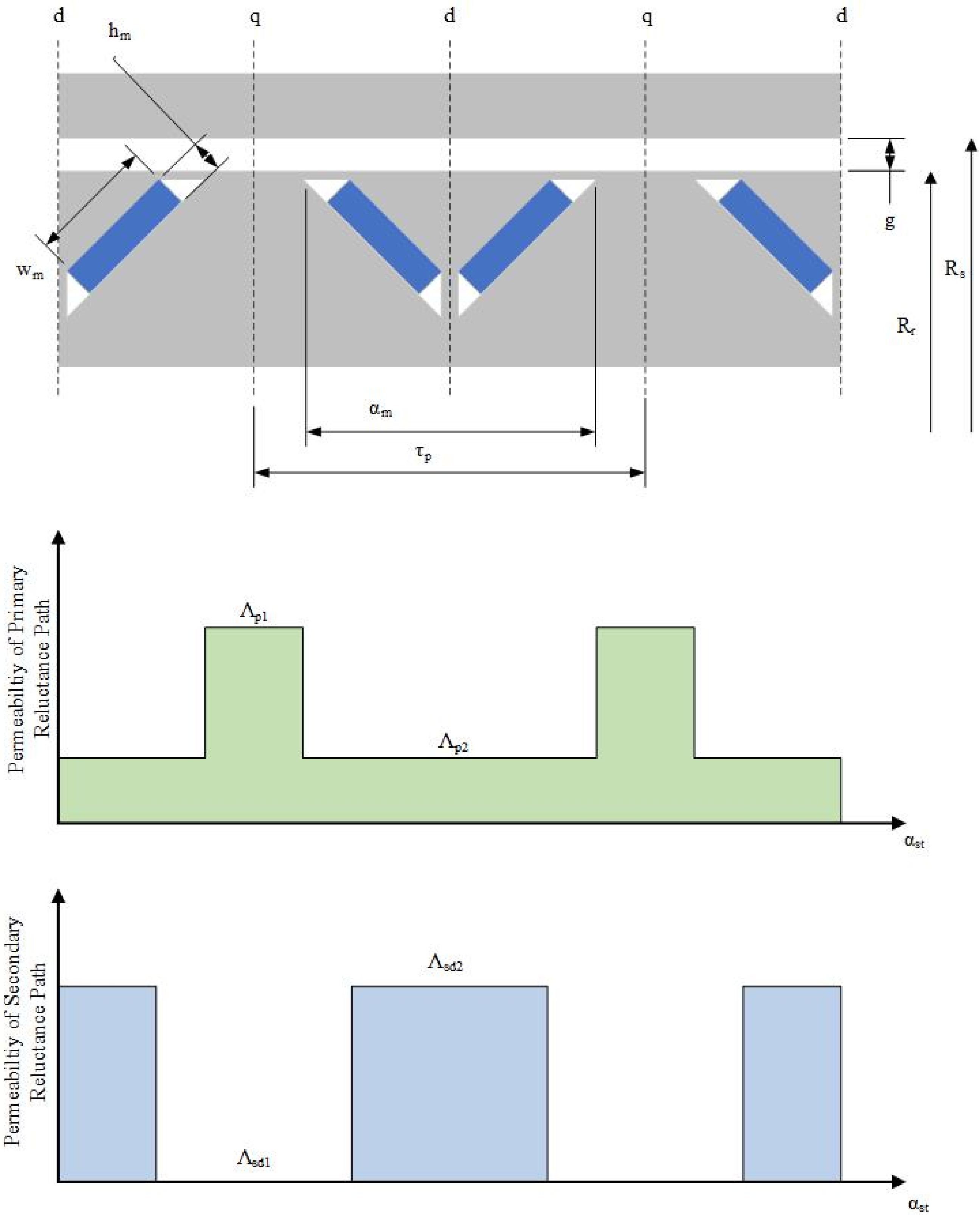

Figure 4.1: Permeability of IPM Rotor

The permeances Λ_{p1} and Λ_{p2} allow modeling the flux which passes through the air gap, into the yoke of the rotor, and returns through the air gap. It does not take into account the reluctance flux looping through the secondary reluctance path. Vagati, et al., [53] considered the structure of multiple reluctance paths for a synchronous reluctance machine but did not take into account the incorporation of magnets. For a single barrier IPM, as shown in fig. 4.4, the secondary reluctance can be modeled as the permeabilities shown in blue. The region in which the secondary path is present, Λ_{sd2} , the air gap permeance is related to only the air gap.

$$\Lambda_{sd2} = \frac{\mu_0}{g} \tag{4.8}$$

In the regions where the secondary path is not present, Λ_{sd1}, the permeability is zero.

$$\Lambda_{sd1} = 0 \tag{4.9}$$

This pattern effectively locates the secondary reluctance paths presence, but cannot be directly used with eq. (4.1) to calculate flux.

4.3 Stator Slots by Permeance Function

The air gap shown so far has been a smooth stator bore with a single barrier IPM rotor. Figure 4.2 shows the opposite, a smooth rotor bore with stator slots and the approximate function. As illustrated, magnetic flux within airgap will cross from rotor to stator, predominately in a radial fashion [60]. Magnetic flux crossing the air gap within the slots will not travel the full height of the slot as the distance to the edge of the slot is much shorter. The flux lines in red have been drawn to illustrate this. The air gap from the stators perspective is approximated with $g_s(\alpha)$, where at the tooth tip $g_s(\alpha) = 0$ and within the slot the air gap takes on a triangular nature with height h_s and width $\gamma\tau_s$. Where γ is simply the percentage of the tooth width that occupies the slot pitch $\tau_s = w_{th} + w_s$.

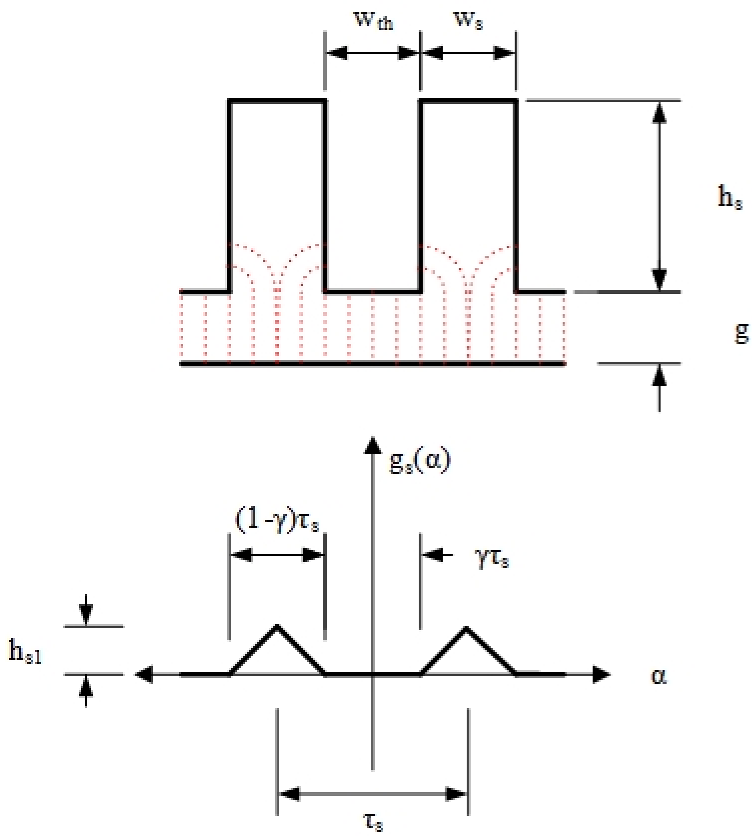

Figure 4.2: Stator slots physical and air gap model: tooth width w_{th}, slot width w_s, slot height h_s, air gap g, slot pitch τ_s, tooth percenatage of slot width γ, effective slot height h_{s1}, stator coordinate α, effective stator air gap g_s

Combining the permeances of the rotor air gap, g, and stator air gap is g_s is a series circuit operation and can be calculated with equation 4.5. As shown in section 4.2 it is easiest to express the air gap of the rotor in terms of permeability as the secondary reluctance path has permeances of zero where the material is not present. This would require modeling of an infinite air gap; therefore, it is more convenient to model the permeance directly. In contrast, the air gap of the stator, g_s, has infinite permeance where the stator teeth exist; therefore, it is best to represent the stator permeance directly with airgap. The permeance of the rotor air gap is shown below, while the air gap of the stator is shown in figure 4.2.

$$\Lambda_{rt}(\phi, \theta) = \frac{\mu_0}{g_{rt}(\phi, \theta_{rt})} \tag{4.10}$$

Combining the the rotor air gap permeance and stator air gap results in an effective total air gap which can be used to calculate total air gap permeance.

$$g_{tot}(\theta_{so}, \phi) = \Lambda_{rt}^{-1}\mu_0 + g_{so}(\theta_{so}, \phi) \tag{4.11}$$

4.4 Windings, MMF, Linear Current Density

Rotating electrical machines typically consist of a non-moving stator and a moving rotor. The permanences and MMFs of the stator and rotor interact within the air gap to produce a magnetic field and flux density. The MMFs of the armature is produced by current flowing through the armature, similarly, a rotor magnet MMF can be replicated with a current and a winding. The modeling of turns and winding functions can be first described by an elementary non-salient structure shown in figure 4.3. The turns function $n(\phi, \theta)$ is the number of the turns enclosed by the path *abcda*. It is dependant upon the starting point of integration. With some work the winding function, $N(\phi, \theta)$ is defined as follows:

$$N(\phi, \theta) = n(\phi, \theta) - < n(\phi, \theta) > \tag{4.12}$$

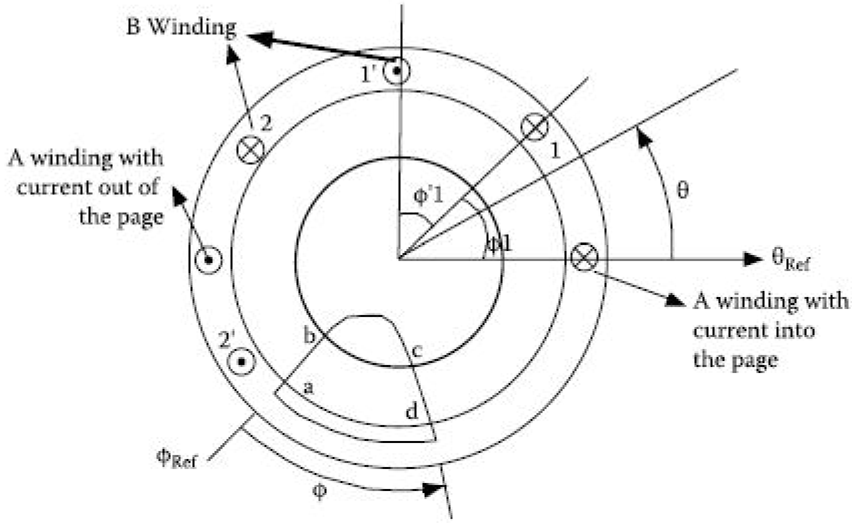

Figure 4.3: Constant air gap machine [3]

where, $< n(\phi, \theta) >$ is the average of the turns function.

$$< n(\phi, \theta) >= \frac{1}{2\pi} \int_0^{2\pi} n(\phi, \theta) d\phi \tag{4.13}$$

When the winding function, $N(\phi, \theta)$, is described with a Fourier series, the amplitude of each order is referred to as a winding factor. The MMF for any winding set is the product of its winding function and the current flowing within the winding.

$$F = N(\phi, \theta) I \tag{4.14}$$

4.4.1 Stator MMF Modifications for the Second Reluctance Path

Solving for the loop through flux condition of the second reluctance path imposes a different constraint, the sum of the magnetic flux across the region represented by Λ_{sd2} must equal zero. Modification of the MMF is required. Figure 4.4 demonstrates these MMF modifica-

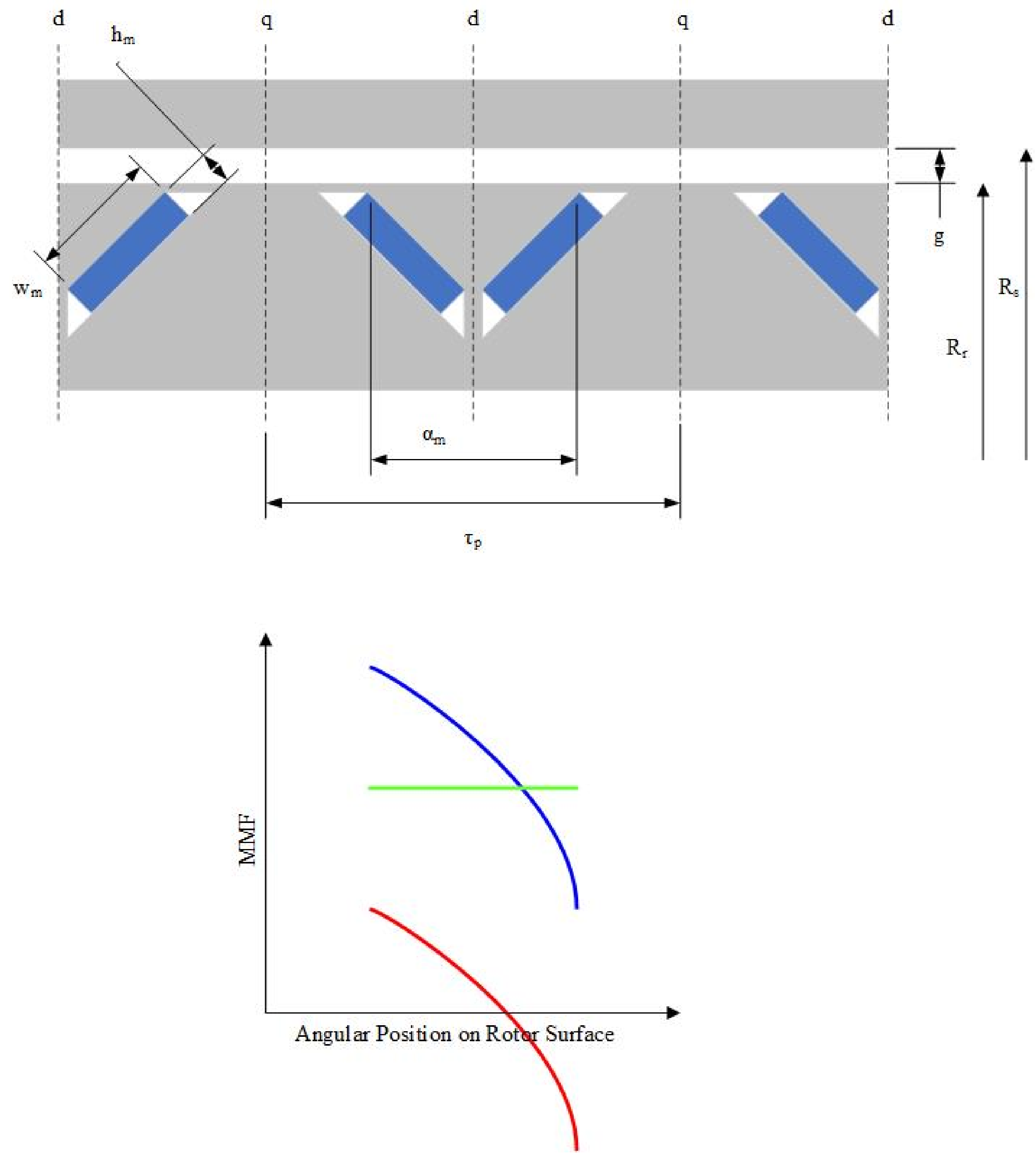

Figure 4.4: MMF modifications for secondary reluctance paths: MMF of the armature(blue), average MMF across the 2nd reluctance path (green), modified second reluctance path MMF (modified second reluctance path MMF = MMF of the armature - average MMF across the 2nd reluctance path).

tions for the second reluctance path. The blue curve represents the armature MMF of the armature over the surface bound by Λ_{sd2}. The green line is the average MMF across the second reluctance path. The red line is the difference of armature MMF and average armature MMF affecting the second reluctance path. Using the difference of the armature and average MMFs effectively holds the condition that the sum of all magnetic flux across this surface is equal to zero. This process needs to be repeated for each nonprimary reluctance path where the condition of balanced magnetic flux is required.

The rotor second reluctance path, and resulting looping flux density, is a reaction to the net change of armature MMF across the pole cap, but not the local average. This is illustrated by the second reluctance path airgap flux, shown by the blue dashed line, in fig. 1.1. Modification to the armature MMF by removing its mean satisfies local conservation of armature flux condition and is made possible through (4.15). The symbols $F_{<abc>}$ and $< F_{abc}(\theta,\phi)N_{PM}(\theta) >$ represent the modified armature MMF and its average over the span of the second reluctance path.

$$F_{<abc>}(\theta,\phi) = \Big(F_{abc}(\theta,\phi)N_{PM}(\theta,\phi) - < F_{abc}(\theta,\phi)N_{PM}(\theta,\phi) > \Big)N_{PM}(\theta,\phi) \quad (4.15)$$

$$< F_{abc}(\theta,\phi)N_{PM}(\theta,\phi) >= \frac{\frac{1}{2\pi}\int_0^{2\pi} F_{abc}(\theta,\phi)N_{PM}(\theta,\phi)d\theta}{\frac{1}{2\pi}\int_0^{2\pi} \mid N_{PM}(\theta,\phi) \mid d\theta} \quad (4.16)$$

4.5 Sculpted and Slotted Features by MMF Function

Notched or slotted features are a necessity of most electrical machines. These allow for magnetic flux to flow through the iron teeth of the stator and current to flow the copper windings within the slots. Features may be placed in the stator as a design feature to reduce torque ripple. Similar features on the surface of the rotor, referred to as sculpt features, are also used to reduce unwanted torque ripple. In its present state, MMF-permeance theory does not adequately describe these features, as it has been developed with a constant air gap dimension [3]. This section will present an extension of MMF-permeance theory describing both slots and sculpts based upon equivalent magnetic currents (EMC) [81] and the equivalent dipole [4].

4.5.1 Application of Superposition for Slotted Features

Utilization of the magnetic dipole - surface current equivalence requires superposition. Bouroujeni et al. [81] applied EMC within the subdomain solution method and focused on the solution of the cogging torque of a surface mount permanent magnet machine. As a first analysis, the fields were found for a first machine with a non-slotted stator 4.5 (b) simply filling the slots with iron and maintaining the air gap dimension. A second stator, shown in 4.5 (c), is constructed with a large airgap at a dimension equal to the slot depth and original air gap. Lateral currents are positioned coincident with the slotted edges of the original machine. The lateral currents are dependent on the radial flux density found in the first machine (a) at the position of the slot edges. It is assumed the flux density within the slot is constant therefor the radial flux density is averaged across both sides of the slot.

$$\boldsymbol{J_{ms}} = \frac{B_r}{\mu_0}\boldsymbol{a_z} \tag{4.17}$$

Equal but opposite currents are applied along the lateral edges 4.5(d) to counter the flux within the slot and direct it to the tooth. Due to the fringing seen in the two-dimensional

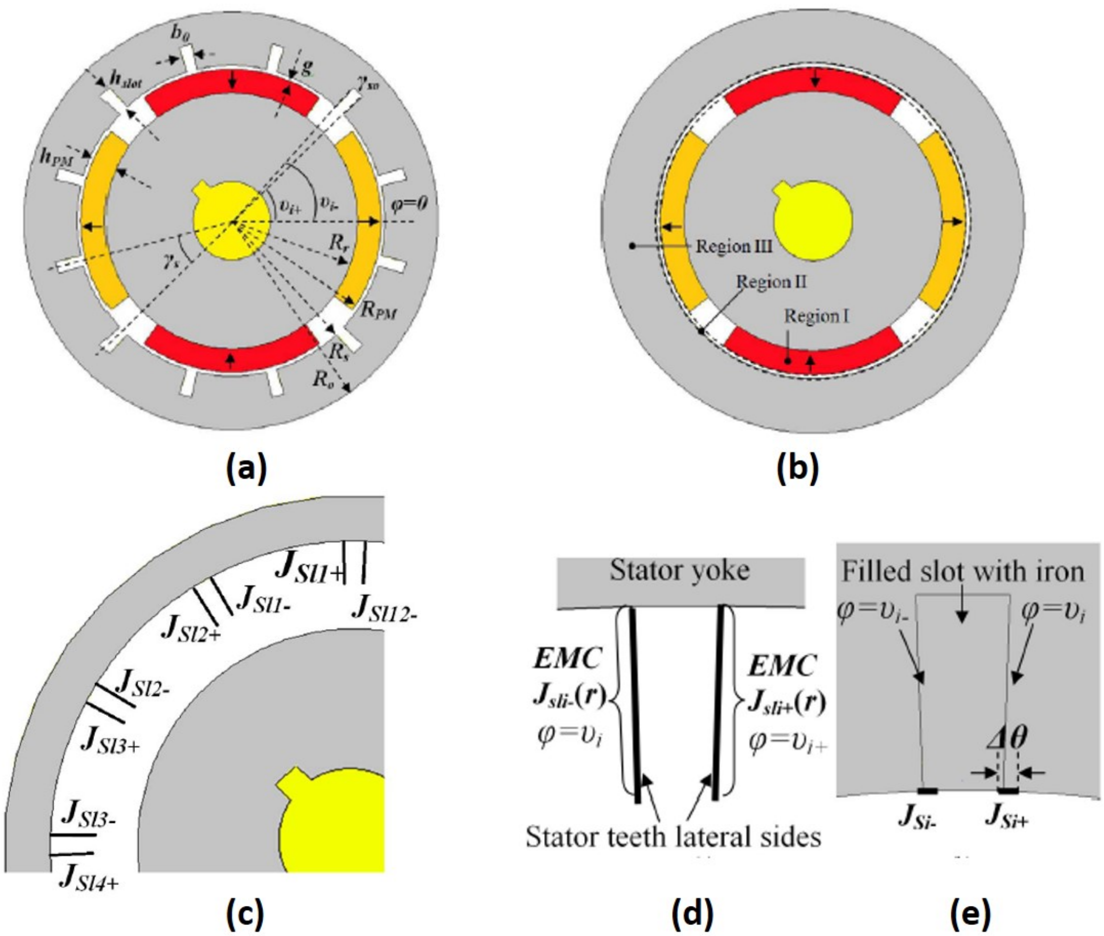

Figure 4.5: Useage of Superposition and Equivalent Magnetization Currents (a) slotted stator (b) toroidal stator (c) stator with EMC (d - e) modified EMC [4]

solution, the lateral currents (d) are converted to arc currents on the ID of the stator(e). Some iteration is required by the author to insure the fields at the center of the slot (d) are equal to the fields in (e). The solution of the arc currents with no magnets (e) and the magnet-only fields (b) are superimposed to obtain the slotted stator result. The arc currents enable the usage of Maxwell's stress tensor to determine cogging torque.

4.5.2 Magnet MMF and Sculpted Rotor

The prediction of airgap flux density for buried magnet IPM machines with sculpted rotor features requires a multi-part analysis. Equation 2.19 establishes the equivalent current for the magnet. For the case of the buried magnet, these currents cannot be directly applied in MMF permeance theory, as the span of the magnet pole is much wider than the length of the magnet. In this case, the following relationship based on conservation of flux is utilized.

$$I'_{magnet} = I_f \frac{\tau_{mag}}{\tau_{magpole}} \tag{4.18}$$

To apply this, conductors are placed at the edges of the second reluctance path surface and the ensuing turns function n, winding function N, and MMF can be formed for the embedded magnet rotor. The air gap permeance function must take into account both the thickness of the magnet and the physical air gap dimension. Figure 4.6 illustrates the conductor, turns, and winding function for the 4 pole rotor.

Superposition and MMF-Permeance theory is used, to adjust for the redistribution of flux density due to the added feature of the sculpted rotor. The sclupted rotor concept is shown in figure 4.7 (a). The unsculpted rotor, figure 4.7 (b), analyzed above with the flux density measured along the lateral features of the sculpted EMCs is calculated. The EMC

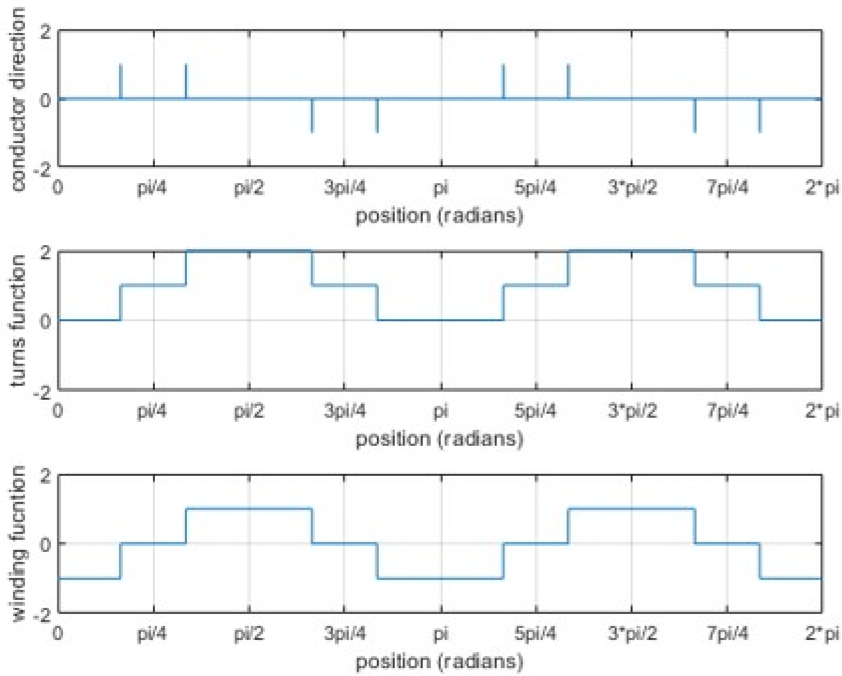

Figure 4.6: Magnet Pole Equivalent Winding Factor

is applied to figure 4.7 (c), and in this case, the winding functions for each magnet pole are considered separately. Figure 4.8 illustrates the EMC current conductor direction and

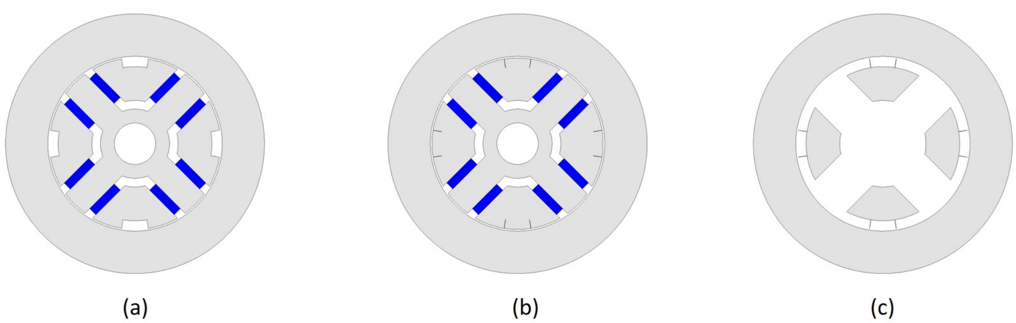

Figure 4.7: Scupted Rotor Superposition (a) sculpted rotor (b) unsculpted rotor (c) sculpted rotor equivalent magnetic currents

the resulting winding function taken over the pole. Figure 4.9 demonstrates the usage of superposition and the effect the sculpt feature has on redistribution of flux density. First, in the process, a smooth magnet pole rotor is solved for the flux density (a south pole is shown).

Next, the air gap flux density along the lateral edges of the sculpt feature is measured and used to determine the equivalent magnetic currents. The effective winding factor across the pole is computed and applied, determining the flux density countering flux within the sculpt feature and increasing flux outside of the sculpt feature.

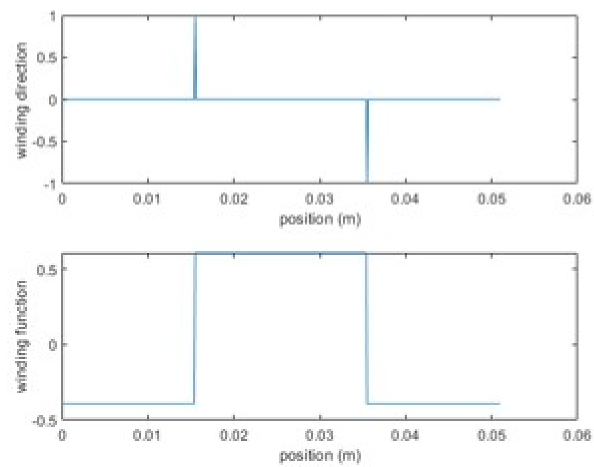

Figure 4.8: Sculpted Rotor Winding Function

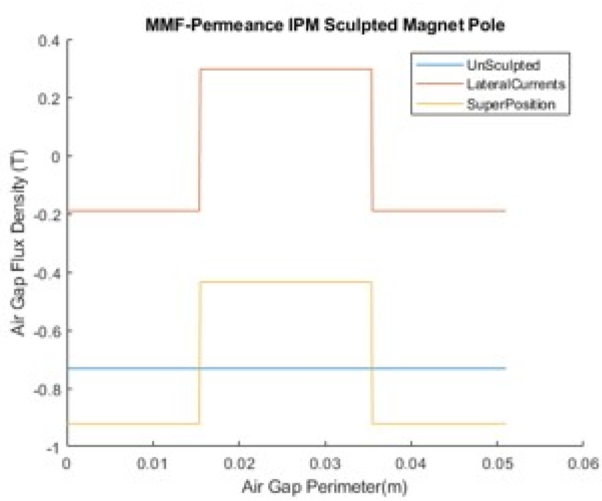

Figure 4.9: Sculpted Rotor Magnet Pole Flux Density

4.5.3 MMF of the Second Reluctance Path due to Rotor Sculpting

Rotor sculpting reluctance flux distribution. The redistribution of flux density and MMF is possible with the use of the equivalent dipole concept. Due to the changing reluctance flux density over the sculpt feature, the process of redistribution requires breaking the geometry into smaller discrete dipoles, allowing for the assumption of homogeneous flux density to hold.

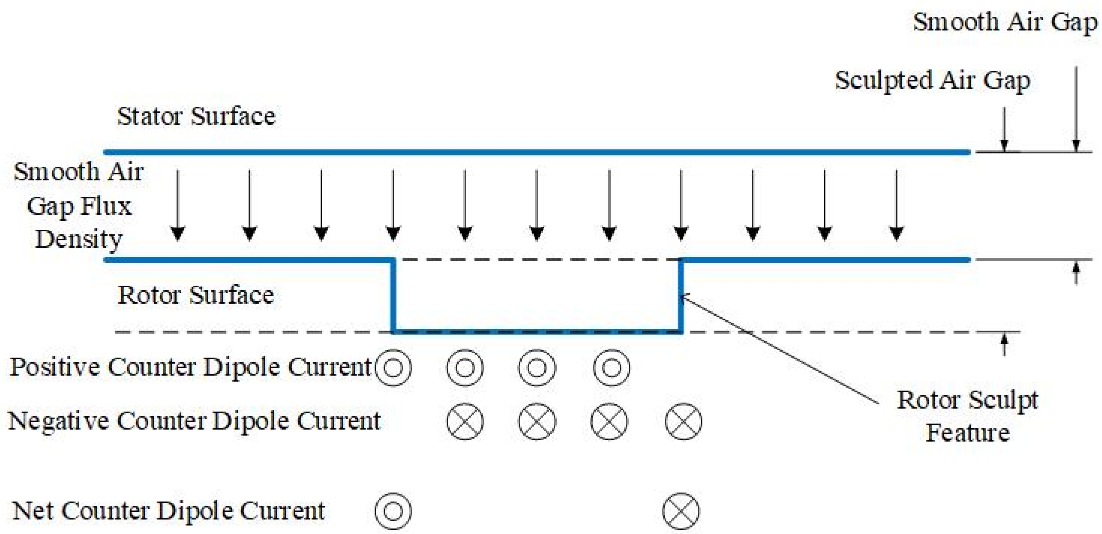

Figure 4.10: Sculpted Rotor Reluctance Counter Dipole Current

Figure 4.10 illustrates the process of analyzing the effects sculpt feature to the reluctance path. They can be broken down into the following steps, across the airgap of the second reluctance feature:

1. Define the dipole counter-current with a sufficient number of points in the sculpt feature to achieve reasonable accuracy. Utilization of the turns function from the magnet sculpt feature can simplify the determination of sculpting locations, assuming a constant sculpt depth.

2. determine the opposite second dipole counter current,

3. sum both the dipole counter current and the opposite dipole counter current, effectively creating the current-turns function for the sculpted feature,

4. create the MMF function over the pole path by removing the mean from the current-turns function,

5. calculate the air gap flux density impacts due to the sculpt feature using the increased air gap of equivalent dipole current,

6. determine the total air gap flux density by superimposing the sculpted feature air gap flux density upon the smooth rotor air gap flux density.

This process enables MMF to be redistributed by the sculpt feature and allows for the separation of sculpt and smooth rotor flux densities.

4.6 Flux Linkage and Inductance

Flux linkage is a key parameter of the machine. Flux is the area integral of flux density but does not alone determine the flux linking the coil.

$$\Phi = rl \int_{a}^{b} B(\phi, \theta) d\theta \tag{4.19}$$

Flux linkage includes how much flux density links the winding. Its calculation requires the use of the winding function. The winding function contains key information, such as: where the coils are, what direction they are wound, and the number of turns. Integrating the product of flux density and the winding function over the area provides the flux linkage, λ, for each phase x.

$$\lambda_x = rl \int_0^{2\pi} B(\phi,\theta) N_x(\phi,\theta) d\theta \tag{4.20}$$

The inductance of each phase is simply the ratio of flux linkage to the current applied.

$$L_x = \frac{\lambda_x(\phi,\theta)}{I_x(\phi,\theta)} \tag{4.21}$$

Knowledge of the flux linkage and rotational speed provides the necessary information to determine the phase voltage.

$$V_x = \frac{d\lambda}{d\phi}\frac{d\phi}{dt} \tag{4.22}$$

4.7 Example Machine

The MMF Permeance model of an example electrical machine is presented in this section. The example machine is shown in fig. 4.11 with the parameters in table 4.1. A four pole, three phase, single flux barrier, 24 slot, interior permanent magnet machine is modeled. The machine is for development purposes and not tied to any specific performance requirement. The iron components of the stator and rotor are colored gray and are assumed to have infinite permeability. The permanent magnets are embedded in the rotor are colored blue and have typical proprieties associated with NdFeB magnets. The stator is designed to have negligibly small slots, such that the bore of the stator can be considered smooth. Windings are placed around the interior of the stator, within slots, and are colored red, green, and blue to represent the three phases. Rotation of the rotor is counter clockwise, it is shown in figure 4.11 at a position of zero mechanical degrees.

The MMF-Permeance model requires a description of the air gap permeance of the rotor,

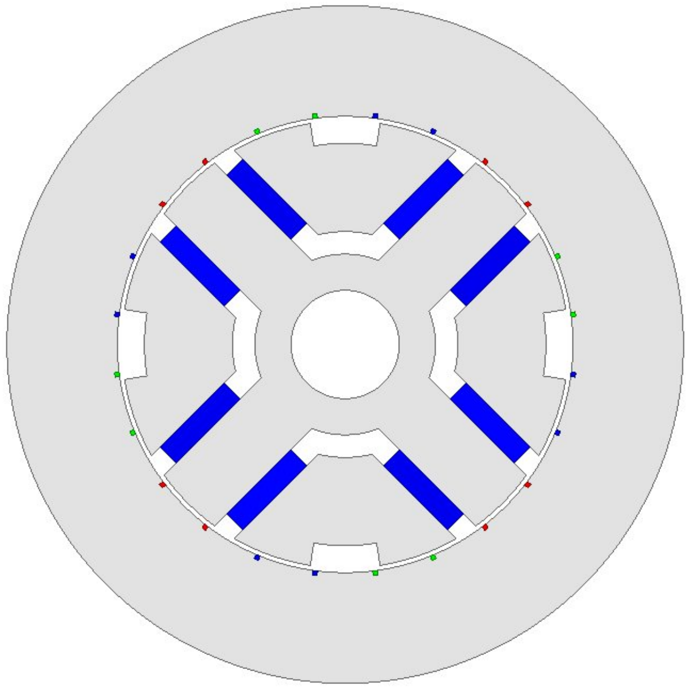

Figure 4.11: Example Motor

Parameter	**Value**	**Unit**
Number of pole pairs	2	
Rotor diameter	100	mm
Number of phases	3	
Slots per pole per phase	2	
Number of slots	24	
Magnet pole width	66	% of pole pitch
Primary reluctance path width	20	% of pole pitch
Sculpted rotor feature width	25	% of pole pitch
Number of magnets per pole	2	
Magnet thickness	5	mm
Magnet Length (per magnet)	20	mm
Relative permeability of magnet	1.099	
Rotor airgap	1	mm
Primary reluctance path second air gap	6	mm
Sculpt feature depth	5	mm

Table 4.1: Example Motor Parameters

MMF functions for each of the three phases, the equivalent MMF function of the rotor magnets, and linear current density functions represent the windings. For each magnet pole, the modification of the stator MMF must be considered to describe the second reluctance path flux density. These alone are sufficient to describe smooth rotors. They are described with a Fourier series, allowing modification for each rotor position. Equivalent magnetic dipole currents are used to describe the sculpted feature, redistributing the MMF and flux densities.

The base permeance functions of the smooth rotor inside a smooth bore stator include a description of the primary reluctance path, the second reluctance path, and the magnet path. The primary reluctance path has high permeance proportional to the inverse of airgap, aligned with the q axis of the rotor, and minimal permeance in the region of the magnet pole. The high permeance is associated with the main dimension of the rotor air gap, while the minimal permeance includes the thickness of the air gap and the magnet. In the region of the q- axis the secondary reluctance path and the magnet pole have no permeance but differ in the region of the magnet pole. The magnet path must consider both the main air gap dimension and the magnet thickness, the second reluctance path only needs to consider the air gap between the stator and rotor. For the example motor, the permeance functions are shown in fig. 4.12.

Windings are distributed among the stator slots sequenced to produce the desired MMF, linear current density, and resulting flux densities. Each turn of the winding is defined by both a position along the bore and a direction. The position of the turn is related to the available slot positions. The vector direction of the turn must either be positive (out of the page) or negative (into the page). These positive and negative directions of turns are used to create a magnetized dipole when current flows. Specially arranged these turns

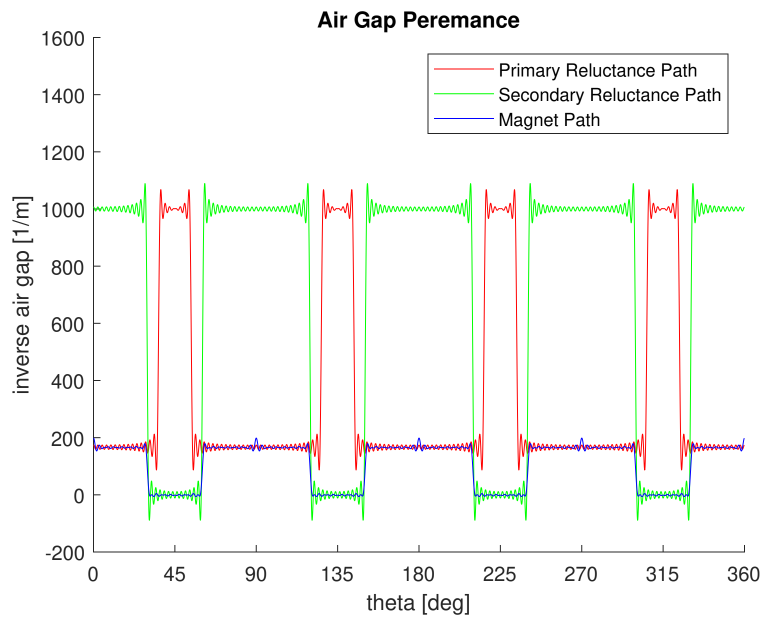

Figure 4.12: Example Motor Air Gap Permeance Functions Versus Stator Coordinate

create an MMF which approximates a sinusoidal distribution. Figure 4.13 illustrates the stator conductor direction and location, the turns function, and the winding function for the example motor. The winding function multiplied by the current for each phase produces the MMF of the armature.

In a similar fashion to the stator winding functions, a winding function can be created to replicate the MMF of the rotor magnets. Each pole has conductors with a positive direction and a negative direction, forming alternating north and south poles. The conductors are distributed at the edges of the magnet pole span. To produce the equivalent MMF of the magnets, the current is applied through the windings. Figure 4.14 shows the conductor location and direction, turns function, and the winding function of the equivalent rotor magnet winding.

Stator windings produce an MMF, which creates a radial flux density in the airgap, but also creates a tangential component of field intensity. In the analysis of torque, employing the

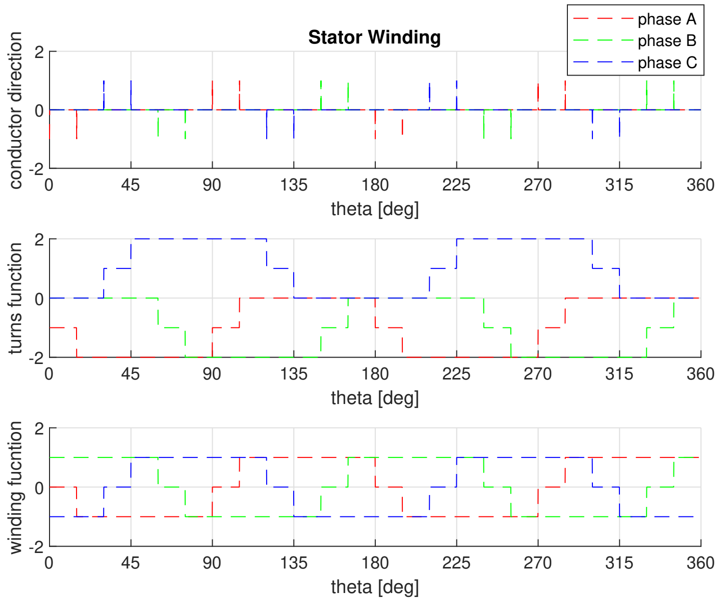

Figure 4.13: Example Motor Stator Winding Functions Versus Stator Coordinate

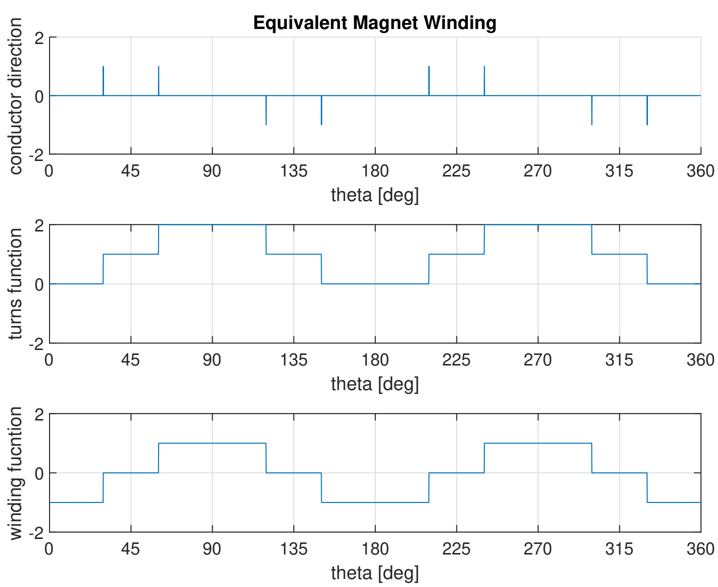

Figure 4.14: Example Rotor Equivalent Magnet Winding Functions Versus Stator Coordinate

Maxwell stress tensor, this tangential component is required. Conductor location, direction, and an assumed width are required. The current applied through the phase is used along with the assumed width to compute the linear current density. The conductor location function presented in fig. 4.13 is expanded to include the assumed width in fig. 4.15. The linear current density, or tangential field intensity, is calculated by the multiplication of the current density and the conductor width and location function.

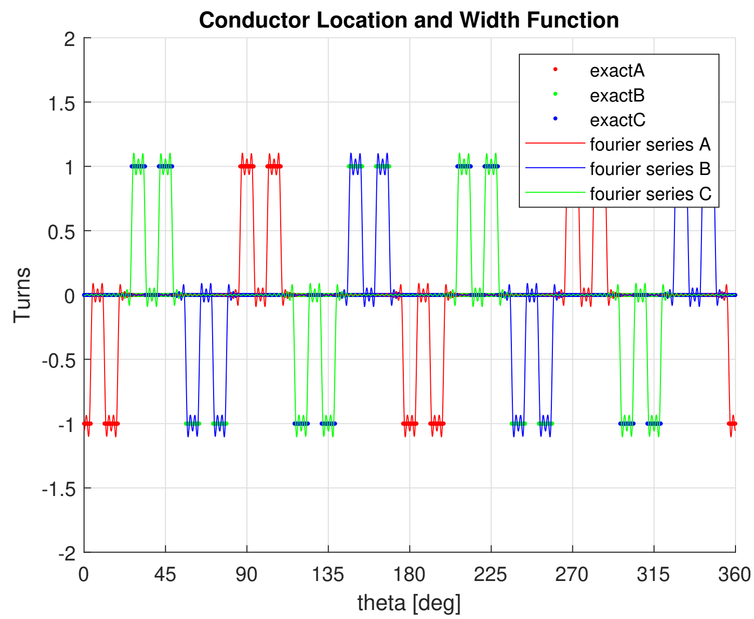

Figure 4.15: Example Stator Conductor Width Function Versus Stator Coordinate

Stator MMF is directly computed from the phase current and the winding function of the individual phases. The total MMF is the sum of each respective phase MMF. This stator MMF applies to the primary reluctance path but does not apply to the equipotential nature of the secondary reluctance path. Modification of the MMF from the stator must be made to account for this. Figure 4.16 provides an example of how this primary MMF is modified to the equipotential secondary MMF across the magnet pole region of the rotor. Radial airgap flux density can now be solved for each component of flux density using the MMF permeance equation as shown in figure 4.17.

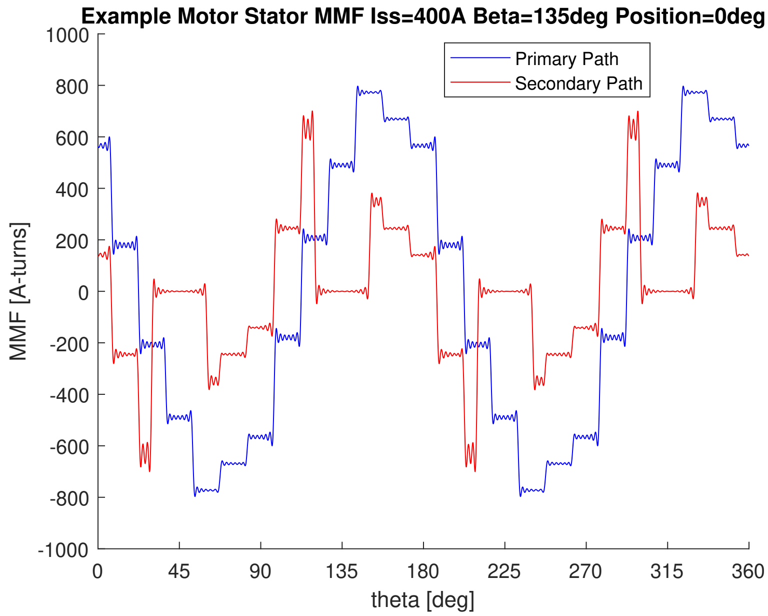

Figure 4.16: Analytically Calculated Stator MMF for Primary and Secondary Reluctance Paths Versus Stator Coordinate

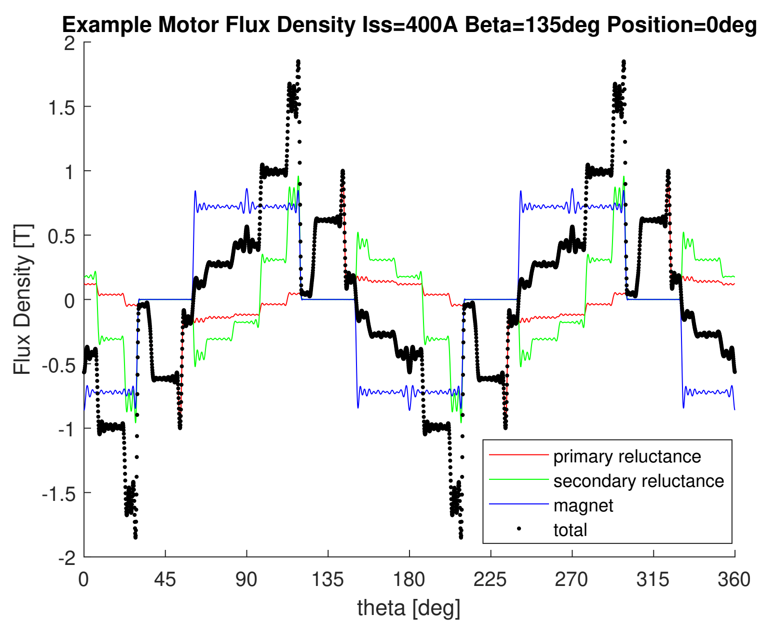

Figure 4.17: Analytically Calculated Motor Radial Flux Density Versus Stator Coordinate

Superposition of the magnetic dipole, representing the sculpted feature, requires the calculation of the smooth rotor radial air gap flux density. The radial air gap flux density of the machine without sculpting features is used the compute the current density. Combining the current density with the sculpt feature dimensions, the equivalent current is calculated. The resulting winding functions of the sculpted magnet features, figure 4.14, and MMF of the sculpted reluctance features, figure 4.19 are used for a modification of the air gap flux density.

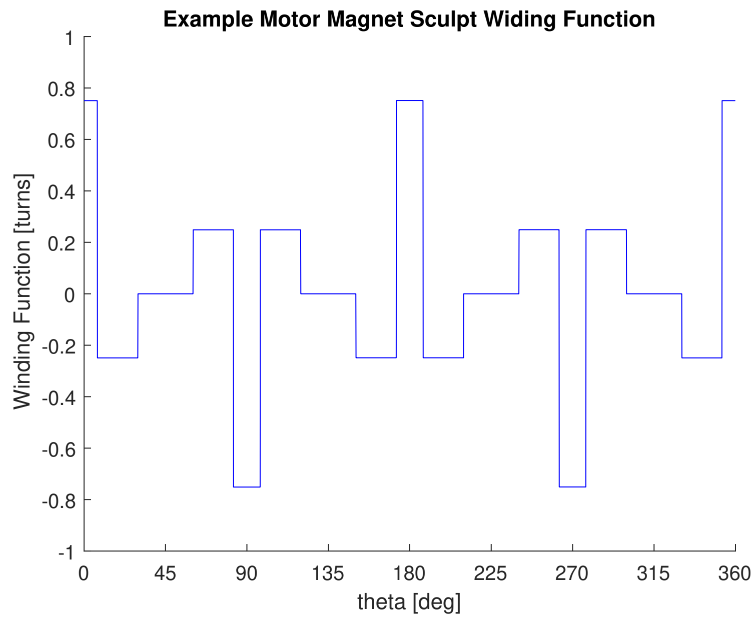

Figure 4.18: Example Motor Magnet Sculpt Feature Winding Function Versus Stator Coordinate

Finally, torque can be analyzed for each rotor position providing details of the torque ripple. Using the MMF Permeance method allows for the torque ripple components for the primary reluctance path, secondary reluctance path, magnet, and sculpt features to be analyzed separately and combined. Within this example, torques are calculated using Maxwell's stress tensor as discussed in section 2.5.

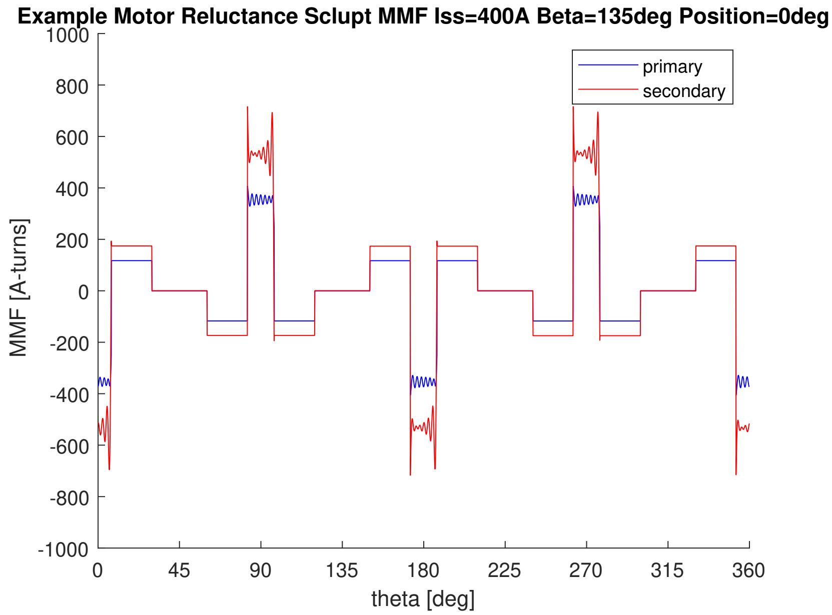

Figure 4.19: Example Motor Reluctance Sculpt Feature MMF Versus Stator Coordinate, MMF due to sculpt feature based on primary reluctance path (blue), MMF due to sculpt feature based on secondary reluctance path (red)

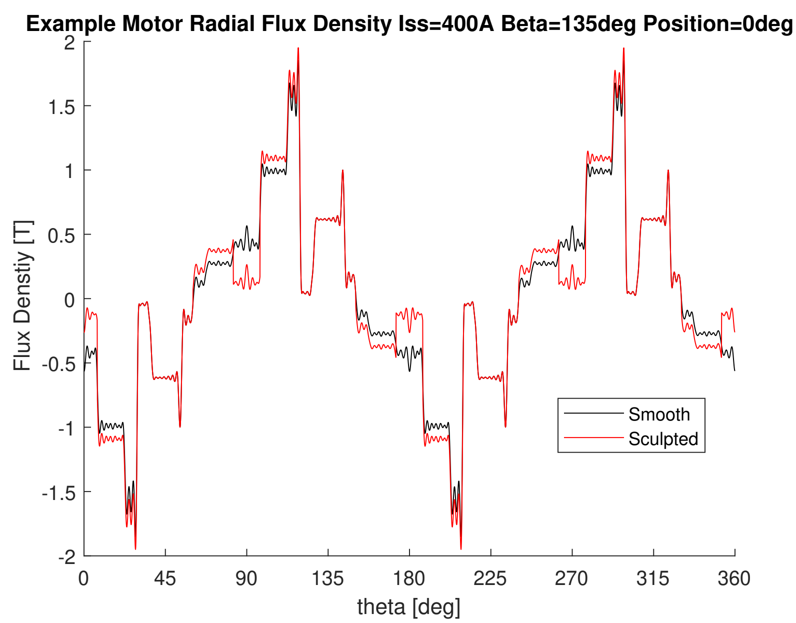

Figure 4.20: Example Motor Flux Density Sculpted vs Smooth Versus Stator Coordinate

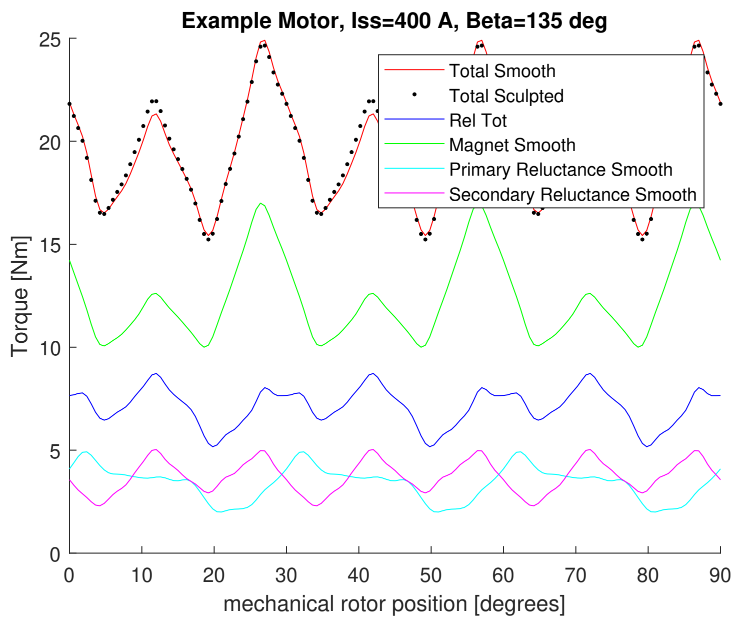

Figure 4.21: Example Motor Torque Ripple Versus Rotor Position Using MMF Permeance Model and Maxwell Stress Tensor

Chapter 5

Space and Time Harmonics of Fields, Permeance, and Torque

5.1 Fourier Series Description

Permeance, winding functions, turns densities, MMF, and linear current density may be described with the Fourier series. Airgap flux density and torque are derived from these base equations. While average torque is maintained during rotation, harmonic content also results. This section develops the Fourier series description of the three phase IPM machine, described in table 4.1. Equations are expressed in terms of electrical frequency of the machine, with the rotor spatial coordinate as θ, and rotor position of $\phi = \omega t$. Simplified Fourier series are developed in this section to illustrate harmonic contributions and interactions.

5.1.1 Current

Phase current amplitude, I_{ss}, and control angle, β, are controlled in order to develop torque. Transformed to the rotor reference frame, current are described with the direct axis current, I_d, and quadrature axis current, I_q. The phase currents, I_a, I_b, and I_c, are determined from the rotating reference frame currents and rotor position ϕ.

$$I_d = I_{ss}\cos(\beta) \tag{5.1}$$

$$I_q = I_{ss}\sin(\beta) \tag{5.2}$$

$$I_a(\phi) = I_d\cos(\phi) - I_q\sin(\phi) \tag{5.3}$$

$$I_b(\phi) = I_d\cos(\phi - \frac{2\pi}{3}) - I_q\sin(\phi - \frac{2\pi}{3}) \tag{5.4}$$

$$I_c(\phi) = I_d\cos(\phi + \frac{2\pi}{3}) - I_q\sin(\phi + \frac{2\pi}{3}) \tag{5.5}$$

5.1.2 Permeance

Permeance functions result from the geometry of the IPM rotor as shown in Fig. 5.1. Three functions are needed to describe the single-V IPM machine: the primary reluctance path,Λ_{r1}, shown as a solid red line, the second reluctance path Λ_{r2}, shown as a dashed gray line, and the permeance of the magnet path, Λ_m, shown as a solid gray line. Each function contains a constant and even order harmonics due to pole pair geometry.

$$\Lambda_{r1}(\phi,\theta) = A_{r1_\circ} + \sum_{n=2,4,6..}^{\infty} A_{r1_n}\cos(n\theta - n\phi) \tag{5.6}$$

$$\Lambda_{r2}(\phi,\theta) = A_{r2_\circ} + \sum_{n=2,4,6..}^{\infty} A_{r2_n}\sin(n\theta - n\phi) \tag{5.7}$$

$$\Lambda_{PM}(\phi,\theta) = A_{PM_\circ} + \sum_{n=2,4,6..}^{\infty} A_{PM_n}\sin(n\theta - n\phi) \tag{5.8}$$

Permeance functions for the second reluctance path, Λ_{r2}, and magnet path, Λ_{PM}, are based off the winding function, N_{PM}, and related to the their respective airgaps, g.

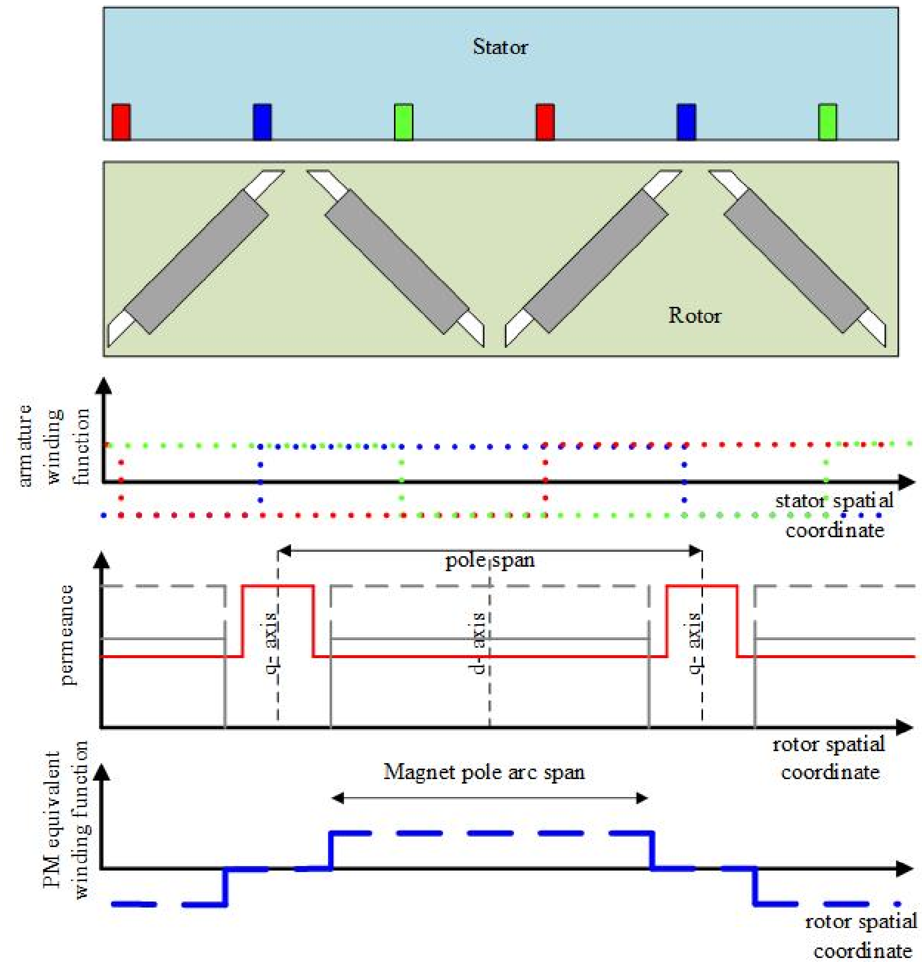

Figure 5.1: Permeance and Winding Functions

5.1.3 Winding and Turns Functions

Winding, $N_x(\theta)$, and conductor density, $C_x(\theta)$, functions are dependant upon the spatial coordinate θ, Each function contains the Fourier coefficients for amplitude and phase. Conductor density functions for each phase are C_a, C_b, and C_c represent the location and width of each conductor. The conductor density function is related to the winding function by

$C = \frac{dN}{d\theta}$. These contain odd harmonics due to the alternating polarities between poles.

$$C_a(\theta) = \sum_{n=1,3,5,7,9..}^{\infty} -a_n \sin n(\theta) \tag{5.9}$$

$$C_b(\theta) = \sum_{n=1,3,5,7,9..}^{\infty} -a_n \sin n(\theta - \frac{2\pi}{3}) \tag{5.10}$$

$$C_b(\theta) = \sum_{n=1,3,5,7,9..}^{\infty} -a_n \sin n(\theta + \frac{2\pi}{3}) \tag{5.11}$$

Where, winding functions for each phase are $N_a(\theta)$, $N_b(\theta)$, and $N_c(\theta)$ are written as follows, also contain all odd harmonics.

$$N_a(\theta) = \sum_{v=1,3,5..}^{\infty} a_v \cos v(\theta) \tag{5.12}$$

$$N_b(\theta) = \sum_{v=1,3,5..}^{\infty} a_v \cos v(\theta - \frac{2\pi}{3}) \tag{5.13}$$

$$N_c(\theta) = \sum_{v=1,3,5..}^{\infty} a_v \cos v(\theta + \frac{2\pi}{3}) \tag{5.14}$$

Finally, the equivalent magnet winding function for the rotor is $N_{PM}(\theta)$.

$$N_{PM}(\theta, \phi) = \sum_{v=1,3,5,7..}^{\infty} b_v \cos(v\theta - v\phi) \tag{5.15}$$

5.1.4 MMF and Linear Current Density

The MMF is the product of the winding function, N_x, and current, I_x. The MMF functions of the motor include phase A, F_a, phase B, F_b, phase C, F_c, rotor magnet, F_{PM}. The total

MMF of the armature (stator), F_{abc}, is the sum of all the phases.

$$F_{abc} = I_{ss}\cos(\phi_r)\sum_{v=1,3,5..}^{\infty} a_v \cos v(\theta) + I_{ss}\cos(\phi_r - \frac{2\pi}{3})\sum_{v=1,3,5..}^{\infty} a_v \cos v(\theta - \frac{2\pi}{3}) + \\ I_{ss}\cos(\phi_r - \frac{4\pi}{3})\sum_{v=1,3,5..}^{\infty} a_v \cos v(\theta - \frac{4\pi}{3}) \quad (5.16)$$

Where the permanent magnet MMF is the product of equivalent current I_{PM}, the winding magnets function, and ratio of pole span, τ_m and magnet width w_m.

$$F_{PM}(\theta, \phi) = N_{PM}(\theta, \phi) I_{PM} \frac{\tau_m}{w_m} \quad (5.17)$$

$$I_{PM} = \frac{B_r}{\mu_0 \mu_r} l_m \quad (5.18)$$

Only a subset of the armature MMF reacts with the second reluctance path permeance.

$$F_{r2}(\theta, \phi) \subseteq F_{abc}(\theta, \phi) \frac{\Lambda_{r2}(\theta)}{\max \Lambda_{r2}(\theta)} \quad (5.19)$$

Linear current density is the sum of the product of conductor densities and current for each phase.

$$K_{abc}(\theta, \phi) = C_a(\theta, \phi) I_a(p\phi) + C_b(\theta, \phi) I_b(p\phi) + C_c(\theta, \phi) I_c(p\phi) \quad (5.20)$$

5.2 Rotating Harmonics

5.2.1 Armature MMF

MMF is the product of winding functions and phase currents. A rotating MMF results from the rotor position dependant phase currents and spatially dependant winding functions. With much work and using the trigonometric identity, eq. (5.21) , the rotating system can be broken down into a positively and negatively rotating harmonics.

$$\cos A \cos B = \frac{1}{2}[\cos(A-B) + \cos(A+B)] \tag{5.21}$$

This sequence involves grouping like terms where $\phi - v\theta$ as the positively rotating sequence $\phi + v\theta$ as the negatively rotating sequence

$$F_{abc} = I_{ss} \sum_{v=1,7,13,19..}^{\infty} \frac{3}{2} a_v \cos(\phi - v\theta) + I_{ss} \sum_{v=5,11,17..}^{\infty} \frac{3}{2} a_v \cos(\phi + v\theta) \tag{5.22}$$

Even harmonics will not naturally show up, as the winding functions are derived from square waves. The resulting MMF components are centered around harmonic multiples of 6. A summary of the sequence effects is shown in the Table 5.1.

5.2.2 Primary Reluctance Path Flux Density Harmonics

The permeance function of the primary reluctance path has only a constant and even electrical harmonics. The armature MMF harmonics only contain odd orders and no triplen harmonics. The convolution of the two results in only the odd order harmonics with triplen harmonics.

	positive sequence	negative sequence
harmonic	$\phi_r - v\theta$	$\phi_r + v\theta$
1	+	
2	n/a - even	n/a - even
3	n/a - triplen	n/a - triplen
4	n/a - even	n/a - even
5		-
6	n/a - triplen	n/a - triplen
7	+	
8	n/a - even	n/a - even
9	n/a - triplen	n/a - triplen
10	n/a - even	n/a - even
11		-
12	n/a - triplen	n/a - triplen
13	+	
14	n/a - even	n/a - even
15	n/a - triplen	n/a - triplen
16	n/a - even	n/a - even
17		-
18	n/a - triplen	n/a - triplen
19	+	
20	n/a - even	n/a - even
21	n/a - triplen	n/a - triplen

Table 5.1: Armature MMF Harmonic Sequencing Summary, negative sequence (+), positive sequence (-), not applicable (n/a). Not applicable is due to cancellation of triplen harmonics of the 3 phases or even MMF components are not possible due to convolution.

$$B_{rel_1} = [A_{r1_\circ} + \sum_{n=2,4,6..}^{\infty} A_{r1_n} \cos(n\theta - n\phi)]$$
$$[I_{ss} \sum_{v=1,7,13,19..}^{\infty} \frac{3}{2} a_v \cos(\phi_r - v\theta) + I_{ss} \sum_{v=5,11,17..}^{\infty} \frac{3}{2} a_v \cos(\phi_r + v\theta)] \quad (5.23)$$

5.2.3 Linear Current Density Harmonics

The linear current density is a product of the phase current and the conductor density functions. Equation 5.20 can be simplified and re-written as equation 5.24. The electrical harmonic description is considered.

$$K_{abc} = I_{ss}\cos(\omega t)\sum_{n}^{\infty} a_n \cos(n\theta) + I_{ss}\cos(\omega t - \frac{2\pi}{3})\sum_{n}^{\infty} a_n \cos(n\theta - n\frac{2\pi}{3}) + I_{ss}\cos(\omega t - \frac{4\pi}{3})\sum_{n}^{\infty} a_n \cos(n\theta - n\frac{4\pi}{3}) \quad (5.24)$$

Each harmonic can be simplified by considering sequence effects of the phases.

$$K_{abc}(n) = I_{ss}\sum_{n}^{\infty} a_n \cos(n\theta \pm \omega t) \quad (5.25)$$

The value of the $\pm$ becomes dependant on the order of the harmonic, which is summarized in table 5.2. A pattern emerges where the fundamental rotates clockwise, triplen harmonics equate to zero, harmonics immediately before triplen harmonics rotate counter clockwise, and harmonics immediately after triplen harmonics rotate counter clockwise.

Order n	**Sign**	**Rotation Direction**
1	-	clockwise
5	+	counter clockwise
6		n/a
7	-	clockwise
11	+	counter clockwise
12		n/a
13	-	clockwise
17	+	counter clockwise
18		n/a

Table 5.2: Linear Current Density Electrical Harmonic Sequence Value

5.2.4 Torque Harmonic Orders from Air Gap Flux Density and Linear Current Density

Torque is calculated from the spatial integral of the Maxwell stress tensor. Integration filters out all but combinations that produce a constant component; periodic functions without an offset do not survive. Each combination of the radial and tangential field harmonics gives rise to two possible harmonics, resulting from both addition and subtraction of the harmonic orders. For each position, integration of the fields results in a torque. As rotor position changes like orders of B and K contribute to torque to their nearest multiple of 6, resulting in the torque of the machine changing with rotor position.

Concentrating on the convolution of the flux density with linear current density orders two possible harmonics, shown in table 5.3. Many harmonic combinations are possible due to the convolution of radial and tangential flux density orders, most do not produce torque. Only convolution of like orders results in a constant value, which is necessary to produce torque.

K\B	**1**		**3**		**5**		**7**		**9**		**11**		**13**		**15**		**17**		**19**	
1	0	2	-2	4	-4	6	-6	8	-8	10	-10	12	-12	14	-14	16	-16	18	-18	20
5	4	6	2	8	0	10	-2	12	-4	14	-6	16	-8	18	-10	20	-12	22	-14	24
7	6	8	4	10	2	12	0	14	-2	16	-4	18	-6	20	-8	22	-10	24	-12	26
11	10	12	8	14	6	16	4	18	2	20	0	22	-2	24	-4	26	-6	28	-8	30
13	12	14	10	16	8	18	6	20	4	22	2	24	0	26	-2	28	-4	30	-6	32
17	16	18	14	20	12	22	10	24	8	26	6	28	4	30	2	32	0	34	-2	36
19	18	20	16	22	14	24	12	26	10	28	8	30	6	32	4	34	2	36	0	38

Table 5.3: Air Gap Field Spatial Electrical Harmonic Convolution, Horizontal - Flux Density Harmonics, Vertical - Linear Current Density Harmonics

Maxwell stress tensor is the spatial integral of the convolution of air gap radial flux density and armature linear current density. This integration filters out all but combinations that produce a zeroth order; periodic functions without an offset do not survive. Torque harmonics which result from the convolution flux density harmonics are shown in the following table.

K\B	**1**	**5**	**7**	**11**	**13**	**17**	**19**
1	0						
5		6					
7			6				
11				12			
13					12		
17						18	
19							18

Table 5.4: Air Gap Field Spatial Electrical Harmonic Convolution and Electrical Torque Harmonic, Horizontal - Flux Density Harmonics, Vertical - Linear Current Density Harmonics

5.2.5 Magnet Flux Density and Torque Harmonics

The flux density of the rotor magnet expressed as a Fourier series is shown in equation 5.26. In this description, the rotor position, ωt, is multiplied by the order of the harmonic. The linear current density of the armature, as shown in section 5.2.3, is dependent on rotor position through the phase current.

$$B_m(\theta, \omega t) = 2\Lambda_m I_f \sum_{v=1,3,5,7..}^{\infty} b_v \cos(v\theta - v\omega t) \tag{5.26}$$

The Maxwell stress tensor combines both the magnet radial flux density and armature linear current density.

$$T_m = r^2 l 2\Lambda_m I_f I_{ss} \cdot \int_{\theta=0}^{2\pi} \left(\sum_{v}^{\infty} b_v \cos(v\theta - v\omega t) \right) \left(\sum_{n}^{\infty} a_n \cos(n\theta \pm \omega t) \right) d\theta \tag{5.27}$$

The trigonometric identity 5.21, along with the Maxwell stress tensor, is used to illustrate the 5th torque harmonic dependency on rotor position. With some work, it is shown the fundamental of the phase current interacts with both the fifth and seventh spatial harmonics of the flux density to produce sixth harmonics in torque. The sixth torque harmonic is only dependant upon rotor position, and the component which is dependant upon the spatial information is null.

$$T_m = r^2 l \Lambda_m I_f I_{ss} \cdot \int_{\theta=0}^{2\pi} \left(b_5 a_5 [\cos(-6\omega t) + \cos((10\theta - 4\omega t)] \right) d\theta \tag{5.28}$$

5.2.6 Field and Torque Harmonics Relationship to Control Angle

Consideration of control angle is necessary in the design and analysis of optimal fields, torques, and harmonics. For the average values this importance is highlighted by the torque equation 5.29, and voltage equations 5.30 and 5.31. Written with the traditional -d and -q axis, parameters and states include inductances, l_d and l_q, the permanent magnet flux linkage λ_m, armature resistance R_s, magnet alignment to reluctance axis ,δ, currents, i_d and i_q, and rotor speed ω. These governing equations, along with current, voltage, and speed constraints, determine the operating currents related to maximum torque per ampere (MTPA) and field weakening. The d- and q- axis currents influence the average performance and also contribute to the airgap flux density and torque harmonics.

$$\tau = \frac{1}{2}\frac{3}{2}\left((l_d - l_q) i_d i_q + \lambda_m \left(\cos(\delta) i_q - \sin(\delta) i_d \right) \right) \tag{5.29}$$

$$v_d = R_s i_d + -\omega l_q i_q - \omega \lambda_m \sin(\delta) \tag{5.30}$$

$$v_q = R_s i_q + \omega l_d i_d + \omega \lambda_m \cos(\delta) \tag{5.31}$$

The Fourier series description of the airgap flux density for the permanent magnet and armature induced reluctance flux densities reveals symmetries within the rotors frame of reference. The permanent magnet airgap radial flux density has even symmetry and is not dependent upon armature current, hence the spatial Fourier series expansion is based upon a cosine. The current dependant flux density, due to the interaction of armature MMF and the rotors salient structure, results in radial airgap flux densities with even symmetry (cosine) due to a d- axis current and odd symmetry (sine) with a q- axis current. The windings tangential flux density creates odd symmetry with a d- axis current and even symmetry with a q- axis current. The resulting radial and tangential flux density space harmonics, due to n current angle command, vector sum from its d- and q- axis constituents.

$$B(\theta, I_{ss}, \beta) = \Lambda(\theta)F(\theta, \vec{i_d}) + \Lambda(\theta)F(\theta, \vec{i_q}) \tag{5.32}$$

	i_d	i_q	O.C.
magnet (radial)	n/a	n/a	even
rotor reluctance (radial)	even	odd	n/a
winding (tangential)	odd	even	n/a

Table 5.5: Airgap flux density Fourier coefficients dependency on reference frame currents.

Airgap flux density symmetry extends to the discussion of torque and its harmonics. Average torque (and torque harmonics) is generated from like symmetries of radial and tangential flux densities. Opposite symmetries produce zero average torque along with harmonics. The permanent magnet flux density interaction with the -q axis currents produces average torque and harmonics. Likewise, reluctance flux densities similarly generate average torque.

$$T_{mag}(\phi, \vec{i_d}, \vec{i_q}) = r^2 l \int_{\theta=0}^{2\pi} \Big(B_{mag}(\theta, \phi)K(\theta, \phi, \vec{i_d}) + B_{mag}(\theta, \phi)K(\theta, \phi, \vec{i_q}) \Big) d\theta \tag{5.33}$$

Freezing of the reluctance airgap flux density due to reference frame current is required to obtain the interaction with its conjugate tangential flux density. Knowledge of the torque harmonics and flux density harmonics due to the -d and -q axis current, provides complete knowledge of harmonics over the entire current plane.

$$T_{rel}(\phi, \vec{i_d}, \vec{i_q}) = r^2 l \int_{\theta=0}^{2\pi} \Big(B_{rel}(\theta, \phi, \vec{i_d}) K(\theta, \phi, \vec{i_d}) + B_{rel}(\theta, \phi, \vec{i_d}) K(\theta, \phi, \vec{i_q}) + B_{rel}(\theta, \phi, \vec{i_q}) K(\theta, \phi, \vec{i_d}) + B_{rel}(\theta, \phi, \vec{i_q}) K(\theta, \phi, \vec{i_q}) \Big) d\theta \quad (5.34)$$

$$\vec{T}_{mag(n)}(\vec{i}_d + \vec{i}_q) = \vec{T}_{(n)}(\vec{i}_d) + \vec{T}_{(n)}(\vec{i}_q) \quad (5.35)$$

$$\vec{T}_{rel(n)}(\vec{i}_d + \vec{i}_q) = \vec{T}_{rel(n)}(\vec{i}_d, \vec{i}_d) + \vec{T}_{rel(n)}(\vec{i}_d, \vec{i}_q) + \vec{T}_{rel(n)}(\vec{i}_q, \vec{i}_d) + \vec{T}_{rel(n)}(\vec{i}_q, \vec{i}_q) \quad (5.36)$$

Torque and its harmonics are produced from interactions of the same harmonic of tangential and radial flux density. For the IPM machine, average torque is produced by components of fundamentals that are in phase with each other. Furthermore, torque is produced from the orthogonality of d- and q- axis winding tangential flux densities and radial flux densities. Field harmonics and non-orthogonal interactions produce the undesired torque harmonics.

5.3 Example Machine Mechanical Harmonics

Mechanical harmonics of the example machine are listed in table 4.1, without the rotor sculpt feature is presented in section 5.3. Mechanical harmonics are a product of electrical harmonics and pole pairs, with the fundamental mechanical order defined as one mechanical rotation. Since this machine is a two pole pair machine, $p = 2$, sinusoidal currents are applied with two electrical cycles per mechanical rotation. Permeance functions are doubly sinusoidal for each pole pair and, as a result, have a fourth mechanical order. Conductor density and winding functions contain both the triplen harmonics and typical 5th/7th, 11th/13th, and additional orders multiplied by the number of poles, p. Phase MMFs, conductor densities, and linear current densities retain these harmonics. The summation of all phase quantities leads to the dropping of the triplen harmonics from the total MMF and total linear current densities. Triplen harmonics are not removed from the 2nd reluctance path MMF F_{r2}. Flux densities contain both triplen and winding harmonics. Calculation of torque from Maxwell stress tensor and convolution air gap variables only even order torque harmonics remain.

Quantity	Mechanical Order
I_d	0
I_q	0
I_a	2
$I_b(p\phi)$	2
$I_c(p\phi)$	2
$\Lambda_{r1}(\theta)$	0,4,8,12,16,24,28,32,36,44...
$\Lambda_{r2}(\theta)$	0,4,8,12,16,20,24,28,32,36,40...
$\Lambda_m(\theta)$	0,4,8,16,20,28,32,36,40...
$N_a(\theta,\phi)$	2,6,10,14,18,22,26,30,34,38,42...
$N_b(\theta,\phi)$	2,6,10,14,18,22,26,30,34,38,42...
$N_c(\theta,\phi)$	2,6,10,14,18,22,26,30,34,38,42...
$N_r(\theta)$	2,6,10,14,18,22,26,30,34,38,42...
$C_a(\theta,\phi)$	2,6,10,14,18,22,26,30,34,38,42...
$C_b(\theta,\phi)$	2,6,10,14,18,22,26,30,34,38,42...
$C_c(\theta,\phi)$	2,6,10,14,18,22,26,30,34,38,42...
$F_a(\theta,\phi)$	2,6,10,14,18,22,26
$F_b(\theta,\phi)$	2,6,10,14,18,22,26
$F_c(\theta,\phi)$	2,6,10,14,18,22,26
$F_m(\theta,\phi)$	2,6,10,14,18,22,26
$F_{abc}(\theta,\phi)$	2,10,14,22,26,34,38,46,50
$F_{r2}(\theta,\phi)$	2,6,10,14,18,22,26,30,34,38,42
$K_{abc}(\theta,\phi)$	2,10,14,22,26,34,38
$B_{r1}(\theta,\phi)$	2,6,10,14,18,22,26,30
$B_{r2}(\theta,\phi)$	2,6,10,14,18,22,26,30
$B_m(\theta,\phi)$	2,6,10,14,18,22,26,30
T_{r1}	0,12,24,36,48
T_{r2}	0,12,24,36,48
T_m	0,12,24,36,48

Table 5.6: Mechanical Harmonics of Example Machine

Chapter 6

Design for Minimal Torque Ripple

6.1 Review of Design Methods and Features

The design of IPM machines is multidisciplinary and complex. Many methods have been developed to optimize and design the machine, which relies on computationally expensive processes. Each of these methods requires multiple runs to explore and optimize the result. Taguchi's design of experiment techniques was used to optimize torque production of IPM machines and minimize torque ripple in [87, 88]. Im et al., used the response surface methodology to minimize torque ripple considering both the flux barrier geometry and residual flux of the permanent magnet [89]. Response surface methodology was applied to a surface mount PMAC machine focusing on magnet pole shaping in [35]. Multi-objective and multi-load point optimization of using the response surface method to minimize torque ripple and maximize average torque is presented in [90]. Lebensztajn and Marretto presented the use of Kriging in the optimization of electromagnetic devices, reducing the sample size necessary while maintaining accuracy [91]. Kriging along with genetic algorithms are presented in [92, 93]. A Multi-objective MOGA technique was utilized in [52]. Each of these optimization techniques effectively minimizes torque ripple but leaves little guidance to design.

Features on or near the rotor surface have been utilized to reduce torque harmonics. The use of notches at the rotor surface placed on the primary reluctance path and/or secondary

Parameter	Value	Unit
Pole Pairs	4	
Stator Slots	48	
Number of Phases	3	
Stack Length	83	mm
Rotor Diameter	161.15	mm
Airgap Length	0.75	mm
Magnet Pole Arc % of Pole Pitch	63.8	%
Barrier Type	Single V	
Magnet Thickness	6.48	mm
Magnet Width	16×2	mm
Permanent Magnet Remnant	1.19	T
Permeability of Iron	∞	H/m
Permeability of Bridge Features	$4\pi \cdot 10^{-7}$	H/m

Table 6.1: Example motor parameters.

reluctance path is explored in [94]. Surface dimples on the flat magnet IPM design are studied in [43, 95], where the first utilized finite elements with some analytical method to guide design, and the former is reliant purely on finite elements for design. IPM machines with dimples at the surface and holes near the surface are discussed in [36, 41]. Bread loafing of the secondary reluctance path is considered in [38]. Rotor surface features are staggered in place of skew features in [34]. Barrier design is altered in [96] to minimize torque ripple. Each of these methods has merits that are shown to be effective.

6.2 Application of Analytical Model to Example Machine

The method developed in chapter 4 is validated with a well-known industrialized IPM machine. Details of a well-known industrialized traction motor are included in table 7.1, and the geometry is modeled analytically within Matlab and finite elements within Ansys Maxwell.

Focusing on the effects of the rotor, the stator geometry has been idealized with no slots. Both sinusoidally distributed stator windings and the production configuration of discretely placed windings are modeled. Only the stator winding harmonics interactions with rotor geometry harmonics are considered. With the assumption of infinite permeability, the bridge features are omitted. Airgap fringing in the region of the magnet barrier is not considered.

Design parameters are studied within this section using the analytical winding function model previously validated. Rotor sculpt features are included along with their additional MMF term.

6.2.1 Sculpting Geometry

The sculpted rotor IPM machine geometry design space to be explored is shown on a single pole of the example machine in Figure fig. 6.1. Rotor primary and secondary reluctance paths are shown in green with no bridge features. The stator, shown in gray, continues to have omitted its slot features, and distributed windings, orange, are placed within the airgap.

The primary design parameters are centered on the rotor effects, which include the ratio of primary and secondary reluctance path and sculpt features. The magnet pole arc width is varied. Up to two sets of symmetrically placed sculpt features are placed on the second reluctance path. The symmetrical feature span locations τ_1 and τ_2 define the symmetrical location of the feature in terms of its percentage of the magnet pole arc span. Single asymmetrical features are described with a similar parameter but with only one sculpt feature on the pole. In this single asymmetrical case, the feature location, τ, is set to be positive for right-hand side placement and negative for the left-hand side placement. The depths D_1 and D_2 are measured from the outer surface of the rotor to the root of the sculpt feature. The widths W_1 and W_2 are measured in terms of a single feature percentage of the pole span.

6.3 Model Validation: Radial Flux Density

This section compares the radial flux density results of the analytical model and finite elements while varying: (1) winding type, (2) current, (3) control angle and (4) rotor sculpt features. Figures 6.2–6.5 plot the flux density along the rotors spatial coordinate, θ, over a single pole pair. Both sinusoidal and distributed windings are compared. The q-axis, which is aligned to the rotor minimum reluctance, occurs at $\theta_{elec} = 90°$ and $\theta_{elec} = 270°$. The d-axis is aligned, which is aligned to the smooth rotors permanent magnet maximum flux linkage, occurs at $\theta_{elec} = 0°$, $\theta_{elec} = 180°$, and $\theta_{elec} = 360°$. In all results, the finite element and the analytical model result in comparable flux densities.

Flux densities shown for sinusoidal windings, fig. 6.2, illustrate the changing airgap flux density harmonics with current and control angle. When the phase current is set to zero, only the permanent magnet field is present. As current and current angle increases, the flux density becomes more jagged, with the case of a fully negative d-axis current displaying the most harmonic content. It is clear that as the negative d-axis current becomes dominant, so do the reluctance path harmonics. Harmonic effects of the discretely distributed windings are shown in fig. 6.3. As current increases, so do the airgap reluctance harmonics. In all cases, the analytical model and finite element results agree with reasonable accuracy.

The effects of rotor sculpt features on the second reluctance path are shown in Figures 6.4 and 6.5. A symmetrical pair of sculpting features are shown with distributed windings in fig. 6.4. The flux densities of the smooth rotor and sculpted rotor are plotted. Reduced flux density in the region of the sculpt features is observed, and sculpt features are located approximately at $\theta_{elec} = 30°, 150°, 210°, 270°$. This flux density from the sculpt features is conserved and redistributed across the regions of the second reluctance path. The

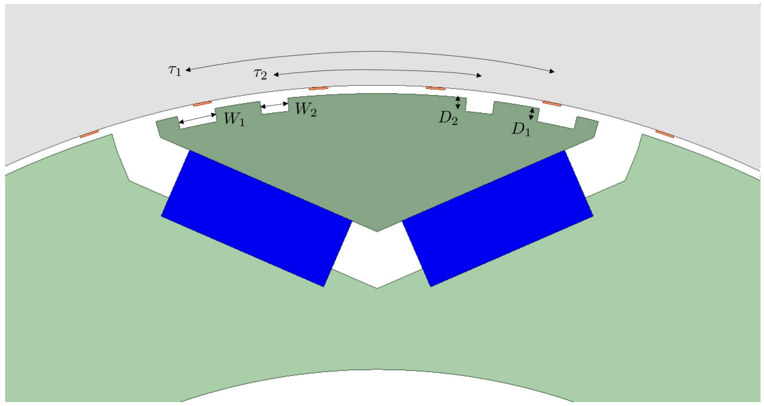

Figure 6.1: Rotor sculpt features.

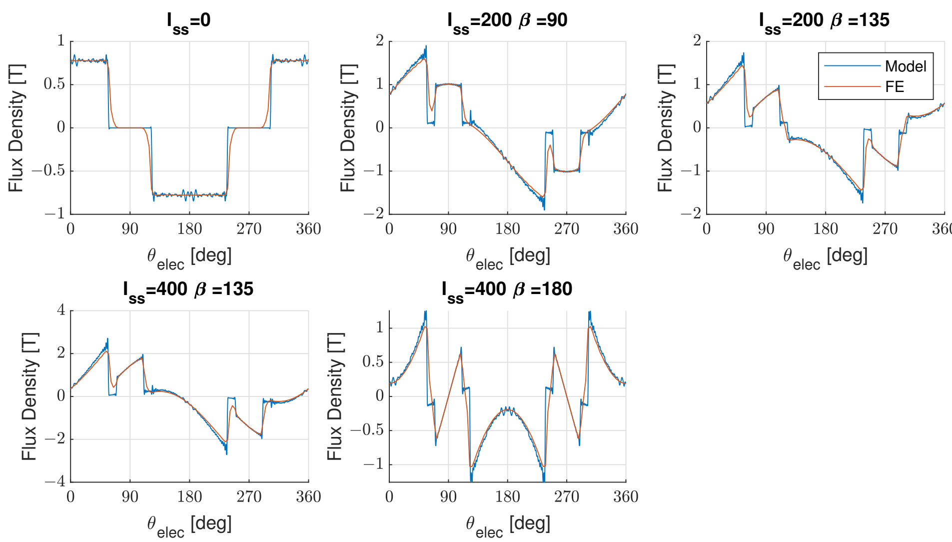

Figure 6.2: Radial flux densities with sinusoidally distributed windings ($N = 200$) at various currents and control angles.

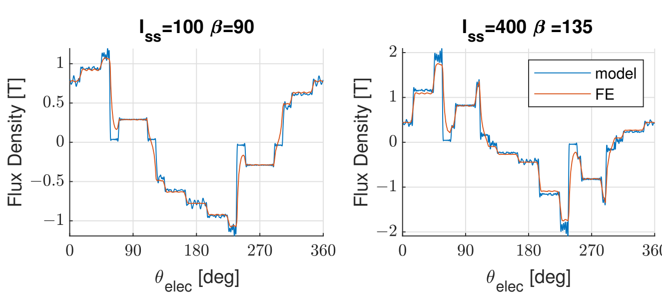

Figure 6.3: Radial flux densities with distributed windings (2 SPP) at various currents and control angles.

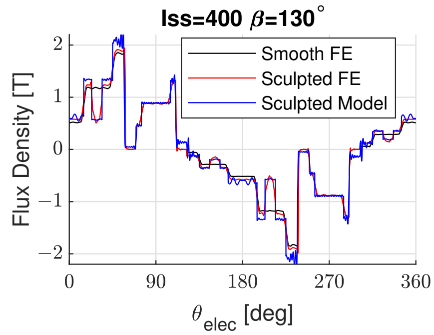

Figure 6.4: Radial flux densities with single symmetrical sculpt feature located at $\tau_1 = 50\%$, $W_1 = 10\%$, and $D_1 = 1.2$ mm.

reluctance flux density single sculpt feature is plotted in fig. 6.5. Similar to the symmetrical sculpt features, the flux density is reduced in the region of the sculpt feature. In all cases, the analytical model and finite element results agree with reasonable accuracy.

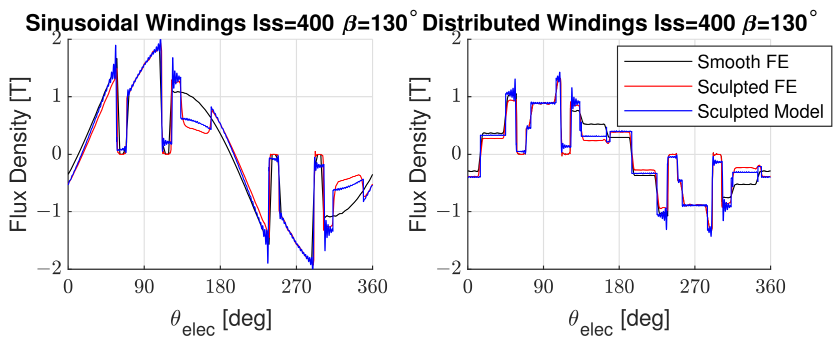

Figure 6.5: Radial flux densities (reluctance only) with single asymmetrical sculpt feature located at $\tau = 50\%$, $W = 20\%$, and $D = 1.2$ mm.

6.4 Model Validation: Torque Ripple

Torque ripple of the smooth rotor IPM, table 7.1, is compared between finite element and the analytical model in fig. 6.6. Good agreement between the finite element and analytical models is observed. The torque ripple effects of two symmetrical rotors sculpt features are demonstrated in fig. 6.7, directly calculated by the analytical model, whereas the finite element model requires two runs, once with and once without sculpting features, to determine the sculpt feature effects.A good correlation between the model and finite elements is demonstrated and shown.

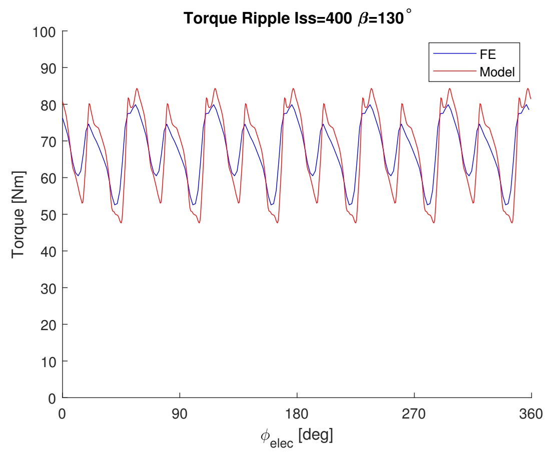

Figure 6.6: Smooth rotor IPM torque ripple.

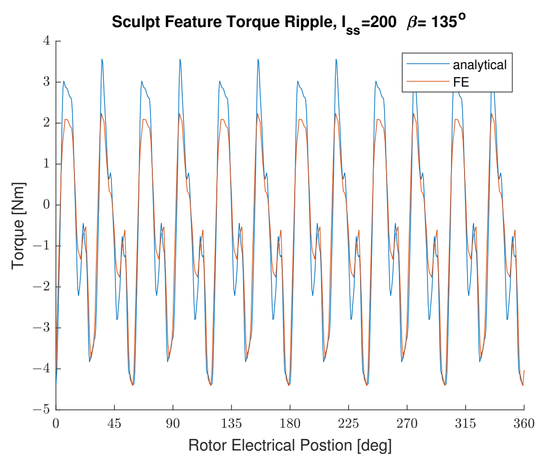

Figure 6.7: Sculpt feature torque ripple.

6.5 Torque Ripple Components

In this section, the torque ripple results of the analytical model are studied while varying current and control angle. Figure 6.8 plots the torque ripple for a complete electrical cycle of the example machine. The torque components for the first reluctance path, second reluctance path, total reluctance torque, magnet torque, and total machine torque are plotted. Magnet torque and its harmonics are dominant at lower currents, but the reluctance paths cannot be ignored. As current is increased, the reluctance torque increases relative to the magnet torque. The stronger field weakening currents cause the contribution of the reluctance features torque to increase. The dominant torque harmonic orders are the 6th and 12th electrical orders. In the design, both the torque harmonic amplitudes and phases of each of the components need to be considered as the sculpt feature design will provide the counter torque at the counter phase.

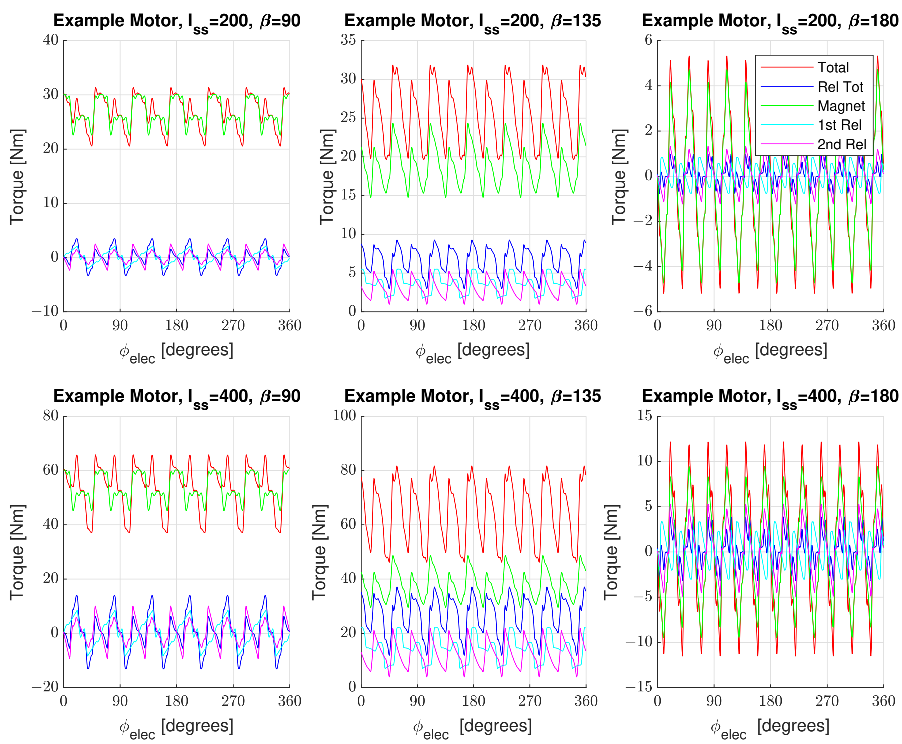

Figure 6.8: Analytical model torque ripple components at various control angles.

6.6 Investigation of Design Features

In this section, the effects of design features are demonstrated to influence both torque harmonic amplitudes and phases. Carefully applied, these effects are used to design counter torque harmonics. Second reluctance path pole arc, sculpt feature type (symmetrical/asymmetrical), sculpt feature location, sculpt feature depth, and sculpt feature width can all be used to design an appropriate counter torque to reduce the machine's torque harmonics. While mildly affecting average torque, the second reluctance path pole arc, τ_p, strongly affects the phase of the 12th electrical order torque harmonic. A single pair of symmetrical sculpt features placed upon the second reluctance path pole arc reduces the average torque. Feature position provides 12th electrical order torque harmonic phasing, and the feature width, and depth directly affect the torque harmonics amplitude. The single asymmetrical feature is shown to increase average torque when placed on a specific side of the second reluctance path pole arc. The asymmetrical feature placement can also be used to modify the phase of both 6th and 12th electrical order torque harmonics. Finally, feature phasor summation is shown to be effective in combining the effects of multiple design features, further providing the ability to design both the amplitude and phase of these minimizing torque harmonics. These relationships provide the necessary intuition to reduce computationally intensive design steps.

6.6.1 Magnet Pole Arc

Magnet pole arc span, τ_m, effects upon the torque harmonics, without rotor sculpt features, are explored. Figure 6.9 shows the average, 6th, and 12th harmonics of torque as a function of τ_m. For this case, magnet torque is dominant. Although not always the case, it is just

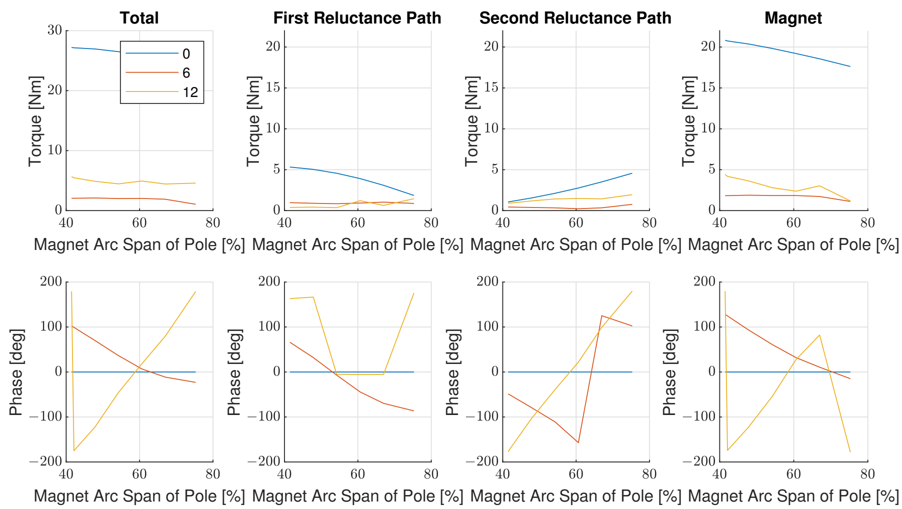

Figure 6.9: Effects of magnet pole arc τ_p loaded at $I_{ss} = 200$ and $\beta = 135°$.

as important to follow the trends of individual torque components. Total, first reluctance, and magnet average machine torque are reduced as the pole arc is increased, and only the second reluctance torque increases the average torque. The 12th order torque harmonic is dominant, with primary contributions from the magnet and the second reluctance path, whereas the 6th order torque harmonic is mostly contributed to by the primary reluctance and magnet. Rotor geometry has a strong influence on the phase of the 12th order torque harmonics, whereas the 6th harmonic is less affected by rotor geometry.

6.6.2 Single Pair Symmetrical Rotor Sculpt Feature

A single symmetrical rotor sculpt feature torque is studied in Figures 6.10–6.12. Only the effects of the sculpt feature torque are plotted. In Figures 6.10 and 6.11, a single sculpt feature position is varied, with fixed width, W_1, and fixed depth, D_1, along the magnet pole arc. Rotor sculpt features hurt average torque, as the phase is 180° out of phase with the smooth rotor average torque. Figure 6.10 compares the analytical model to finite elements and shows precise agreement with the phase and matching trends for torque amplitude.

Using a wider feature width, D_1, fig. 6.11 translates amplitude and phase plots to a phasor representation. The 12th harmonic is the dominant torque in both amplitudes and choice of phase.

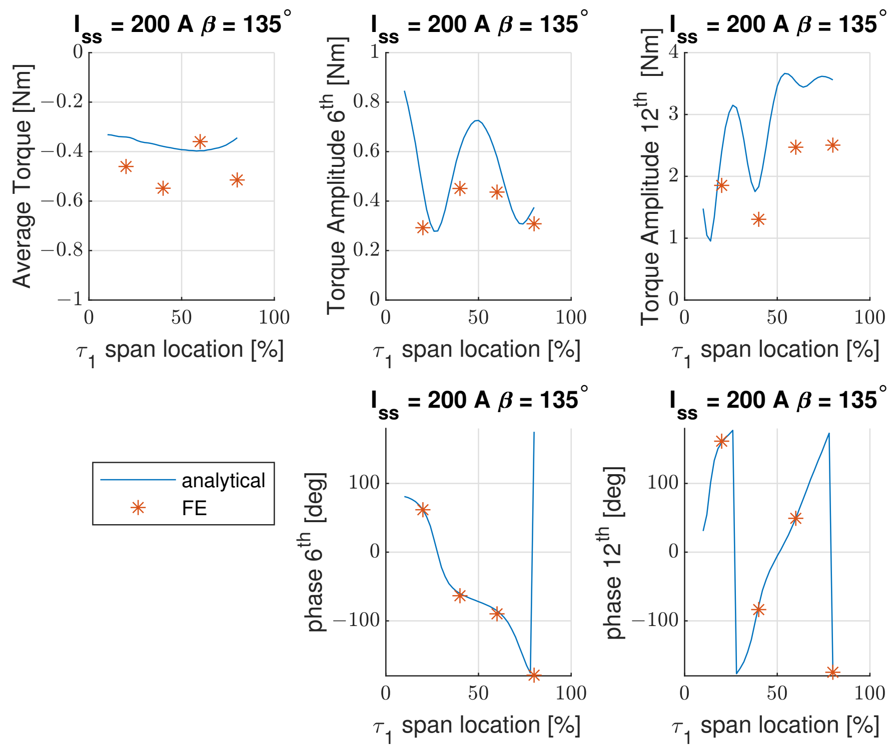

Figure 6.10: Symmetrical sculpt feature effects compared to finite elements: $D_1 = 1.2$ mm, $W_1 = 5\%$.

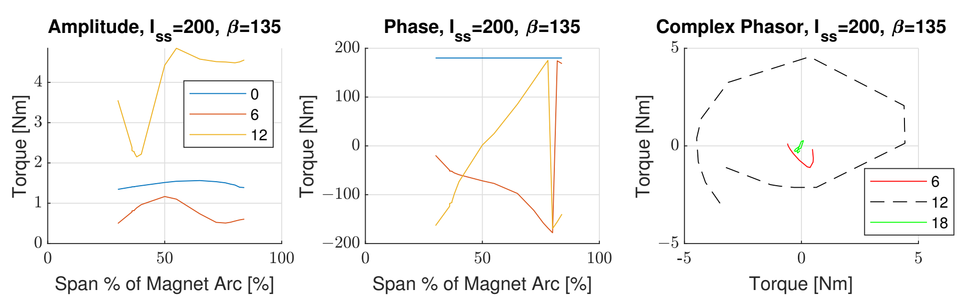

Figure 6.11: Symmetrical sculpt feature effects with phasor diagram: $D_1 = 1.2$ mm, $W_1 = 9\%$.

Figure 6.12 includes the sculpt features width and depth effects. Increasing sculpt feature width, W_1, and/or the sculpt features depth, D_1, increases the amplitude of the sculpt features torque harmonic. The primary influence on the torque harmonic amplitude is the width of the sculpt feature. Sculpt feature width and depth do not affect the torque harmonics phase.

6.6.3 Single Asymmetrical Rotor Sculpt Feature

A single sculpt feature resulting in asymmetrical placement upon the rotor surface is studied in this section. Similar parameters D_1, W_1, and τ_1 are used to describe the features width, depth, and location. In the asymmetrical case, the location, τ_1, is described with the same location parameter, wherein this case, a positive τ_1 results on the right side of fig. 6.1 and a negative τ_1 results in sculpt feature placement on the left hand side. Figure 6.13 compares the model to finite element and shows precise agreement with phase and matching trends for torque amplitude. In the asymmetric sculpt feature case, a torque improvement is possible due to the aligned axis effect from $\tau_1 > 0$. The placement of the sculpt feature allows for the placement of the torque harmonic phase angle across a broad range of phases. Negative values of τ_1 result in the largest amplitudes of the 12th electrical torque harmonic.

6.6.4 Two Symmetrical Rotor Sculpt Features

More than one symmetrical rotor sculpt feature can be used. In this section, it is shown that the components of a first symmetrical feature can be combined with that of the second symmetrical rotor sculpt feature. The MMF-permeance model is validated by comparing to finite element results in fig. 6.7.

To illustrate this concept, the parameters of the two sculpt feature sets of fig. 6.1 are shown in table 6.2. Through vector summation, the two vectors were used to create a 12th

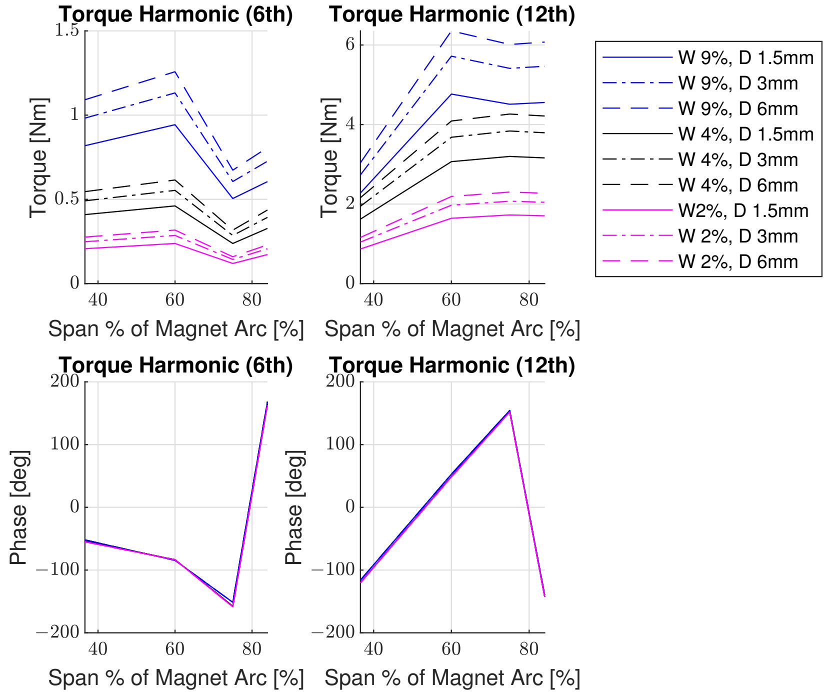

Figure 6.12: Sculpt feature effects $N = 1$.

order counter torque with a phase of $-116°$.

Feature	**Value**	**Unit**
τ_1	82	% of magnet pole arc
τ_2	46.5	% of magnet pole arc span
W_1	5.5	% of pole span
W_2	5.5	% of pole span
D_1	1.2	mm
D_2	1.2	mm

Table 6.2: Two sculpt feature parameters.

Figure 6.14 illustrates the first (red) and second 12th order electrical torque (green) phasors. The two phasors combine to create the effective total phasor (blue). This phasor summation is plotted along with the torque complex mapping of the previous single feature design sweep. These symmetrical rotors sculpt features are designed to mitigate the 12th order electrical torque harmonics to near zero. A single feature or multiple features can be

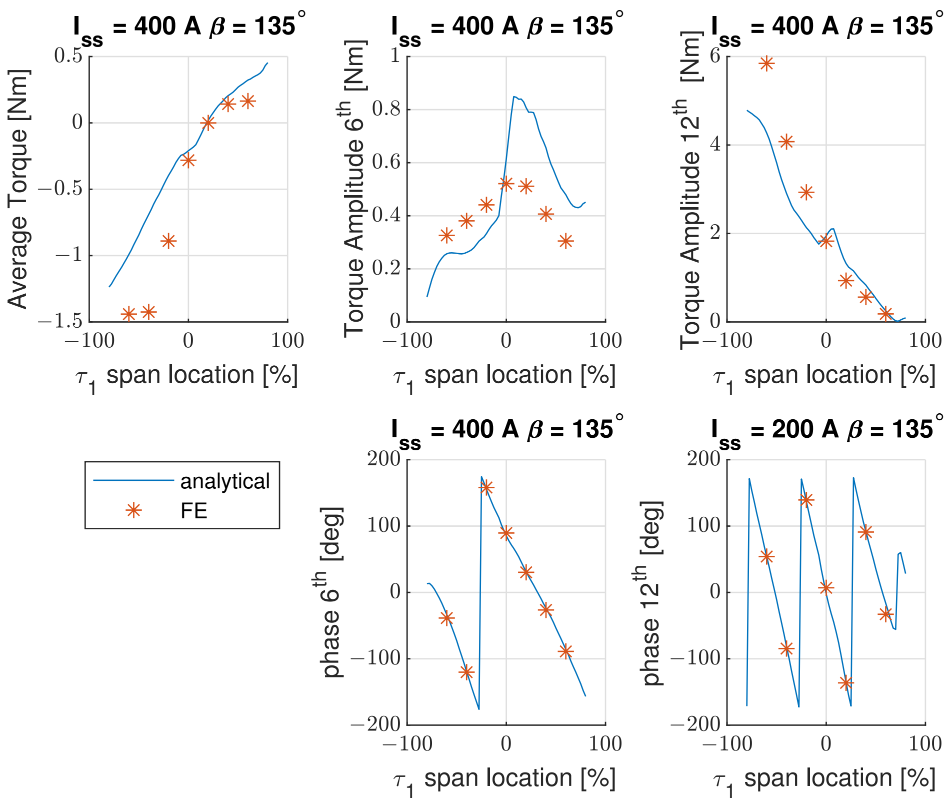

Figure 6.13: Single asymmetrical sculpt feature effects with phasor diagram: $D_1 = 1.2$ mm, $W_1 = 5\%$.

designed to minimize the torque ripple. The sculpt features are not without consequence, as the average torque is negatively affected.

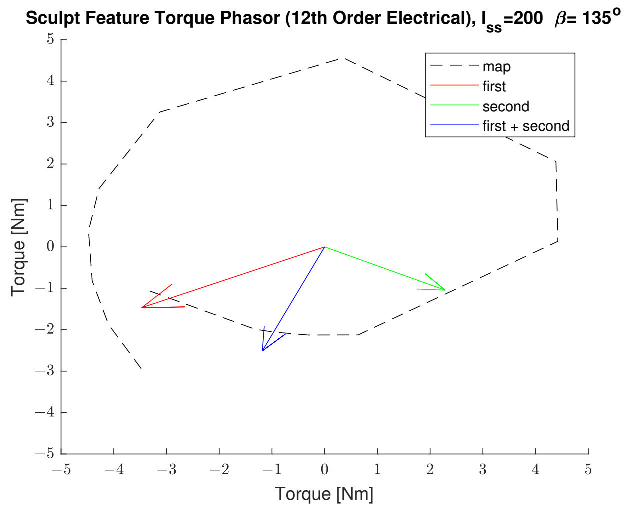

Figure 6.14: Two sculpt features of 12th order electrical torque phasor plot.

6.7 Conclusions

This chapter has presented an analytical modeling and design approach to reduce torque ripple with rotor sculpt features. By carefully placing rotor sculpt features and rotor barrier features, average torque can be maintained while minimizing torque harmonics. Sculpt features torque amplitude and phase are shown to be in close agreement in 6.10 and 6.13. The analytical model accurately predicts the phase in the case of symmetrical and asymmetrical features providing an opportunity to guide design. Contributions of this section include:

- A new analytical winding factor modeling approach for the single V IPM machine relating the rotor's first reluctance feature, second reluctance feature, permanent magnet features, sculpt features, and stator windings to the resulting torque harmonics;

- An analytical modeling approach accounting for both symmetrical and torque aligning asymmetrical rotor sculpt features;

- Results from the analytical model providing valuable insights for identifying rotor feature design improvements;
- Design approach for placement of rotor sculpt features to minimize torque ripple while maintaining average torque;
- Demonstration of close agreement of radial flux density and torque harmonics results between the analytical model and that of finite element results.

These results enable better design insight and an efficient design process through the use of an analytical model.

Chapter 7

Optimal Design for Minimal Torque Ripple

7.1 Methods

This section describes the electric machine parameters, sculpt feature geometry, analytical modeling, and optimization method utilized to minimize torque harmonics.

7.2 Electric Machine Parameters

To evaluate the analytical MMF permanence method, a single barrier IPM machine has been modeled using both FE and analytical methods. The model is constructed and evaluated based on a well-known smooth rotor industrial IPM machine. Parameters of this machine are included in section 7.2.

A schematic of a two-pole rotor describing the sculpting features to this machine is given in fig. 7.1. Variables Y_1 and Y_2, define sculpt feature location in terms of half of the magnet pole arc span, α_m, where Y_1 is a positive percentage and Y_2 as a negative percentage (counter-clockwise position). Feature width Z_1 and Z_2, define the sculpt feature width in terms of percentage of the magnet pole arc span, α_m. A single sculpt feature depth, D_1, is utilized for both features. The asymmetrical features will be used to take advantage of

Parameter	Value	Unit
Pole Pairs	4	
Stator Slots	48	
Number of Phases	3	
Stack Length	83	mm
Rotor Diameter	161.15	mm
Air Gap Length	0.75	mm
Magnet Pole Arc % of Pole Pitch	63.8	%
Barrier Type	Single V	
Magnet Thickness	6.48	mm
Magnet Width	16x2	mm
Permanent Magnet Remnant	1.19	T
Permeability of Iron	∞	$\frac{mkg}{s^2A^2}$
Permeability of Bridge Features	$4\pi \cdot 10^{-7}$	$\frac{mkg}{s^2A^2}$

Table 7.1: Motor Parameters

average the possible torque increase but also to target specific torque harmonics.

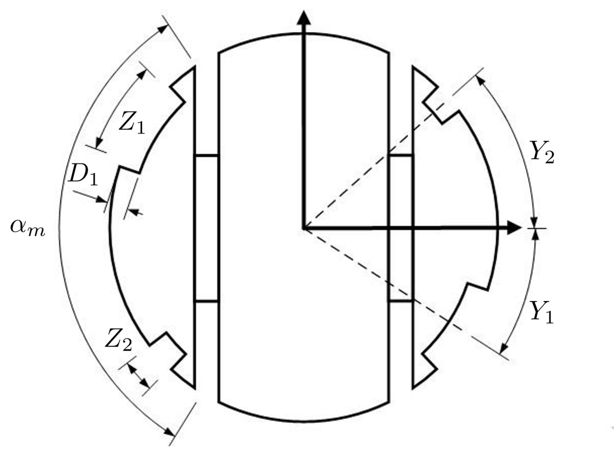

Figure 7.1: Two pole equivalent Scrupted Rotor IPM model

7.3 Minimization of Torque Harmonics

The developed analytical model is used to design sculpting features upon the smooth rotor machine defined in Table section 7.2. This computationally efficient model is integrated with a genetic optimization tool, GOSET [97], to determine the geometry to minimize the torque ripple via targeted torque harmonics. All optimization is done with a fixed current I_{ss} and angle β, in the constant torque region.

7.3.1 Optimization Methodology

The design optimization of sculpt features to minimize the 6^{th} or 12^{th} order torque component amplitude. In previous work, it was shown that the analytical model predicts sculpt feature effects of torque harmonic phase precisely and the amplitude with modest accuracy [98]. Starting with a smooth rotor, optimizing with sculpting features is done using the smooth rotor FE result and the sculpted rotor analytical model. Addressing both the amplitude and phase, the torque harmonic design objective is expressed as a complex number. The targeted smooth rotor FE torque harmonic is rotated 180°, T^*, to determine the desired torque harmonic produced by the sculpt features.

$$\vec{T}^*(n) = \vec{T}_{sm}^{FE}(n)e^{\vec{i}\pi} \tag{7.1}$$

To minimize the torque harmonic, the difference between the finite element smooth rotor torque harmonic conjugate, $\vec{T}^*(n)$, and the analytical models sculpt feature torque harmonic effect, $\vec{T}_{ScEff}^{MDL}$, further defines the optimization objectives in (7.3) and (7.4). Subtracted in complex form, the amplitude of the difference is later used in the objective function.

$$\vec{T}_{ScEff}^{MDL}(n) = \vec{T}_{sc}^{MDL}(n) - \vec{T}_{sm}^{MDL}(n) \tag{7.2}$$

The first, (7.3), utilizes the sculpt feature location, $Y2$, width, $Z2$, and depth D_1. The second, (7.4), utilizes the sculpt feature location, Y_1, width, Z_1, and depth D_1. The optimization problems utilize Y_1 are Y_2 to respectively minimize the 6^{th} order and 12^{th} order torque harmonics. Feature locations Y_1 and Y_2 set the phase of the torque harmonics introduced by the sculpt feature [98]. Feature Z_1 and Z_2 are designed to set the amplitude of injected torque harmonic.

The main design constraint of the rotor is mechanical stress. The centrifugal forces coupled with the stress intensification due to the barrier features. Thinner bridges increase magnetic performance but increase stress. For this analysis, the bridge thickness is left constant, and the sculpt feature placement is varied. Stress concentrations occur in either the bridge or sculpt feature as shown in fig. 7.2. At 5000rpm the rotor stresses, shown in fig. 7.3, near yield as the sculpt feature approaches the barrier. A further constraint is applied on feature location in combination with feature size to avoid manufacturing and mechanical limitations of feature placement near the barriers.

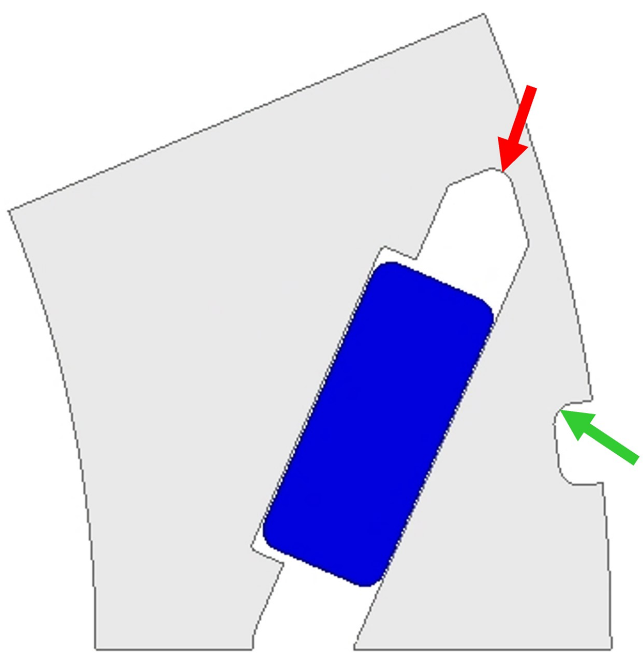

Figure 7.2: Rotor Sculpt Feature, bridge stress (red arrow), sculpt stress (green arrow)

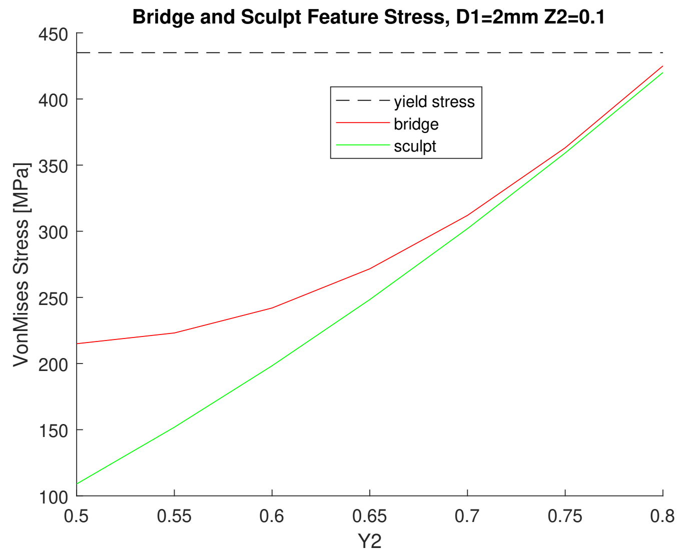

Figure 7.3: Rotor Stresses, 5000 rpm, D1=2mm, Z1=0.1

$$\begin{aligned}
\min_{T,i_d,i_q} \quad & \left| \vec{T}^*(12) - \vec{T}^{MDL}_{ScEff}(12) \right| \\
\text{s.t.} \quad & -90\% < Y_2 < 0\% \\
& 2\% < Z_2 < 50\% \\
& |Y_2| + |Z_2| \leq 91\%
\end{aligned} \tag{7.3}$$

$$\begin{aligned}
\min_{T,i_d,i_q} \quad & \left| \vec{T}^*(6) - \vec{T}^{MDL}_{ScEff}(6) \right| \\
\text{s.t.} \quad & 30\% < Y_1 < 90\% \\
& 2\% < Z_1 < 50\% \\
& |Y_1| + |Z_1| \leq 91\%
\end{aligned} \tag{7.4}$$

Each problem was set up with a population of 200 and 10 generations. To confirm the genetic algorithm's accuracy, optimizations were repeated multiple times to confirm stable results.

7.4 Optimal Designs

The optimization process minimized the 12^{th} harmonic or 6^{th} harmonic torque, three designs are of interest. Table 7.2, highlights these designs. Design 1 designates the starting point of the smooth rotor design. Design 2 and Design 3 seek to minimize the 12^{th} order harmonic of torque. Design 4 seeks to minimize the 6^{th} order torque harmonic.

	Y1	Z1	Y2	Z2	D1
Design 1	smooth rotor				
Design 2	-	-	-86.6%	4.3%	2mm
Design 3	-	-	-32.1%	20.3%	2mm
Design 4	75.9%	14.1%	-	-	2mm

Table 7.2: Analytical Model Sculpt Feature Designs

Sculpt feature effects, based on (7.2), are shown in Figs. 7.4 and 7.5, examining which shows the torque resulting from the analytical design relative to the objective and FE results. Sculpt feature effects to average torque, fig. 7.4, shows reduced average torque for both Design 2 and Design 3. Increased average torque is achieved with Design 4. Both the radial flux density fundamental amplitude and phase account for these changes. Torque amplitude trends are the same for all designs but with limited accuracy. Sculpt feature effects on torque harmonics of the designs are shown in Fig. fig. 7.5. Designs 2 and 3 are shown analytically to achieve the target T^*, when checked in FE Design 2 underachieves the desired torque amplitude, and Design 3 overachieves it. A strong correlation holds between the analytical model sculpt feature torque harmonic effect phase and that found with the finite element model. Design 4 shows a good correlation in torque harmonic phase between the analytical model and finite element model, and the amplitude shows that the effect to the 6th harmonic is limited.

The three designs proposed to minimize torque ripple, table 7.2, are confirmed in FE and

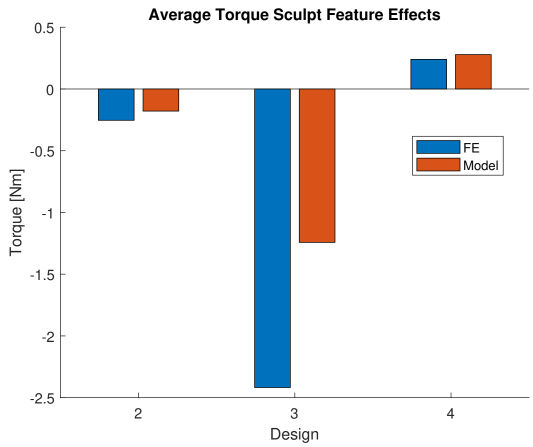

Figure 7.4: Comparison of Sculpt Feature Effects to Average Torque (FE and Model), $I_{ss} = 200A, \beta = 112°$

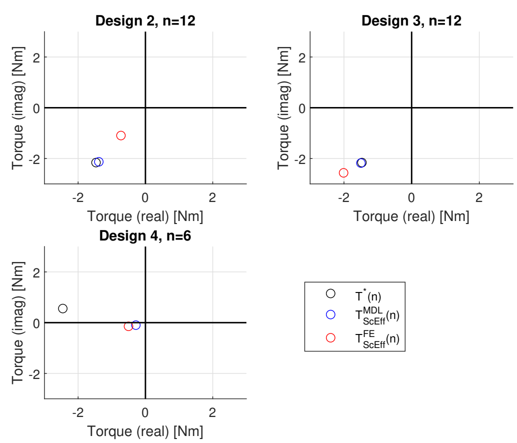

Figure 7.5: Comparison of Sculpt Feature Design Effects to Torque Ripple (FE and Model), $I_{ss} = 200A, \beta = 112°$

shown in fig. 7.6. Design 2 is shown to reduce average torque 1%, reduce the 6th torque harmonic 3%, and reduce the 12th harmonic of torque ripple by 50%. Design 3 reduces average torque by 8%, increases the 6th harmonic amplitude by 6%, and the 12th harmonic by 75%. Design 4 improves average torque by 1%, reduces the 6th torque harmonic by 17%, and reduces the 12th harmonic by 23%.

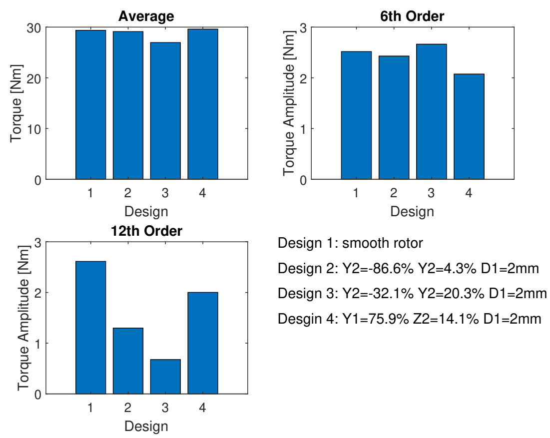

Figure 7.6: FE Torque Comparison of Analytical Model Optimized Sculpt Features, $I_{ss} = 200A, \beta = 180°$

7.5 Finite Element Detailed Search of Design Space

To validate the optimized analytical design, a detailed search, in the region of the designs in table 7.2, is performed in FE. Figures 7.7, 7.8, and 7.9 show the amplitude of the machine's torque harmonic as a function of the design variables. The constraint, $|Y_x| + |Z_x| \leq 91\%$, is represented as a dashed red line in Figs. 7.7 and 7.9. For all extended searches, the analytical designs are designated with a red asterisk. Comparing Design 2 to extended search results in fig. 7.7 shows the genes identified in table 7.2 are in proximity of the minimum and design optimum within 3%. Full cancellation of the 12^{th} harmonic is not possible with design 2 since the geometry achieving the torque harmonic minimum is beyond the allowable design space. The comparison between design 3 and extended search in fig. 7.8 shows the analytical design is within the optimum 2% and with a small modification able to fully cancel the torque harmonic. Figure 7.9, shows that Design 4 cannot fully cancel the intended torque harmonic but is at the minimum along with the constraint. For each design, gradients around the optimum are approximately $\frac{0.25Nm}{\%}$ further showing the analytical design sufficiently finds the region of optimum for each design. The new analytical model coupled with GOSET optimization algorithms yields similar geometry and performance as the FE extended search method.

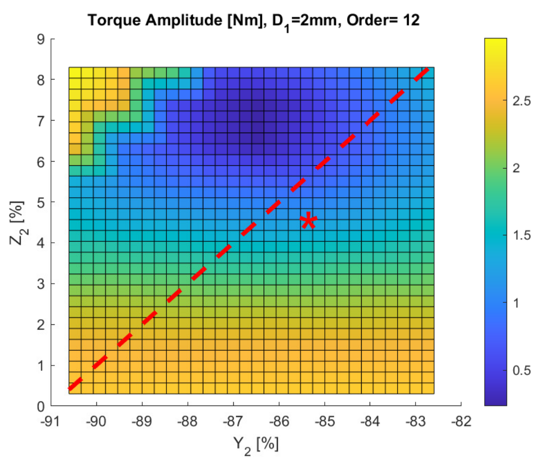

Figure 7.7: Finite Element Extended Search of Design 2, $I_{ss} = 200A, \beta = 112°$, Constraint: Dashed Red Line, Analytical Design: Red *

7.6 Exhaustive Search

The effectiveness of the analytical model with optimization is compared to finite elements and an exhaustive search. Variables Y_1, Y_2, Z_1, and Z_2 are swept, with an increment of 1%, over the same range as the optimization problem. Figures 7.12 7.10 and 7.11 plot the amplitude of the average torque and 6th and 12th order torque ripple. The optimized designs are plotted as stars. The optimization of each design using the analytical model required

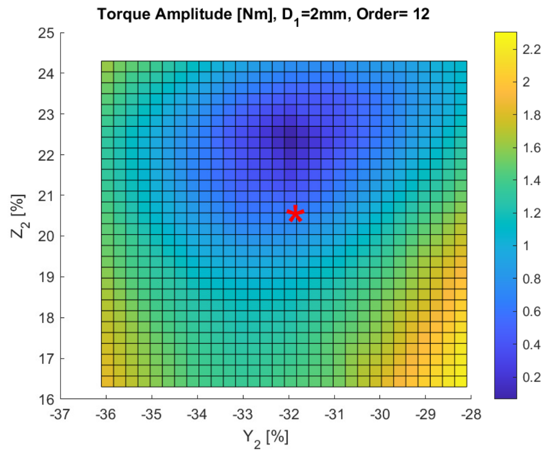

Figure 7.8: Finite Element Extended Search of Design 3, $I_{ss} = 200A, \beta = 112°$, Analytical Design: Red *

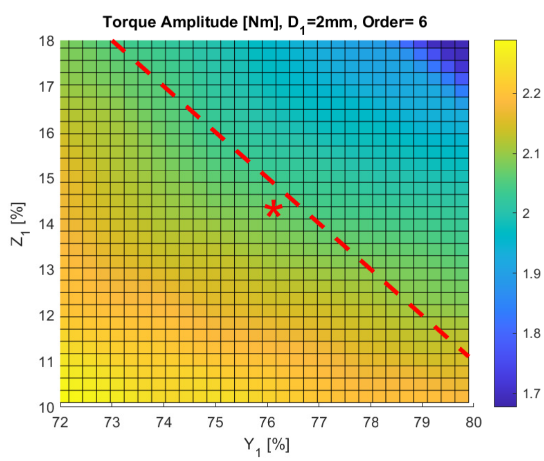

Figure 7.9: Finite Element Extended Search of Design 4, $I_{ss} = 200A, \beta = 112°$, Constraint: Dashed Red Line, Analytical Design: Red *

approximately 45 minutes, whereas an exhaustive search within FE required 72 hours.

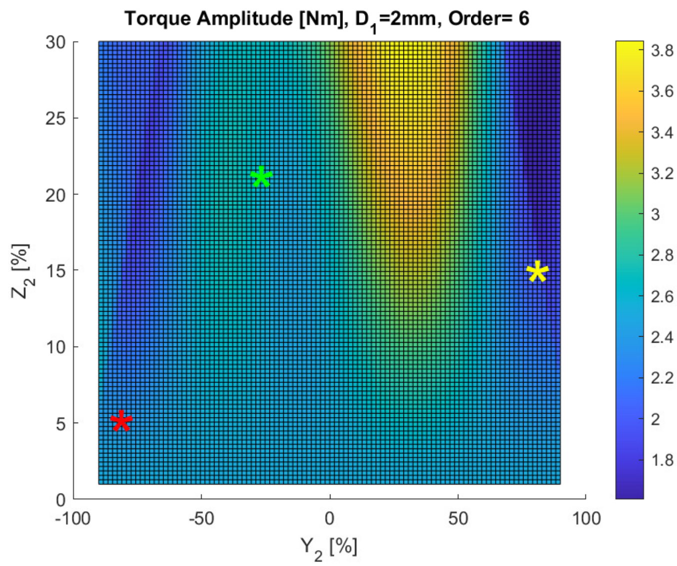

Figure 7.10: Finite Element Exhaustive Search, Order = 6, $I_{ss} = 200A, \beta = 112°$, Design 2 (red), Design 3 (green), Design 4 (yellow)

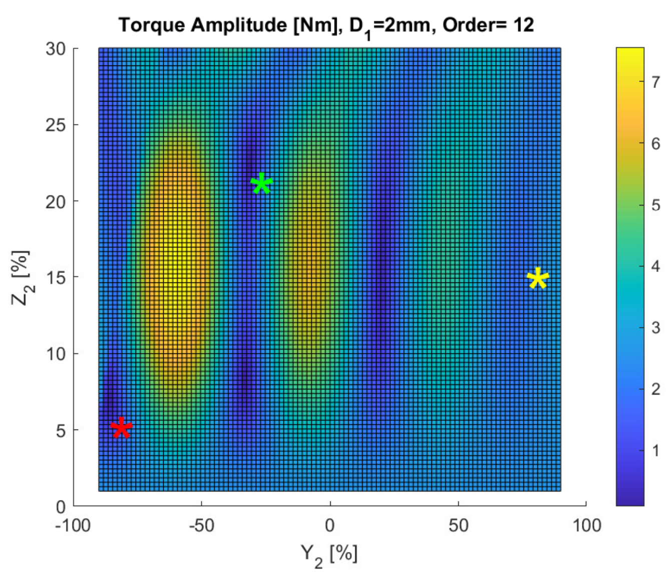

Figure 7.11: Finite Element Exhaustive Search, Order = 12, $I_{ss} = 200A, \beta = 112°$, Design 2 (red), Design 3 (green), Design 4 (yellow)

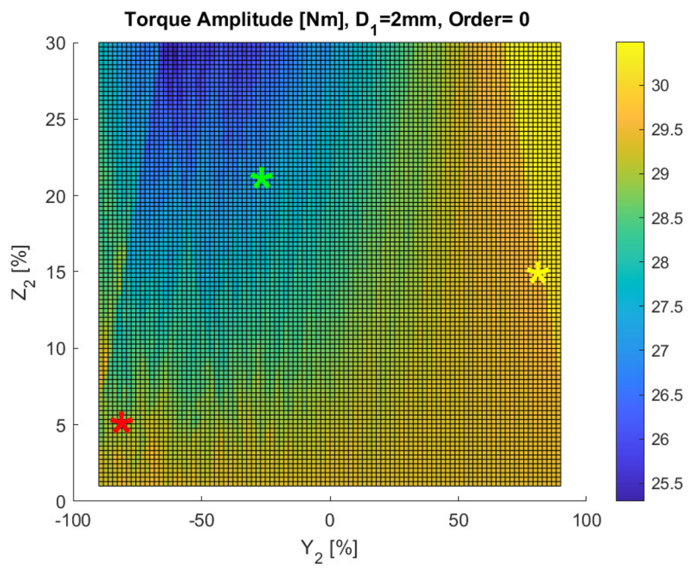

Figure 7.12: Finite Element Exhaustive Search, Order = 0, $I_{ss} = 200A, \beta = 112°$, Design 2 (red), Design 3 (green), Design 4 (yellow)

7.7 Conclusion

This chapter has presented an analytical modeling and design optimization approach to reduce torque ripple with rotor sculpt features. By carefully placing rotor sculpt features and rotor barrier features, average torque can be maintained while torque harmonics are minimized. An average torque increase is presented in fig. 7.4, while reduction of harmonics is presented in fig. 7.5. Contributions of this chapter include:

1. Asymmetrical sculpting features onto the rotor can address the torque harmonic contents, specifically the 6^{th} and the 12^{th} orders.

2. An analytical MMF model is developed and is used to guide the design process in place of FEA.

3. The analytical model with GOSET optimization yields similar geometry as the benchmarked FE method with an extended search.

4. The analytical model with GOSET optimization yields similar torque pulsation reduction as the benchmarked FE method with an extended search.

5. A single use of the analytical model to design sculpt features, has saved significant computational time.

6. Non-standard IPM design can result in the reduction of torque harmonics without a sacrifice of average torque, however a cost of additional control complexity.

7. Given a predefined torque harmonic target, an analytical model was developed and used with optimization to design sculpt features to minimize ripple.

Chapter 8

Conclusion

8.1 Closing

The purpose of this dissertation is to investigate the design of interior permanent magnet machines with the look to minimize torque pulsations and improve torque density through the design of the rotor. The development of an MMF permeance model for the traditional IPM machine is presented. Treatment of surface features is at the center of this work. Analysis of the airgap surface features is made possible through the use of an additional MMF term, based upon the equivalent magnetic dipole. Evaluation of the winding, permeance, and surface harmonics will is presented alongside their interactions. Further improvement of torque density and torque ripple is developed through the use of these surface harmonics. A design process allowing for vector summation is presented. Torque ripple is minimized with the analytical model and optimization enabling quick and efficient design.

8.2 Future Work

Future work includes an extension of the winding factor model to a broader set of problems. The following questions are posed:

- How can the MMF Permeance method be extended to include the effects of fringing?

- What are the impacts of saturation to torque harmonics?
- How can the MMF Permeance method be extended to treat the saturated case?
- Can the rotor equivalent magnetic current be extended to problems solved in finite elements?
- Can the torque harmonics be improved across multiple operating points, or the entire operating range?
- How do the sculpt feature affect the windage losses and convection coefficients?
- Can the optimization speed be further improved using a gradient based optimization method?
- How can the torque ripple minimization process be developed to handle different operating temperatures?
- How does the proposed design methods fit in with the larger design process?

BIBLIOGRAPHY

BIBLIOGRAPHY

[1] S. Trout, "Ecce 2018," Sep 2018.

[2] Geek3, "Magnetic dipole field around a small current loop." 2020, [Wikipedia, the free encyclopedia ; Online; created Sept, 2010]. [Online]. Available: https://commons.wikimedia.org/w/index.php?curid=11621875

[3] H. A. Toliyat, *Electric machines: modeling, condition monitoring, and fault diagnosis*. CRC Press, 2017.

[4] D. K. Cheng, *Field and wave electromagnetics*. Addison-Wesley, 1989.

[5] R. Islam, I. Husain, A. Fardoun, and K. McLaughlin, "Permanent-magnet synchronous motor magnet designs with skewing for torque ripple and cogging torque reduction," *IEEE Transactions on Industry Applications*, vol. 45, no. 1, pp. 152–160, 2009.

[6] R. Cao, C. Mi, and M. Cheng, "Quantitative comparison of flux-switching permanent-magnet motors with interior permanent magnet motor for ev, hev, and phev applications," *IEEE Transactions on Magnetics*, vol. 48, no. 8, pp. 2374–2384, 2012.

[7] D. Wu and Z. Q. Zhu, "Design tradeoff between cogging torque and torque ripple in fractional slot surface-mounted permanent magnet machines," *IEEE Transactions on Magnetics*, vol. 51, no. 11, pp. 1–4, 2015.

[8] X. Liu, H. Chen, J. Zhao, and A. Belahcen, "Research on the performances and parameters of interior pmsm used for electric vehicles," *IEEE Transactions on Industrial Electronics*, vol. 63, no. 6, pp. 3533–3545, 2016.

[9] G. Pellegrino, A. Vagati, P. Guglielmi, and B. Boazzo, "Performance comparison between surface-mounted and interior pm motor drives for electric vehicle application," *IEEE Transactions on Industrial Electronics*, vol. 59, no. 2, pp. 803–811, 2012.

[10] G. Pellegrino, A. Vagati, B. Boazzo, and P. Guglielmi, "Comparison of induction and pm synchronous motor drives for ev application including design examples," *IEEE Transactions on Industry Applications*, vol. 48, no. 6, pp. 2322–2332, 2012.

[11] Z. Yang, F. Shang, I. P. Brown, and M. Krishnamurthy, "Comparative study of interior permanent magnet, induction, and switched reluctance motor drives for ev and hev applications," *IEEE Transactions on Transportation Electrification*, vol. 1, no. 3, pp. 245–254, 2015.

[12] D. Zarko, D. Ban, and T. Lipo, "Analytical calculation of magnetic field distribution in the slotted air gap of a surface permanent-magnet motor using complex relative air-gap permeance," *IEEE Transactions on Magnetics*, vol. 42, no. 7, pp. 1828–1837, 2006.

[13] L. J. Wu, Z. Q. Zhu, D. Staton, M. Popescu, and D. Hawkins, "An improved subdomain model for predicting magnetic field of surface-mounted permanent magnet machines accounting for tooth-tips," *IEEE Transactions on Magnetics*, vol. 47, no. 6, pp. 1693–1704, 2011.

[14] B. Kim and T. A. Lipo, "Analysis of a pm vernier motor with spoke structure," *IEEE Transactions on Industry Applications*, vol. 52, no. 1, pp. 217–225, 2016.

[15] G. Dajaku, "Open circuit air-gap field calculation of a new pm machine having a combined spm and spoke type magnets," *IEEE Transactions on Magnetics*, pp. 1–1, 2020.

[16] G. Dajaku, "Analytical analysis of electromagnetic torque and magnet utilization factor for two different pm machines with spm and hupm rotor topologies," *IEEE Transactions on Magnetics*, vol. 57, no. 6, pp. 1–9, 2021.

[17] J.-W. Kwon, M. Li, and B.-I. Kwon, "Design of v-type consequent-pole ipm machine for pm cost reduction with analytical method," *IEEE Access*, vol. 9, pp. 77 386–77 397, 2021.

[18] K. D. Hoang, "Simplified analytical model for rapid evaluation of interior pm traction machines considering magnetic nonlinearity," *IEEE Open Journal of the Industrial Electronics Society*, vol. 1, pp. 340–354, 2020.

[19] W. Hu, X. Zhang, Y. Lei, Q. Du, L. Shi, and G. Liu, "Analytical model of air-gap field in hybrid excitation and interior permanent magnet machine for electric logistics vehicles," *IEEE Access*, vol. 8, pp. 148 237–148 249, 2020.

[20] M. M. Ghahfarokhi, E. Amiri, S. T. Boroujeni, and A. D. Aliabad, "On-load analytical modeling of slotted interior magnet synchronous machines using magnetic islands method," *IEEE Access*, vol. 8, pp. 95 360–95 367, 2020.

[21] M. Hajdinjak and D. Miljavec, "Analytical calculation of the magnetic field distribution in slotless brushless machines with u-shaped interior permanent magnets," *IEEE Transactions on Industrial Electronics*, vol. 67, no. 8, pp. 6721–6731, 2020.

[22] M. S. Mirazimi and A. Kiyoumarsi, "Magnetic field analysis of synrel and pmasynrel machines with hyperbolic flux barriers using conformal mapping," *IEEE Transactions on Transportation Electrification*, vol. 6, no. 1, pp. 52–61, 2020.

[23] F. Momen, K. Rahman, Y. Son, and P. Savagian, "Electrical propulsion system design of chevrolet bolt battery electric vehicle," in *2016 IEEE Energy Conversion Congress and Exposition (ECCE)*, 2016, pp. 1–8.

[24] K. Namiki, K. Murota, and M. Shoji, "High performance motor and inverter system for a newly developed electric vehicle," *SAE Technical Paper Series*, 2018.

[25] S. Jurkovic, K. Rahman, B. Bae, N. Patel, and P. Savagian, "Next generation chevy volt electric machines; design, optimization and control for performance and rare-earth mitigation," in *2015 IEEE Energy Conversion Congress and Exposition (ECCE)*, 2015, pp. 5219–5226.

[26] T. Kanayama, E. Yanagida, S. Kano, B. Geller, Y. Nakao, and M. Fukao, "Development of new hybrid system for mid-size suv," *SAE Technical Paper Series*, 2020.

[27] S. Hayslett, K. Van Maanen, W. Wenzel, and T. Husain, "The 48-v mild hybrid: Benefits, motivation, and the future outlook," *IEEE Electrification Magazine*, vol. 8, no. 2, pp. 11–17, 2020.

[28] B. Sarlioglu and C. T. Morris, "More electric aircraft: Review, challenges, and opportunities for commercial transport aircraft," *IEEE Transactions on Transportation Electrification*, vol. 1, no. 1, pp. 54–64, 2015.

[29] M. van der Geest, H. Polinder, J. A. Ferreira, and M. Christmann, "Power density limits and design trends of high-speed permanent magnet synchronous machines," *IEEE Transactions on Transportation Electrification*, vol. 1, no. 3, pp. 266–276, 2015.

[30] N. Bianchi, D. Durello, and A. Fasolo, "Relationship between rotor losses and size of permanent-magnet machines," *IEEE Transactions on Industry Applications*, vol. 49, no. 5, pp. 2015–2023, 2013.

[31] T. A. Lipo and W. Liu, "Comparison of ac motors to an ideal machine part i—conventional ac machines," *IEEE Transactions on Industry Applications*, vol. 56, no. 2, pp. 1346–1355, 2020.

[32] J. F. Miller and D. Howell, "The ev everywhere grand challenge," in *2013 World Electric Vehicle Symposium and Exhibition (EVS27)*, 2013, pp. 1–6.

[33] Surong Huang, Jian Luo, F. Leonardi, and T. A. Lipo, "A general approach to sizing and power density equations for comparison of electrical machines," *IEEE Transactions on Industry Applications*, vol. 34, no. 1, pp. 92–97, 1998.

[34] Z. S. Du and T. A. Lipo, "Torque ripple minimization in interior permanent magnet machines using axial pole shaping," in *2018 IEEE Energy Conversion Congress and Exposition (ECCE)*, 2018, pp. 6922–6929.

[35] S. Jang, H. Park, J. Choi, K. Ko, and S. Lee, "Magnet pole shape design of permanent magnet machine for minimization of torque ripple based on electromagnetic field theory," *IEEE Transactions on Magnetics*, vol. 47, no. 10, pp. 3586–3589, 2011.

[36] S. Lee, G. Kang, J. Hur, and B. Kim, "Stator and rotor shape designs of interior permanent magnet type brushless dc motor for reducing torque fluctuation," *IEEE Transactions on Magnetics*, vol. 48, no. 11, pp. 4662–4665, 2012.

[37] S. A. Evans, "Salient pole shoe shapes of interior permanent magnet synchronous machines," in *The XIX International Conference on Electrical Machines - ICEM 2010*, 2010, pp. 1–6.

[38] U. Seo, Y. Chun, J. Choi, P. Han, D. Koo, and J. Lee, "A technique of torque ripple reduction in interior permanent magnet synchronous motor," *IEEE Transactions on Magnetics*, vol. 47, no. 10, pp. 3240–3243, 2011.

[39] K. Wang, Z. Q. Zhu, G. Ombach, and W. Chlebosz, "Optimal rotor shape with third harmonic for maximizing torque and minimizing torque ripple in ipm motors," in *2012 XXth International Conference on Electrical Machines*, 2012, pp. 397–403.

[40] A. Kioumarsi, M. Moallem, and B. Fahimi, "Mitigation of torque ripple in interior permanent magnet motors by optimal shape design," *IEEE Transactions on Magnetics*, vol. 42, no. 11, pp. 3706–3711, 2006.

[41] Y. Shimizu, S. Morimoto, M. Sanada, and Y. Inoue, "Reduction of torque ripple in double-layered ipmsm for automotive applications by rotor structure modification," in *2017 IEEE 12th International Conference on Power Electronics and Drive Systems (PEDS)*, 2017, pp. 429–434.

[42] K. Yamazaki, M. Kumagai, T. Ikemi, and S. Ohki, "A novel rotor design of interior permanent-magnet synchronous motors to cope with both maximum torque and iron-loss reduction," *IEEE Transactions on Industry Applications*, vol. 49, no. 6, pp. 2478–2486, 2013.

[43] G. Kang, Y. Son, G. Kim, and J. Hur, "A novel cogging torque reduction method for interior-type permanent-magnet motor," *IEEE Transactions on Industry Applications*, vol. 45, no. 1, pp. 161–167, 2009.

[44] J. Liang, A. Parsapour, M. Moallem, and B. Fahimi, "Asymmetric rotor surface design in interior permanent magnet synchronous motors for torque ripple mitigation," in *2019 IEEE International Electric Machines Drives Conference (IEMDC)*, 2019, pp. 727–732.

[45] J. Liang, A. Parsapour, Z. Yang, C. Caicedo-Narvaez, M. Moallem, and B. Fahimi, "Optimization of air-gap profile in interior permanent-magnet synchronous motors for

torque ripple mitigation," *IEEE Transactions on Transportation Electrification*, vol. 5, no. 1, pp. 118–125, 2019.

[46] K. Yamazaki and K. Utsunomiya, "Mechanism of torque ripple generation by time and space harmonic magnetic fields in interior permanent magnet synchronous motors," in *2020 International Conference on Electrical Machines (ICEM)*, vol. 1, 2020, pp. 232–238.

[47] M. Ibrahim and P. Pillay, "Aligning the reluctance and magnet torque in permanent magnet synchronous motors for improved performance," in *2018 IEEE Energy Conversion Congress and Exposition (ECCE)*, 2018, pp. 2286–2291.

[48] P. Winzer and M. Doppelbauer, "Comparison of synchronous machine designs with displaced reluctance axis considering losses and iron saturation," in *2015 IEEE International Electric Machines Drives Conference (IEMDC)*, 2015, pp. 1801–1807.

[49] M. Doppelbauer and P. Winzer, "A lighter motor for tomorrow's electric car," *IEEE Spectrum*, vol. 54, no. 7, pp. 26–31, 2017.

[50] S. Hayslett and E. Strangas, "Design and analysis of aligned axis interior permanent magnet machines considering saturation," in *2019 IEEE International Electric Machines Drives Conference (IEMDC)*, 2019, pp. 686–692.

[51] S. Han, T. M. Jahns, and W. L. Soong, "Torque ripple reduction in interior permanent magnet synchronous machines using the principle of mutual harmonics exclusion," in *2007 IEEE Industry Applications Annual Meeting*, 2007, pp. 558–565.

[52] G. Pellegrino and F. Cupertino, "Fea-based multi-objective optimization of ipm motor design including rotor losses," *2010 IEEE Energy Conversion Congress and Exposition*, pp. 3659–3666, 2010.

[53] A. Vagati, M. Pastorelli, G. Francheschini, and S. C. Petrache, "Design of low-torque-ripple synchronous reluctance motors," *IEEE Transactions on Industry Applications*, vol. 34, no. 4, pp. 758–765, July 1998.

[54] Z. Zhu, D. Howe, E. Bolte, and B. Ackermann, "Instantaneous magnetic field distribution in brushless permanent magnet dc motors. i. open-circuit field," *IEEE Transactions on Magnetics*, vol. 29, no. 1, pp. 124–135, 1993.

[55] Z. Zhu, D. Howe, and C. Chan, "Improved analytical model for predicting the magnetic field distribution in brushless permanent-magnet machines," *IEEE Transactions on Magnetics*, vol. 38, no. 1, pp. 229–238, 2002.

[56] C. Tang, M. Shen, Y. Fang, and P.-D. Pfister, "Comparison of subdomain, complex permeance, and relative permeance models for a wide family of permanent-magnet machines," *IEEE Transactions on Magnetics*, vol. 57, no. 2, pp. 1–5, 2021.

[57] C. Mi, M. Filippa, W. Liu, and R. Ma, "Analytical method for predicting the air-gap flux of interior-type permanent-magnet machines," *IEEE Transactions on Magnetics*, vol. 40, no. 1, pp. 50–58, 2004.

[58] A. R. Tariq, C. E. Nino-Baron, and E. G. Strangas, "Iron and magnet losses and torque calculation of interior permanent magnet synchronous machines using magnetic equivalent circuit," *IEEE Transactions on Magnetics*, vol. 46, no. 12, pp. 4073–4080, 2010.

[59] G. Dajaku and D. Gerling, "Air-gap flux density characteristics of salient pole synchronous permanent-magnet machines," *IEEE Transactions on Magnetics*, vol. 48, no. 7, pp. 2196–2204, July 2012.

[60] B. Koo and K. Nam, "Analytical torque ripple prediction using air-gap permeance and mmf functions in pm synchronous motors," in *2018 21st International Conference on Electrical Machines and Systems (ICEMS)*, Oct 2018, pp. 302–307.

[61] A. J. Pina and L. Xu, "Modeling of synchronous reluctance motors aided by permanent magnets with asymmetric rotor poles," in *2015 IEEE International Electric Machines Drives Conference (IEMDC)*, 2015, pp. 412–418.

[62] Q. Li, T. Fan, and X. Wen, "Armature-reaction magnetic field analysis for interior permanent magnet motor based on winding function theory," *IEEE Transactions on Magnetics*, vol. 49, no. 3, pp. 1193–1201, 2013.

[63] A. Aggarwal, E. G. Strangas, and J. Agapiou, "Analysis of unbalanced magnetic pull in pmsm due to static eccentricity," in *2019 IEEE Energy Conversion Congress and Exposition (ECCE)*, 2019, pp. 4507–4514.

[64] A. Aggarwal and E. G. Strangas, "Review of detection methods of static eccentricity for interior permanent magnet synchronous machine," *Energies*, vol. 12, no. 21, p. 4105, 2019.

[65] H. Polinder and M. J. Hoeijmakers, "Analytic calculation of the magnetic field in pm machines," in *IAS '97. Conference Record of the 1997 IEEE Industry Applications Conference Thirty-Second IAS Annual Meeting*, vol. 1, 1997, pp. 35–41 vol.1.

[66] O. Vlado, *Dynamics of saturated electric machines.* Springer-Verlag, 1989.

[67] M. V. K. Chari and S. J. Salon, *Numerical methods in electromagnetism.* Academic Press, 2005.

[68] G. Barakat, T. El-meslouhi, and B. Dakyo, "Analysis of the cogging torque behavior of a two-phase axial flux permanent magnet synchronous machine," *IEEE Transactions on Magnetics*, vol. 37, no. 4, pp. 2803–2805, 2001.

[69] M. Cheng, P. Han, and W. Hua, "General airgap field modulation theory for electrical machines," *IEEE Transactions on Industrial Electronics*, vol. 64, no. 8, pp. 6063–6074, 2017.

[70] M. Fakam, M. Hecquet, V. Lanfranchi, and A. Randria, "Design and magnetic noise reduction of the surface permanent magnet synchronous machine using complex air-gap permeance," *IEEE Transactions on Magnetics*, vol. 51, no. 4, pp. 1–9, 2015.

[71] T. Lubin, T. Hamiti, H. Razik, and A. Rezzoug, "Comparison between finite-element analysis and winding function theory for inductances and torque calculation of a synchronous reluctance machine," *IEEE Transactions on Magnetics*, vol. 43, no. 8, pp. 3406–3410, 2007.

[72] T. Hamiti, T. Lubin, and A. Rezzoug, "A simple and efficient tool for design analysis of synchronous reluctance motor," *IEEE Transactions on Magnetics*, vol. 44, no. 12, pp. 4648–4652, 2008.

[73] B. Gaussens, E. Hoang, O. de la Barriere, J. Saint-Michel, M. Lecrivain, and M. Gabsi, "Analytical approach for air-gap modeling of field-excited flux-switching machine: No-load operation," *IEEE Transactions on Magnetics*, vol. 48, no. 9, pp. 2505–2517, 2012.

[74] X. Y. Ma, G. J. Li, G. W. Jewell, and Z. Q. Zhu, "Quantitative analysis of contribution of air-gap field harmonics to torque production in three-phase 12-slot/8-pole doubly salient synchronous reluctance machines," *IEEE Transactions on Magnetics*, vol. 54, no. 9, pp. 1–11, 2018.

[75] R. Dutta, M. F. Rahman, and L. Chong, "Winding inductances of an interior permanent magnet (ipm) machine with fractional slot concentrated winding," *IEEE Transactions on Magnetics*, vol. 48, no. 12, pp. 4842–4849, 2012.

[76] Q. Li, T. Fan, X. Wen, and P. Ning, "An analytical approach to magnet eddy-current losses for interior permanent-magnet synchronous machines during flux weakening," *IEEE Transactions on Magnetics*, vol. 51, no. 8, pp. 1–9, 2015.

[77] H. Chen, D. Li, R. Qu, Z. Zhu, and J. Li, "An improved analytical model for inductance calculation of interior permanent magnet machines," *IEEE Transactions on Magnetics*, vol. 50, no. 6, pp. 1–8, 2014.

[78] P. Liang, Y. Pei, F. Chai, Y. Bi, and S. Cheng, "An improved method for armature-reaction magnetic field calculation of interior permanent magnet motors," *IEEE Transactions on Magnetics*, vol. 52, no. 7, pp. 1–4, 2016.

[79] G. Liu, L. Liu, Q. Chen, and W. Zhao, "Torque calculation of five-phase interior permanent magnet machine using improved analytical method," *IEEE Transactions on Energy Conversion*, vol. 34, no. 2, pp. 1023–1032, 2019.

[80] N. Bianchi and T. M. Jahns, *Design, analysis, and control of interior PM synchronous machines: presented at the IEEE industry applications society annual meeting, Seattle, USA, October 3rd, 2004.* IEEE, 2006.

[81] S. Taghipour Boroujeni and V. Zamani, "A novel analytical model for no-load, slotted, surface-mounted pm machines: Air gap flux density and cogging torque," *IEEE Transactions on Magnetics*, vol. 51, no. 4, pp. 1–8, 2015.

[82] N. Bianchi, *Electrical Machine Analysis Using Finite Elements*, 2017.

[83] J. Kirtley, "Electric machines." [Online]. Available: https://ocw.mit.edu/courses/electrical-engineering-and-computer-science/6-685-electric-machines-fall-2013/

[84] G. Dajaku and D. Gerling, "Stator slotting effect on the magnetic field distribution of salient pole synchronous permanent-magnet machines," *IEEE Transactions on Magnetics*, vol. 46, no. 9, pp. 3676–3683, Sep. 2010.

[85] ——, "Determination of air-gap flux density due to magnets using the new analytical model," in *The XIX International Conference on Electrical Machines - ICEM 2010*, Sep. 2010, pp. 1–6.

[86] K. H. Nam, *AC motor control and electrical vehicle applications.* CRC Press, Taylor & Francis Group, 2019.

[87] Sung-Il Kim, Ji-Young Lee, Young-Kyoun Kim, Jung-Pyo Hong, Y. Hur, and Yeon-Hwan Jung, "Optimization for reduction of torque ripple in interior permanent magnet motor by using the taguchi method," *IEEE Transactions on Magnetics*, vol. 41, no. 5, pp. 1796–1799, 2005.

[88] J. Xu, L. Gao, L. Zeng, and R. Pei, "Optimum design of interior permanent magnet synchronous motor using taguchi method," in *2019 IEEE Transportation Electrification Conference and Expo (ITEC)*, 2019, pp. 1–4.

[89] Y. Im, S. Hwang, S. Jang, J. Choi, and J. Choi, "Analysis of torque pulsation considering interior permanent magnet rotor rib shape using response surface methodology," *IEEE Transactions on Magnetics*, vol. 48, no. 2, pp. 979–982, 2012.

[90] M. Chowdhury, M. S. Islam, and M. Islam, "Design optimization of interior permanent magnet synchronous machines utilizing global response surface method for vari-

able speed drives," in *2019 IEEE International Electric Machines Drives Conference (IEMDC)*, 2019, pp. 609–614.

[91] L. Lebensztajn, C. A. R. Marretto, M. C. Costa, and J. . Coulomb, "Kriging: a useful tool for electromagnetic device optimization," *IEEE Transactions on Magnetics*, vol. 40, no. 2, pp. 1196–1199, 2004.

[92] H. Kim and B. Kwon, "Optimal design of motor shape and magnetisation direction to obtain vibration reduction and average torque improvement in ipm bldc motor," *IET Electric Power Applications*, vol. 11, no. 3, pp. 378–385, 2017.

[93] F. Bittner and I. Hahn, "Kriging-assisted multi-objective particle swarm optimization of permanent magnet synchronous machine for hybrid and electric cars," in *2013 International Electric Machines Drives Conference*, 2013, pp. 15–22.

[94] Sang-Moon Hwang, Jae-Boo Eom, Geun-Bae Hwang, Weui-Bong Jeong, and Yoong-Ho Jung, "Cogging torque and acoustic noise reduction in permanent magnet motors by teeth pairing," *IEEE Transactions on Magnetics*, vol. 36, no. 5, pp. 3144–3146, 2000.

[95] Byung-Chae Yun, Kwang-Kyu Han, Dong-Yeup Lee, Gyu-Hong Kang, Ki-Bong Jang, Heung-Kyo Shin, and Gyu-Tak Kim, "A study on the improvement of dynamic characteristics in interior permanent magnet motor by rotor shape design," in *2008 International Conference on Electrical Machines and Systems*, 2008, pp. 3126–3130.

[96] K. Yamazaki, M. Kumagai, T. Ikemi, and S. Ohki, "A novel rotor design of interior permanent magnet synchronous motors to cope with both maximum torque and core loss reduction," in *2012 IEEE Energy Conversion Congress and Exposition (ECCE)*, 2012, pp. 3692–3698.

[97] S. D. Sudhoff, *Power magnetic devices: A multi-objective design approach.* John Wiley amp; Sons, Incorporated, 2021.

[98] S. Hayslett and E. Strangas, "Analytical design of sculpted rotor interior permanent magnet machines," *Energies*, vol. 14, no. 16, 2021. [Online]. Available: https://www.mdpi.com/1996-1073/14/16/5109